Aus dem
Julius Wolff Institut für Biomechanik und Muskuloskelettale Regeneration
der Medizinischen Fakultät Charité – Universitätsmedizin Berlin

DISSERTATION

# Biologische Evaluation und Anpassung einer neuartigen, modularen Technologieplattform für die lokale Freisetzung von Ionen und Medikamenten in der Knochenheilung

# Biological evaluation and customization of a novel modular technology platform for local ion and drug delivery in bone healing

zur Erlangung des akademischen Grades
Doctor of Philosophy (PhD)

vorgelegt der Medizinischen Fakultät
Charité – Universitätsmedizin Berlin

von

Julia Catherine Kallenberg, geb. Berkmann

aus Braunschweig

Datum der Promotion: 04.06.2021

# Table of contents

## List of figures

# Abbreviations

| Abbreviation | Full name |
|---|---|
| BAG | Bioactive glass |
| BC | Blood clot |
| BHD | Bone healing device |
| BMC | Bone mineral content |
| BMD | Bone mineral density |
| BMP-2 | Bone morphogenetic protein-2 |
| BSA | Bovine serum albumin |
| BV | Bone volume |
| C1Sph/-SIP | Mesoporous carbon nanospheres/ with SIP coating |
| Ce | Cerium |
| cl | Contralateral |
| CM | Conditioned medium |
| CMSC | Centrum für Muskuloskeletale Chirurgie, Charité CVK, Charité – Universitätsmedizin Berlin, Berlin, Germany |
| Cu | Copper |
| EBM/ EGM | Endothelial basal/ growth medium |
| ECM | Extracellular matrix |
| ELISA | Enzyme-linked immunosorbent (ELISA) assay |
| EM | Expansion medium |
| EMA | European Medicines Agency |
| Ex/ em | Excitation/ emission wavelength |
| FDA | Food and Drug Administration, USA |
| FE-SEM | Field emission scanning electron microscopy |
| fx | Fracture |
| H&E | Hematoxylin and eosin |
| h/r MSC | Human/ rat mesenchymal stromal cells |
| HA | Hip arthroplasty |
| HUVEC | Human Umbilical Vein Endothelial Cells |
| i.c. | Intracardiac |
| i.p. | Intraperitoneal |
| IHC | Immunohistochemistry |
| IRB | Institutional review board |
| IVIS | In vivo imaging system |
| KA | Knee arthroplasty |
| LDH | Lactate dehydrogenase |
| M. | Musculus |
| MBG | Mesoporous bioactive glass |
| mBMC | Murine bone marrow cells |

| | |
|---|---|
| MOZART | **M**esop**O**rous matrices for locali**Z**ed pH-triggered rele**A**se of the**R**apeu**T**ic ions and drugs, European Union's Horizon 2020 research and innovation program, grant agreement No. 685872 |
| | MOZART collaboration partner: |
| Ashland | Ashland Specialties Ireland Limited, Dublin, Ireland |
| Cellogic | Cellogic GmbH, Berlin, Germany |
| Charité | Charité - Universitätsmedizin Berlin, Berlin, Germany |
| Delsitech | Delsitech Oy, Turku, Finland |
| Demokritos | National Center for Scientific Research/ Demokritos, Athens, Greece |
| FAU | Friedrich-Alexander-Universität Erlangen-Nürnberg, Erlangen, Germany |
| Nanolith | Nanolith Sverige AG, Bromma, Sweden |
| NBR | Nobil Bio Richerche Srl, Concesio, Italy |
| POLITO | Politecnico di Torino, Turin, Italy |
| UCM | Universidad Complutense de Madrid, Madrid, Spain |
| USFD | The University of Sheffield, Sheffield, UK |
| NAC | N-Acetylcysteine |
| NF/κB | Nuclear factor-κB |
| OM | Osteogenic medium |
| OPG | Osteoprotegerin |
| OR | Operating room |
| PBS | Phosphate-buffered saline |
| RANK/ RANKL | Receptor activator of nuclear factor-κB/ ligand |
| ROS | Reactive oxygen species |
| Ru | Ruthenium (tris(2,2-bipyridyl)-dichlororuthenium(II) hexahydrate) |
| *S. aureus* | *Staphylococcus aureus* |
| s.c. | Subcutaneously |
| SBF | Simulated body fluid |
| SHP407 | Thermosensitive hydrogel with polyurethane backbone |
| SIP | Self-immolative polymer |
| SOP | Standard operating protocol |
| Sr | Strontium |
| Tb.Th./_N./_Sp. | Trabecular thickness/ number/ separation |
| TCA cycle | Tricarboxylic acid cycle |
| TCH | Tetracycline hydrochloride |
| TV | Tissue volume |
| α-SMA | α-Smooth muscle actin |
| µCT | Micro-computed tomography |
| 3R | Replace, reduce, refine |

# Abstract

Deutsch. Muskuloskelettale Erkrankungen einschließlich Frakturen, Gelenkersatz oder -rekonstruktionen nehmen aufgrund des demografischen Wandels, einer erhöhten physischen Aktivität der Patienten und einer verringerten regenerativen Kapazität durch das Altern zu. Diese Erkrankungen verursachen beträchtliche körperlichen Schmerzen und erfordern lange Rehabilitationsphasen, besonders wenn Heilungsverzögerungen oder Infektionen auftreten. In diesem PhD-Projekt wurde eine neuartige, lokale Strategie zur Stimulation der Knochenheilung entworfen, entwickelt und biologisch evaluiert, um dem klinischen Bedarf an präventiven oder symptomatischen Interventionen bei Heilungsverzögerungen zu begegnen.

Dafür wurden die Einzelkomponenten eines hybriden Biomaterial-Komposits, welches sich aus mesoporigen Trägern (mesoporige bioaktive Gläser (MBG), Carbone) mit optionaler pH-sensitiver Beschichtung, eingebracht in ein thermosensitives Hydrogel, zusammensetzt, bezüglich Anwendbarkeit und Funktionalität *in vitro* und *in vivo* getestet. Der Grad lokaler Ansäuerung nach muskuloskelettaler Verletzung wurde gemessen, um einen Schwellenwert für die nötige pH-Reaktivität zu ermitteln. Die pro-regenerativen Effekte auf die Knochenheilung des Komposits mit ausgewählten therapeutischen Ionen und Medikamente wurden getestet.

Die Dosis- und Kompositionsabhängigkeit der zellulären Antwort auf Dissolutionsprodukte verschiedener bioaktiver Gläser konnte gezeigt werden. Die *in vivo* eingesetzten MBG zeigten eine für lokale Applikationen günstige, niedrige Distribution. Die *in vivo* pH-Reaktivität der Trägerbeschichtung konnte bestätigt werden. Ihr Einsatz für die Behandlung bakterieller Infektionen, die eine lokale Ansäuerung hervorrufen können - gezeigt an Proben humaner Synovialflüssigkeit - wird derzeit evaluiert. Die lokale Ansäuerung nach muskuloskelettaler Verletzung, gemessen im Rattenmodell, wurde als zu gering bewertet, um eine Reaktion des pH-sensitiven Materials und somit eine Wirkstofffreisetzung herbeizuführen. In der Knochenheilungsstudie zeigte das Komposit ohne pH-Reaktivität, beladen mit unterschiedlichen Ionen (Strontium, Kupfer) und Medikamenten (N-Acetylcystein, BMP-2), Beladungs-spezifische, pro-regenerative Effekte. Die verlängerte Freisetzung kleiner Mengen von BMP-2 verbesserte die Knochenheilung signifikant und kann eine vielversprechende Alternative zu den klinisch genutzten Kollagenschwämmen darstellen.

In diesem PhD-Projekt wurde ein neues Medikamentenfreisetzungs-System, welches funktionell durch die Beladung in Richtung Angiogenese, Osteogenese oder gegen Inflammation und Infektion angepasst werden kann, für die Verbesserung der Knochenheilung entwickelt. Biologisch evaluiert wurde dieses System in humanen Proben oder in relevanten prä-klinischen Modellen, um den Weg für eine künftige klinische Translation zu ebnen. Die positive Bewertung dieser Behandlungsstrategie und ihrer Komponenten durch klinische Orthopäden betont das große Translationspotenzial.

English. Musculoskeletal pathologies including fractures, joint replacements or reconstructions and their associated complications are on the rise. This increase is attributed to ongoing demographic changes, enhanced physical activity of patients, combined with a declining potential to regenerate upon aging. Such pathologies lead to considerable suffering and require long recovery times, especially when healing is impaired or infections occur. Within this PhD project, a novel local strategy to stimulate healing was conceptualized, developed, and biologically evaluated as a first step towards facing the so far unmet clinical need for effective and safe preventative or symptomatic interventions targeting compromised bone healing.

For this, the individual components of a hybrid biomaterial-based composite consisting of mesoporous carriers (mesoporous bioactive glasses (MBG), carbons (C1Sph)), optionally coated with a pH-sensitive, self-immolative polymer (SIP), and a thermosensitive hydrogel (SHP407) as embedding moiety were investigated with respect to practicability and functionality *in vitro* and *in vivo*. The degree of acidification after musculoskeletal injury was measured locally to unravel pH-sensitivity thresholds. The effect of the composite, biologically enhanced by selected therapeutic ions (Strontium, Copper) and drugs (N-Acetylcysteine, BMP-2), on bone healing was studied.

The cellular response to bioactive glass dissolution products was found to be highly dosage- and composition-dependent, making testing of every formulation essential. The employed MBG exhibited a low dispersion behavior *in vivo*, which is a pre-requisite for local treatments. *In vivo* responsiveness of the pH-sensitive coating was confirmed, and is currently evaluated in the context of bacterial infections that can induce local acidification as detected during this project in septic human synovial fluids. The observed degree of local pH acidification after musculoskeletal injury in rats, however, was too subtle to induce self-immolation of the SIP. Pro-regenerative effects of therapeutic substances on the bone healing outcome were identified, using the composite locally without SIP, indicating a successful treatment concept. The prolonged, low-dose release kinetics of BMP-2 induced significant and superior bone healing, thus qualifying as a promising alternative to the clinically used collagen sponge.

Within this PhD project, a new drug-delivery system to enhance bone healing, that can be functionally tailored by ion doping and drug loading towards angiogenesis, osteogenesis, or against inflammation and infection, was biologically evaluated and customized. The usage of primary human material and clinically relevant pre-clinical models enables further development towards clinical application. The approval of several clinicians concerning need and future use of the composite hybrid system or its individual components imply a great potential for future translation.

# 1. Introduction

Bone healing consists of well-orchestrated, consecutive and partially overlapping pro- and anti-inflammatory, pro-angiogenic as well as pro-osteogenic signaling phases involving a multitude of cell types. In the adult mammalian organism, bone is a unique tissue – next to liver – for its inherent potential to fully regenerate without scar formation, thereby restoring its physiological function (*restitutio ad integrum)* [1, 2].

Despite the regenerative potential of bone, around 10 % of fracture patients experience impaired healing, presenting either as delay in healing or as the development of pseudoarthrosis or non-unions (discussed in [1]). This imposes a high burden on the patient's quality of life as these clinical conditions can require additional surgical interventions and prolong the time to recovery. Pathologies of the musculoskeletal system are among the five most costly diseases in Germany (Figure 1A, B). They are associated with productivity losses as well as with higher risks for co-morbidities that arise from restricted physical activity [3]. All the above issues significantly aggravate the negative social-economic impact [4].

With increasing age, the regenerative capacity of bone after fracture declines [5, 6], which can be attributed to more prevalent comorbidities such as diabetes and osteoporosis, but also to a chronic low-grade pro-inflammatory systemic milieu due to the increase in immunological memory, a phenomenon referred to as inflamm-aging [7]. Globally, increasing life expectancy and low birth rates especially in developed countries are causing a major demographic change [8] (Figure 1C). As bone quality decreases upon aging, fracture incidence is augmented (Figure 1D) [9]. All of the above translates into a higher number of geriatric patients, thus, the prevalence of impaired healing cases is expected to rise.

Both, the current and the prospective rise in prevalence indicate an urgent and so far not adequately addressed medical need for effective strategies to improve healing in compromised settings. One approach is the early identification of patients at risk with clinically considered patient-dependent risk factors such as age, sex, comorbidities, and life-style habits (including smoking and diet) as well as injury-dependent factors [10].

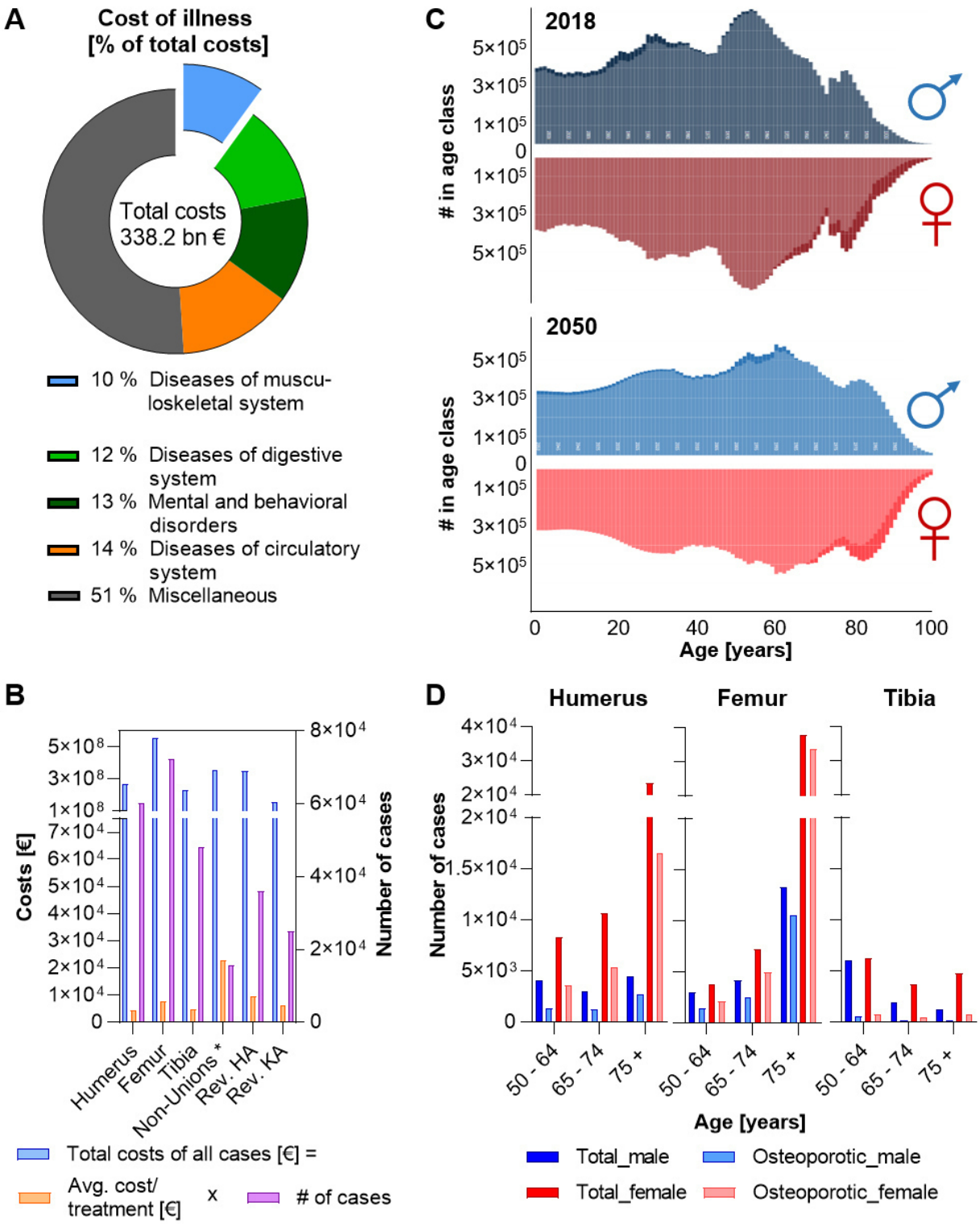


**Figure 1. Cost of musculoskeletal diseases, focusing on long bone fractures in the context of the demographic change and age distribution in Germany.** (**A)** Total costs and relative contribution of the top 4 most costly pathologies in % for the year 2015. (**B)** Number of cases, average costs per treatment in € and total cost per long bone fractures, non-unions (*: all stationary cases with non-union as primary diagnosis), and revisions surgeries for (total) hip arthroplasty (HA) and (total) knee arthroplasty (KA) in € per year. Shown numbers represent the means of the years 2010 – 2016. (**C)** Age structure in 2018 and prospective age structure in 2050, assuming version 1 (V1) of population development. (**D)** Number of cases for long bone fractures relative to age, sex and osteoporosis diagnosis

per year. Shown numbers represent the means of the years 2010 – 2016. (**A, C**) Federal Statistical Office, Wiesbaden, Germany, graphic modified. (**B, D**) Data collection by Cellogic, sources: Federal Statistical Office, Wiesbaden, Germany: ICD10 (fractures: S42.2*/S72.0*/ S82.1*, S82.2*, S82.3*, non-unions: M84.1*, M84.4*) and OPS sources (revision HA/ KA: 5-821.*, 5-823.*), osteoporotic numbers: courtesy of Cellogic, based on [9], independent visualization.

Having identified such patients, novel treatment strategies are needed that specifically target the underlying cause for the reduction in healing capacity, while limiting side effects. Reasons for impaired aseptic healing are overshooting of the pro-inflammatory response, a diminished angiogenic/ osteogenic potential, malfixations, or critical gap size. Infections can additionally delay healing and lead to osteolysis [1]. Currently, there is no minimally-invasive treatment available that is biocompatible, safe and can be customized based on the patient-specific needs to induce a pro-angiogenic or pro-osteogenic response. Moreover, most secondary interventions entail invasive surgery which poses an additional risk, especially to the elderly patient. In that light, an EU Horizon 2020 project called 'MOZART'- '**M**esop**O**rous matrices for locali**Z**ed pH-triggered rele**A**se of the**R**apeu**T**ic ions and drugs' (No. 685872), to which this PhD project belongs, was conducted. Eleven European partners (will be referred to using their acronyms in the following, explanations can be found in the list of abbreviations), both from academia and industry, collaborated for four years in order to develop a novel treatment strategy combining biomaterials and biological knowledge. A series of inorganic spheres that could be exploited as smart carrier platforms for localized and targeted therapies were developed (Figure 2). As a carrier for therapeutic drugs, nano- to micron-sized (~ 200 nm – 5 µm) mesoporous bioactive glass (MBG) spheres were synthesized, with the mesopores serving as a reservoir for the drug cargo. Moreover, biological effects of MBG can be directed through the introduction of therapeutic ions into the glass network, allowing for potential dual and synergistic actions by the ion-doped carrier and the loaded drug. To ensure local treatment and minimize systemic side effects, a place-keeper as embedding moiety for the MBG was required. For this, a thermosensitive polyurethane-based hydrogel (SHP407) that undergoes sol-gel transition at physiological body temperature of 37°C was developed. The combination of MBG spheres with this hydrogel enables injection into the target area and can therefore be defined as a minimally-invasive approach to stimulate bone healing. The volume, concentration of MBG, and hydrogel properties can be adjusted, broadening the range of possible applications. The last biomaterial component of this novel composite consisted of a pH-sensitive and self-immolative polymeric (SIP) coating to cover the mesopores of the MBG, thereby enclosing the loaded drugs. Injury-induced blood vessel rupture is reported to result in local hypoxia and acidification of the injury site [11, 12]. Under acidic conditions, the pH-sensitive moiety of the SIP is subjected to proton-assisted cleavage, resulting in sequential disassembling of the SIP into the polymeric building blocks, thereby opening the mesopores and enabling drug release in a

targeted and endogenously triggered manner. This additional safe-guard is expected to further limit off-target and side effects, as the local environment itself triggers the drug release and these trigger conditions should be absent in neighboring tissues.

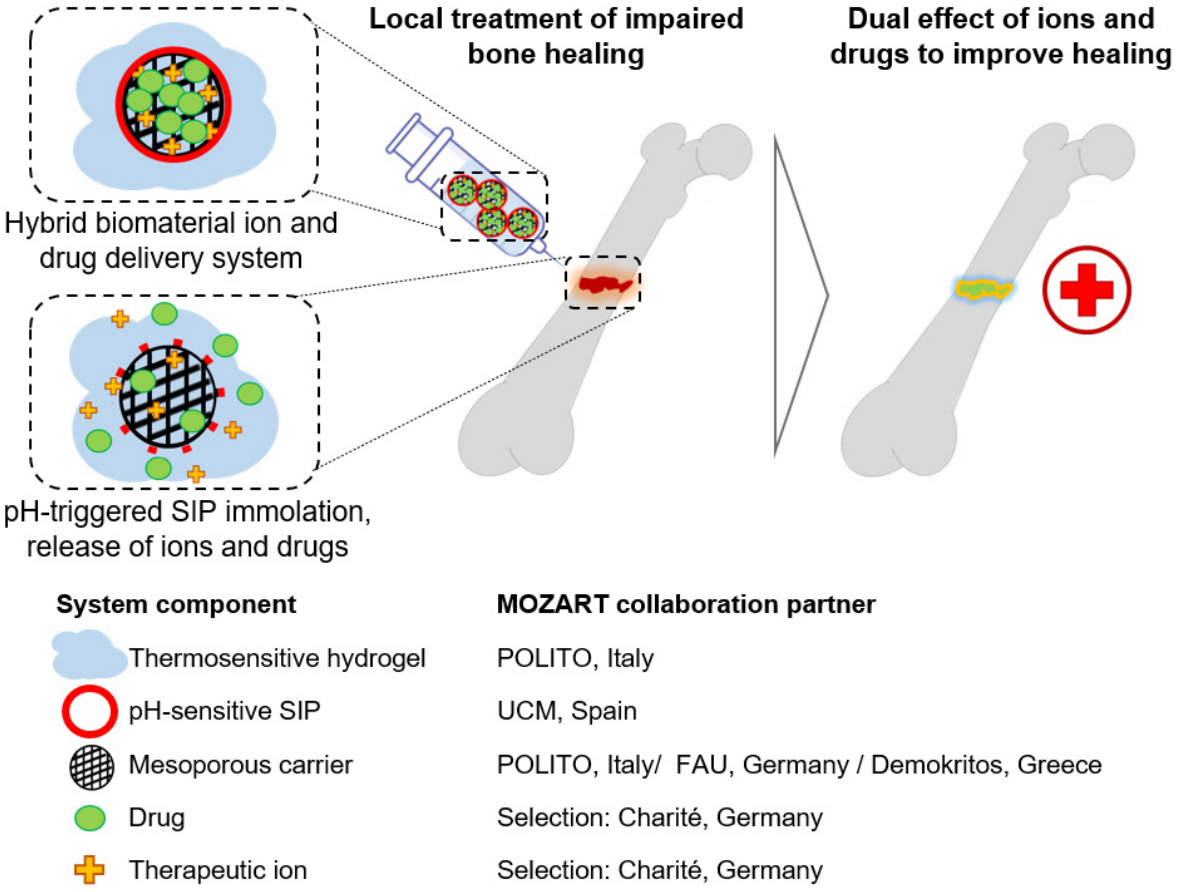


**Figure 2. The MOZART idea.** Nano- to micron-sized mesoporous bioactive glasses (MBG) with a versatile ionic make-up act as carriers that can be loaded with drugs, pores can be covered and closed by a pH-sensitive, self-immolative polymer (SIP) coating. The loaded and coated MBG can be embedded in a thermosensitive hydrogel (SHP407) acting as place-keeper (top boxed figure). This composite can be utilized to direct and improve bone healing. Upon exposure to physiological fluid and in an acidic environment, the SIP degrades, and the drug can diffuse out of the pores. Moreover, the glass network dissolves, thereby therapeutic ions can be released (bottom boxed figure) to evoke a beneficial healing outcome in conjunction with the released drug.

In my PhD project, emphasis was laid on defining promising bioactive components (drugs and therapeutic ions) in the context of bone healing and on biologically evaluating and customizing the combination of bioactive components and biomaterials. Based on this aim, my PhD consisted of several sub-projects. In brief, I investigated the different components of the biomaterials-approach with respect to cyto-and biocompatibility and biological effectiveness *in vitro* and *in vivo*. The quest to utilize the pH as an endogenous trigger for substance release was validated as part of my thesis by providing *in vivo* target values for stimulus sensitivity in the early fracture hematoma; the pH-responsiveness of the developed SIP was confirmed *in vivo*. Other potential applications for the SIP

coating were identified in human patients with musculoskeletal infections and are currently under further investigation. Within my project, the final composite, varying in the loaded drugs (BMP-2, N-Acetylcysteine and Tetracycline) and doped therapeutic ions (Strontium, Copper and Cerium) to enable versatility of possible applications and treatment personalization based on risk factor identification (Figure 3), was evaluated in a rodent osteotomy model of impaired bone healing. By gaining an understanding of the biology underlying impaired bone healing and its clinical representations as well as regulatory aspects of novel treatment approaches, this PhD project provided the opportunity to explore the combination of the clinically proven growth factor BMP-2 with MBG to tailor and improve release kinetics. In previous studies, the required BMP-2 dosage to achieve full bridging of the fracture gap could be reduced by 10-fold compared to the clinically applied supraphysiological dosage [13], yet, the unfavorable release kinetics with a high burst release remained, as the clinically utilized absorbable collagen sponge was employed as drug carrier. In this context, I identified MBG microspheres as suitable release platforms for prolonged, low-dose BMP-2 release. All material components, including the MBG, the C1Sph and the SHP407 were tested *in vivo* for the first time. In parallel, the concept was presented to orthopedic clinicians and adjusted based on their demands, questionnaires were designed and analyzed in order to identify the clinical potential that this concept harbors as well as to define possible application sites.

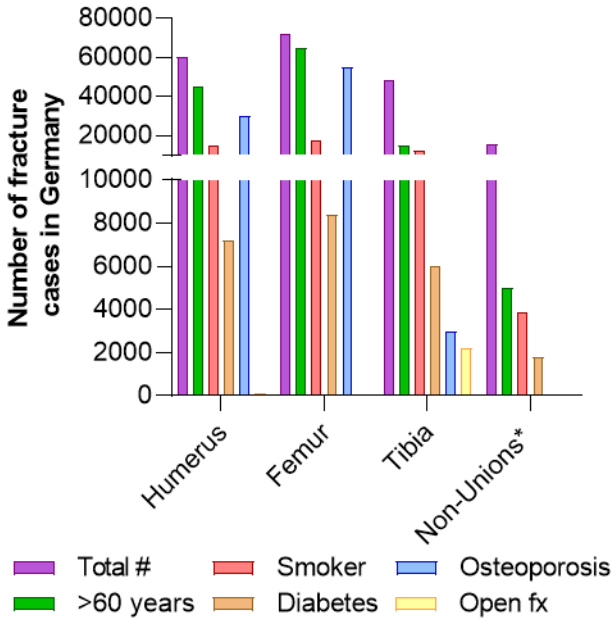


**Figure 3. Healthcare clinical assessment of number of fracture cases based on fracture location, comorbidities and other risk factors.** Fracture treatment strategies depend on age, health, life-style and fracture types. In elderly patients, an anti-inflammatory intervention is of highest priority, while osteoporotic patients need a strong osteogenic boost. Angiogenic responses are reduced among smokers, rendering a pro-angiogenic intervention beneficial. In diabetic patients, a combinatorial approach of pro-angiogenic and anti-inflammatory treatments is advisable. The management of open fractures (fx) or prosthetic infections necessitate anti-microbial strategies. Non-unions*: all stationary cases with non-union as primary diagnosis. Total #; >60 years and open fx: Shown numbers represent the means of the years 2010 – 2017; source: Federal Statistical Office, Wiesbaden, Germany based on ICD10 classifications. Number of smokers, diabetes and osteoporotic patients based on prevalence rates (Smokers: Special Eurobaromater 458 '*Attitudes of Europeans towards tobacco and electronic cigarettes*', European Union, 2017; diabetes: International Diabetes Foundation, https://www.idf.org/our-network/regions

members/europe/members/136-germany.html, accessed in November 2018; osteoporosis: [9]). Data courtesy of Cellogic. Independent visualization.

The focus of PD Dr. Katharina Schmidt-Bleek's working group is centered on understanding the effects of immune cell populations and their age-related changes on bone healing with the intention to apply gained knowledge for the development of novel treatment strategies. The present collaborative study aimed to combine biological expertise and biomaterial development to establish a platform for personalized local preventative or symptomatic treatments. My PhD project represented the link between basic and translational research. It focused on identifying therapeutic ions and drugs to be used in conjunction with the biomaterial carriers, biologically validating the individual biomaterial components *in vitro* and *in vivo*, including individual suitability testing for future application in the context of bone healing, and testing the composite bone healing devices (BHD) with different drugs and therapeutic ions in a pre-clinical femoral osteotomy model. In close collaboration with the Centrum für Muskuloskeletale Chirurgie, Charité – Universitätsmedizin Berlin (CMSC), I collected clinically relevant human patient data and enabled decision-making on product design. In light of the great clinical need for novel treatment strategies, the lessons learned within my PhD project allow fine-tuning of the current BHD design for future clinical translation of this novel treatment concept or its individual parts. My work has resulted in four publications and three additional manuscripts (one submitted, two in draft).

# 2. Materials and methods

This section explains the methods used within my PhD project. Details on synthesis and characterization of the employed materials can be found in the respective publications [14-17]. Material development, doping and loading were carried out by MOZART partners, based on the physiological boundary conditions and required biological effects that were defined during my PhD project. Unless stated differently, the assays were performed according to the manufacturer´s instructions. Manufacturers' headquarter locations are given at first mentioning.

## 2.1. Material-centered *in vitro* studies

### 2.1.1. Material preparation and customization (MBG/ C1Sph, SHP407, composite)

For the preparation of MBG (consisting of binary $SiO_2$-CaO) or SIP-coated C1Sph (C1Sph-SIP), materials were weighted and suspended in physiological fluid (Sterofundin (B. Braun Melsungen, Melsungen, Germany) / 0.9% NaCl/ PBS). All materials were used at a final concentration of 15 mg/ml in the *in vivo* studies, with subcutaneous (s.c.) injections of 200 µl (3 mg), and 0.75 mg MBG applied in the bone healing study. The materials were ultrasonicated twice for two min, with 80 hz, maximal power. The SHP407 was dissolved o/n at 4 °C with repeated vortexing. The composite (MBG in SHP407/ blood clot without SIP coating) was prepared by mixing ice-cold SHP407 with MBG at a final gel concentration of 150 mg/ml, 50 µl of the composite was administered in the bone osteotomy gap. For the autologous blood clot, a syringe was coated with sodium citrate to prevent coagulation, blood was drawn from the vena saphena of the right hind limb. 7 µl of Thrombin solution (500 i.E./ml, 12 % $CaCl_2$, Baxter, Deerfield, USA) was mixed with MBG suspension and 180 µl of blood. After clotting, the composite was inserted in the fracture gap.

### 2.1.2. BMP-2 *in vitro* release kinetics

rhBMP-2 (Peprotech, Hamburg, Germany) loading in MBG and confirmation of loading was carried out by collaboration partners (described in [14]), leading to a final dosage of 50 µg BMP-2 per animal. *In vitro* release experiments were performed at a concentration of 75 µg/ml in PBS or Tris-HCl (Trizma Base, Sigma-Aldrich, St. Louis, USA) set to pH 7.4 at 37 °C for 14 days. At each time point, 500 µl MBG-free supernatant was harvested and stored at -20 °C, the MBG suspension was re-supplemented with 500 µl fresh solution. Released BMP-2 was quantified using an α-BMP-2 enzyme-linked immunosorbent (ELISA) assay (Peprotech). Each sample was tested in duplicate using TMB as substrate and measured at 450 nm (reference measurement 620 nm).

## 2.2. Cell culture studies

### 2.2.1. Primary cell cultures

Primary human bone marrow mesenchymal stromal cells (hMSCs), isolated after approval by the institutional review board (IRB) of the Charité and patients' consent, were donated from the Core Facility "Tissue Harvesting of the BIH Center for Regenerative Therapies". Cell cultivation occurred in expansion medium (EM) containing Dulbecco's modified Eagle's medium (DMEM, low glucose, Sigma Aldrich) supplemented with 10 % fetal bovine serum (FBS Superior, Biochrom, Berlin, Germany), 1 % GlutaMAX (Thermo Fischer Scientific, Waltham, USA), and penicillin (100 U/ml) /streptomycin (0.1 mg/ml, Biochrom) at 37 °C in a humidified incubator with 5 % $CO_2$ atmosphere.

Primary rat MSCs (rMSCs) were isolated from rat femora, followed by outgrowth cultures. Rat MSCs were cultivated in EM under identical conditions as the hMSCs.

For the cultivation of Human Umbilical Vein Endothelial Cells (HUVECs, single donor; Lonza, Basel, Switzerland), endothelial growth medium (EGM, Lonza) containing endothelial basal medium (EBM) and additional manufacturer-supplied growth factors were utilized. 25000 cells/cm² of cells in passage 2-3 were seeded for tube formation assays.

For all cell cultures and experiments, medium was exchanged twice per week. Ions and drugs were re-supplemented during each medium change, while the biomaterials were added at experiment start to transwell inserts (0.4 µm pore size, Corning, Corning, USA). For the cytocompatibility tests and osteogenic differentiation, cells were seeded in 24-/ 48- tissue culture treated well plates in EM (final volume 500/ 250 µl/well), assays were started after overnight attachment. For subconfluent cultures, 2400 (viability) – 6400 (osteogenesis) cells/cm², for confluent cultures 15000 cells/cm² hMSCs (rMSC: 2500 cells/cm² (viability); 25000 cells/cm² (osteogenesis, confluent)) were seeded.

### 2.2.2. Cytocompatibility tests (Metabolic activity, cell count, cytotoxicity)

The metabolic activity of r/ hMSCs was quantified by Presto Blue (diluted 1:10 in EM, ex/em 560/590, Thermo Fisher Scientific). Cell number was determined by fixing the cells in 4 % formaldehyde (VWR, Darmstadt, Germany), DAPI-staining of nuclei (1 µg/ml, 15 min, wash with PBS; Sigma Aldrich), fluorescence imaging (BZ-X810, Keyence, Osaka, Japan), and automated counting of the nuclei using Fiji ImageJ [18]. The LDH assay (Roche, Basel, Switzerland) was performed to investigate cytotoxicity on 25 µl debris-free supernatant of the viability experiments.

### 2.2.3. Functional assays (Angiogenesis, Osteogenesis)

*Tube formation assay – angiogenesis*

For the tube formation assay, 24-wells coated with 50 µL growth factor reduced Matrigel® Basement Membrane Matrix (BD Biosciences, Franklin Lakes, USA) were used. HUVECs were seeded in EBM,

supplemented with hMSC conditioned medium (CM) [16] or NAC and returned to the incubator. After 16 hours, tube formation was evaluated by microscopy (DMI6000B, Leica, Wetzlar, Germany) and a custom-made macro using Fiji ImageJ [18].

*Osteogenic differentiation assays*

To induce osteogenic differentiation, cells were cultivated in osteogenic differentiation medium (OM) containing EM supplemented with 50 µM L-Ascorbic acid 2-phosphate sesquimagnesium salt hydrate, 10 mM ß-Glycerophosphate disodium salt hydrate and 100 nM Dexamethasone (all: Sigma Aldrich). Cell/ debris-free supernatant was collected during media changes and stored at -80 °C. For the determination of inorganic phosphate in the supernatant, a colorimetric phosphate assay (Abcam, Cambridge, United Kingdom) was carried out, diluting all EM conditions 1:100 and all OM conditions 1:800 in EM. At the final time points, cells were fixed, washed with distilled water, and the mineralized extracellular matrix (ECM) was stained with 0.5 % w/v Alizarin Red S (Sigma-Aldrich, 10 min, RT). Stain extraction with 10 % w/v Cetylpyridinium chloride (Sigma-Aldrich) allowed quantification by absorbance at 562 nm. The hydroxyapatite portion of the mineralized matrix was visualized using the OsteoImage Assay (Lonza) with an additional nuclei staining.

### 2.3. *In vivo*/ *ex vivo* animal studies

Female C57BL/6N mice were purchased from Charles River Laboratories and employed in the studies at an age of 3 months, female Sprague-Dawley rats (Janvier Labs) were aged 3 months for the analysis of pH changes or >7 months for the bone healing study. Animal import occurred with health certificate, animals were kept under FELASA obligatory hygiene standards under conventional housing with food and water available ad libitum and controlled temperature (20 ± 2°C) as well as 12 h light/dark cycle. All *in vivo* studies were approved by the local animal protection authorities (Landesamt für Gesundheit und Soziales: G0027/17, G0293/17, G0017/16, G0155/18, G0258/18) and conducted according to the German Animal Welfare Act, the National Institutes of Health Guide for Care and Use of Laboratory Animals and the ARRIVE guidelines.

Animals were anesthetized with a mixture of isoflurane (Forene, Abott, Wiesbaden, Germany) and oxygen, moreover analgesia with bubrenorphine (Temgesic, RB Pharmaceuticals, Berkshire, United Kingdom), antibiotic treatment (Clindamycin, Ratiopharm, Ulm, Germany) were administered via subcutaneous injection and eye ointment was given, followed by study-specific interventions as outlined below. Animals were kept on a 37 °C heating plate during surgical interventions. After femoral osteotomy or muscle trauma, the animals received a potent analgesic (Tramadolhydrochloride, Grünenthal, Aachen, Germany) for three days post surgery via the drinking water. Sacrifice of animals occurred in deep anesthesia (intraperitoneal (i.p.) injection of medetomidine and ketamine) via cervical dislocation (mice) or intracardiac (i.c.) injection of KCl (rats).

2.3.1. Biodistribution study/ pH-triggered cargo release/ *In situ* validation of SHP407

For the biodistribution of DY-677-labeled MBG (DY-677: Dyomics, Jena, Germany) and the pH-triggered cargo release from C1Sph-SIP study, the dorsal region of anesthetized mice was clipped and 200 µl containing 3 mg material were injected s.c. in the nuchal fold using a 18-20 G needle or dwelling canula. Imaging of the animal to detect the fluorescent DY-677-MBG or cargo (for C1Sph-SIP: tris(2,2-bipyridyl)-dichlororuthenium(II) hexahydrate (Ruthenium (Ru)), Sigma Aldrich) was conducted using IVIS® Lumina (Caliper LifeSciences, USA; ex/em: DY-677: 675 nm / Cy5.5; Ru: 465 nm/ Cy5.5). To test pH-responsiveness, the animals received repeated injections of pH 7.4 or 4 physiological solution over 30 min via the dwelling cannula. All imaging steps occurred under isoflurane anesthesia.

A similar approach was followed for the *in situ* validation of SHP407 in freshly sacrificed mice. Here, body temperature was maintained through a heating plate set to 37°C and a red-light lamp. Injection of ice-cold, liquid SHP407 or composite (200 µl) s.c. in the nuchal fold was accomplished by a G18 needle, smaller amounts were administered in a 0.7 mm osteotomy gap by creating a drop of gel. After 5 min of gelation, the injection sites were opened; dispersion and gelation were studied visually and haptically.

2.3.2. pH study after musculoskeletal injury

To measure pH in musculoskeletal trauma, a 5 mm femoral osteotomy gap was created in rats. A size-matched muscle trauma was established by caudally cutting the skin, blunt immobilization of the Musculus (M.) gastrocnemius, isolation of the M. soleus and two times 20 s crushing using a clamp. pH was measured inside the hematomas using a microinvasive needle-type optical pH microsensor (pH-1 micro, needle-type sensor, PreSens, Regensburg, Germany) based on the dual life time reference method.

2.3.3. Femoral osteotomy/ Bone healing studies

Femoral osteotomies were created in anesthetized mice and rats. The operation area was shaved and disinfected. The skin was incised longitudinally, the femur exposed by dissecting the fasciae and dislodging the muscles bluntly. The external fixators (MouseExFix/ MouseDis/ RatExFix, RISytem, Davos, Switzerland) were mounted on the femur, followed by sawing using a Gigli wire saw (mice, gap size: 0.7/ 1.4 mm) or an oscillating saw (W&H, Bürmoos, Austria) and a saw guide (rats, gap size: 2/ 5 mm). After wound closure, animals were returned to their cages.

2.3.4. Tissue harvest

Blood was collected by i.c. puncture under deep anesthesia. After sacrifice, injection sites, organs, bones etc. were harvested and stored in ice-cold PBS or were fixed in 4 % PFA (Science Services, München, Germany) in PBS.

2.3.5. Flow cytometry

Cells were isolated form murine femora by opening the bones on both sides and flushing the bone marrow out with a 24G needle and filtration through a 40µm strainer (Falcon, Corning). Cells were re-suspended in RPMI 1640 (+10 % FCS) to a final concentration of 500,000 cells/ml. The CellRox Deep Red (Thermo Fisher, 3.2.2.) assay was performed at 37 °C using 0.5 mM NAC (1 h) and 200 µM tert-butyl hydroperoxide (TBHP, 30 min), followed by CellRox ROS staining (750 nM) and CyTox nuclei staining. Flow cytometric measurement was performed using a BD LSR Fortessa SORP (BD Biosciences).

2.3.6. Micro-computed tomography

Micro-computed tomography (µCT) was conducted on fixed bones using a Skyscan 1172 (Bruker, Billerica, USA) at a nominal voxel resolution of 8 µm, 0.5 mm aluminum filter, 70 kV (mouse)/ 80 kV (rats) source voltage and 124 µA (mouse)/ 142 µA (rats) source energy. Reconstruction of shadow images occurred using an adjusted Feldkamp algorithm with nRecon software. Custom-made scripts were employed for the analysis in CTan software, CTvox software (all: Bruker) was utilized for visualization. Via the Otsu algorithm, global thresholds were selected and applied to all bone samples per *in vivo* study, calibration occurred using reference phantoms (Bruker).

2.3.7. Histology (H&E, MOVAT's pentachrome)

After fixation, the explanted injection sites or decalcified rat femora were de-hydrated, paraffin-embedded and cut in 5 µm tissue sections. Sections were de-paraffinized in Xylol and re-hydrated by a descending alcohol series ending in distilled water. Hematoxylin and eosin (H&E) and MOVAT's pentachrome staining [19] were performed, the former was embedded in Aquatex (Sigma Aldrich), while the latter was followed by dehydration and embedding in Vitroclud (Langenbrink, Emmendingen, Germany). Frozen samples embedded in SCEM (Section Lab, Hiroshima, Japan) or TissueTec (Sakura Finetek, Tokio, Japan) (murine bones or the muscle/ osteotomy hematomas) were cut in 5 µm-thick sections with the Cryostat (CM3050 S, Leica; undecalcified bones were cut with Kawamoto Tape as described in [20]) and fixed for 10 min in 4 % PFA, followed by the respective staining. Images were taken using a brightfield microscope (Axioskop 40, Zeiss, Oberkochen, Germany). Histomorphometric and cell count analysis were carried out by color thresholding using custom-made macros in FiJi/ ImageJ [18], software.

2.3.8. Immunohistochemistry on tissue sections (α-SMA, CD68)

For α-SMA or CD68 staining on de-paraffinized, re-hydrated rat bone sections, sections were blocked with 5 % normal horse serum (Vector Laboratories, Burlingame, USA) in 1 % BSA/PBS (1 h) and stained with α-α-SMA (1:400, mouse monoclonal, clone 1 A4, DAKO Agilent Technologies, Santa Clara, USA) or α-CD68 (1:2000, mouse monoclonal, clone BM4000, OriGene Technologies,

Rockville, USA) overnight at 4 °C. As secondary antibody, an α-mouse, rat adsorbed biotinylated secondary antibody (Vector Laboratories, 1:50) in 2 % normal horse serum and 1 % BSA/PBS was incubated (30 min). Application of AB complex (Vector AK 5000, Vector Laboratories), section alkalization with chromogen buffer (pH 8.2) and staining visualization (Vector SK 5100, Vector Laboratories) followed. Mayer's hematoxylin was used as counterstain, embedding occurred in Aquatex. The blood vessel (α-SMA) occupied area or the area of CD68+ cells residing on newly formed bone were normalized to the total callus area.

2.3.9. Metabolomic analysis

Samples stored at -80 °C were sent to metaSysX (Potsdam, Germany), prepared and analyzed as described in [21].

### 2.4. *Ex vivo* clinical studies

For the *ex vivo* pH measurement of orthopedic patient samples directly after extraction, a just calibrated electrochemical pH microelectrode (8220BNWP Orion PerpHecT ROSS, Thermo Scientific, Germany) was utilized. The studies were performed after approval by the Institutional Review Board (IRB) of the Charité–Universitätsmedizin Berlin (IRB approval EA4/171/16 and EA4/040/14) and patient consent according to the International Conference on Harmonization Guidelines for Good Clinical Practice and the Declaration of Helsinki.

### 2.5. Statistics

Statistical analysis was conducted with GraphPad Prism (GraphPad Software, San Diego, USA), and p-values were considered statistically significant (*) when $p \leq 0.05$. Further differentiation of significance (**, ***) as presented in the corresponding publications is not shown for reasons of clarity and consistency throughout all figures. For small samples sizes in the *in vivo* studies, two-tailed Mann-Whitney U tests were performed. For the *in vitro* studies, unpaired, two-tailed Student's t-tests or one-way ANOVA with Dunnett's/ Tukey's multiple comparison tests were performed.

## 3. Main results

As outlined in the introduction, the local treatment strategy developed within the MOZART project consists of multiple biomaterial components that act as carrier and place-keeper for drugs and therapeutic ions, altogether the composite should allow for localized pharmacological intervention to prevent or treat impaired bone healing. The proposed biomaterial components comprise mesoporous bioactive glasses (MBG) or mesoporous carbons (C1Sph) as drug and ion carriers, a pH-sensitive SIP-coating to cover the carrier and close the mesopores, as well as a thermosensitive hydrogel (SHP407) acting as embedding moiety (Figure 4). None of the biomaterial components had been tested *in vivo* before, thus, I biologically validated every individual biomaterial before progressing to the final application to improve bone healing. For this, the biomaterial components were combined with the therapeutic ions and drugs selected and validated with this PhD project.

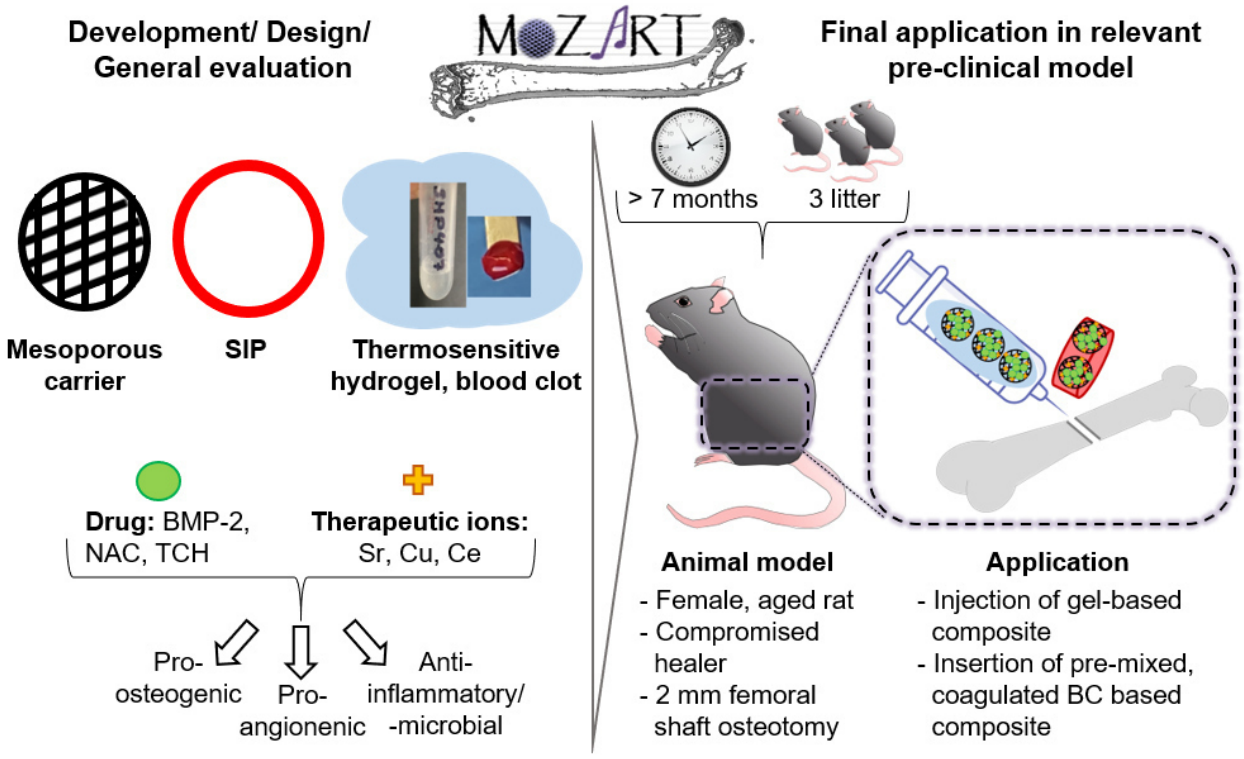


**Figure 4. Schematic representation of biomaterial components and application of different composites/ bone healing devices (BHD) in a rat model of compromised bone healing.**

The results will guide you through the different steps in developing and evaluating the bone healing device (BHD) and are grouped into the categories material validation (3.1.), functional testing (3.2.) and clinical evaluation of the BHD (3.3.). MOZART collaboration partners synthesized, doped and loaded the biomaterials using the therapeutic candidates selected by me to induce pro-osteogenic, pro-

angiogenic, anti-inflammatory or anti-infective effects (Figure 4). When not specifically stated otherwise, the results shown were obtained by me.

### 3.1. Material validation and customization

#### 3.1.1. Bioactive glasses (BAG) – ionic composition matters

Since the discovery of the famous 45S5 or Bioglass by Larry Hench in 1969 [22], a new class of bioactive ceramic materials was founded. This class yield a strong and stable chemical bond with bone tissue, but also form bone-like carbonated hydroxyapatite on their surface in an ion-exchange reaction upon contact with biological fluids, and can further stimulate regenerative processes [23]. Today, various BAG with different ionic compositions exist. In that context, 45S5 and 1393, two commercially available BAG that deviate in their ionic make-up (Figure 5A), were studied *in vitro* by colleagues and me for the regenerative responses that their ionic dissolution products can evoke on primary hMSCs [16]. For this, osteogenic differentiation was induced in hMSCs via cultivation in osteogenic medium (OM) under continuous ionic dissolution of the two types of BAG contained in transwell inserts (Figure 5B). A 2D-tube formation assay using primary HUVECs and conditioned medium (CM) of hMSC under BAG exposure was conducted to unravel potential pro-angiogenic paracrine responses by hMSCs. Investigation of tube formation showed a pro-angiogenic response induced by 45S5 with lower 45S5 concentrations yielding the highest total tube length and branching (Figure 5C). Conversely, after 14 days of osteogenic induction in hMSCs, low-dose ionic dissolution products of 1393 caused the highest degree of mineralized matrix (Figure 5D). In sum, this study demonstrated that ions dissolved from BAG can stimulate hMSC function and that the response by hMSCs to BAG is dosage- and composition-dependent. Therefore, the choice of ionic species contained in the glass network can decisively influence the pro-regenerative effect. Changing the ionic make-up of the BAG enables steering of cellular responses, at the same time, different compositions need to be tested in parallel to identify the most promising candidates.

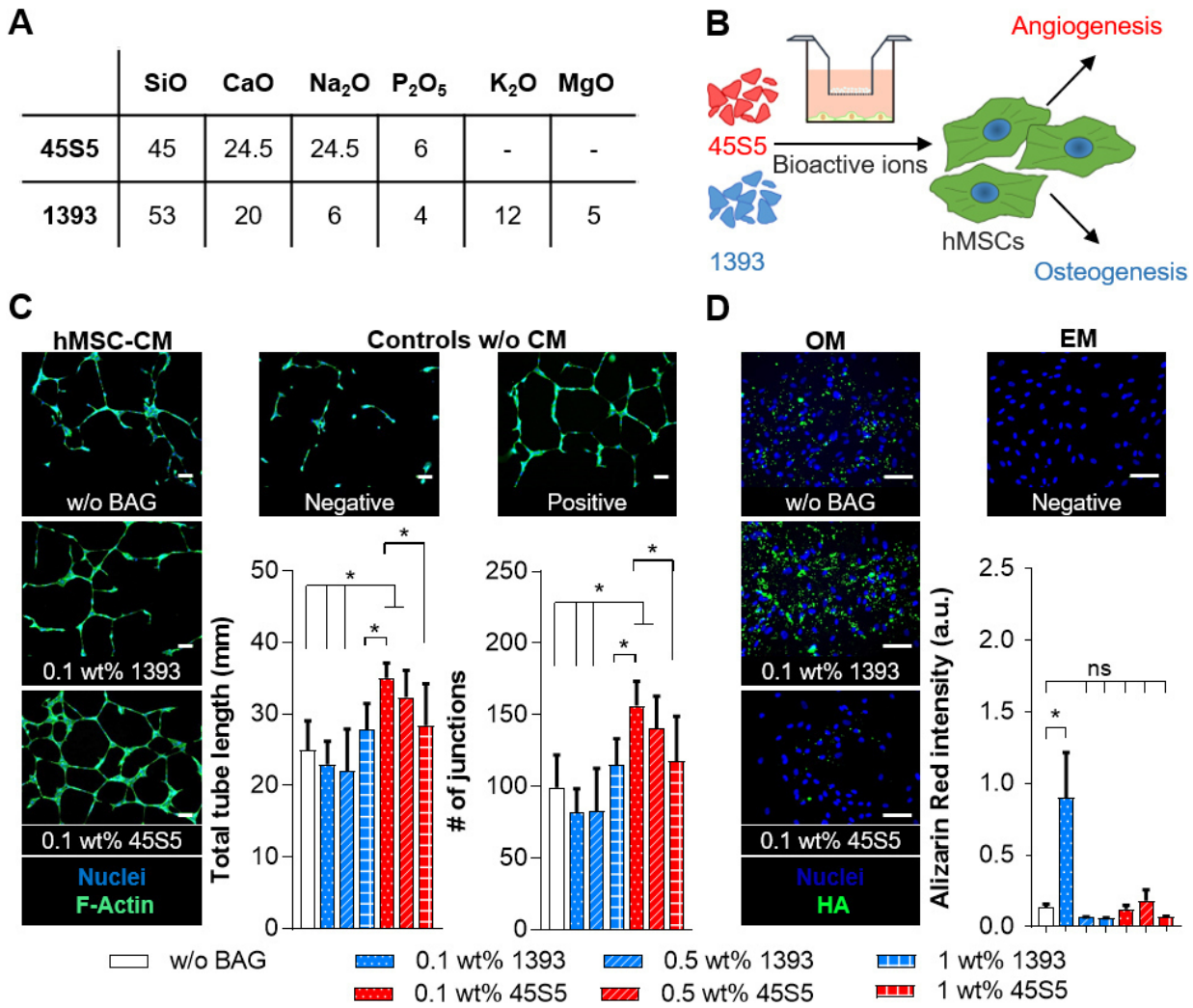


**Figure 5. Angiogenic and osteogenic response of hMSCs upon exposure to ionic dissolution products of 45S5 and 1393 commercial bioactive glasses (BAG) at different concentrations. (A)** Composition (wt. %) of 45S5 and 1393 BAG, adapted from [24]; **(B)** Schematic representation of the experimental set-up; **(C)** Representative images (green= F-Actin, blue= nuclei) of 2D-tube formation assay using CM of hMSCs after exposure to 1393 and 45S5 ionic dissolution products on HUVECs. Endothelial Basal medium (EBM) served as negative control, addition of supplemental growth factors (endothelial growth medium (EGM)) as positive control, CM conditions were generated in EBM. Tube length and number of junctions were quantified; n= 9. **(D)** Representative images of OsteoImage-stained hydroxyapatite (HA; green) and nuclei (blue) at 14 days post osteogenic induction (osteogenic medium, OM) with continuous exposure to 45S5 and 1393. Cells cultivated in expansion medium (EM) or OM served as negative or positive control, respectively. Quantification of matrix mineralization by Alizarin Red S staining and measurement of optical density of dissolved matrix. n=4. **(C-D)** Cell culture experiments were carried out by Dr. Taimoor H. Qazi and me, microscopy images were prepared and taken by Dr. Taimoor H. Qazi. Scale bar= 100 µm. One-way ANOVA with Tukey's post-hoc test was performed.* $p \leq 0.05$. Adapted from [16].

3.1.2. Biodistribution of fluorophore-labelled MBG – low dispersion is beneficial for local application

Within the MOZART project, binary $SiO_2$-CaO MBG developed by POLITO and FAU were employed as the base MBG carrier that can additionally be doped with therapeutic ions for the bone healing application. In contrast to several studies working *in vivo* with bioactive glasses as scaffolds or nail/ rod/ scaffold coatings, the MBG were applied as nano- to micron-sized spheres in the bone healing study. This small size could result in quick distribution within the organism, and in low material and cargo retention at the targeted treatment site. Hence, after *in vitro* biocompatibility assessment according to ISO norms by NBR, I conducted a biodistribution study by subcutaneously injecting MBG suspension in the nuchal fold (Figure 6 A). To track the potential dispersion, a far-red to near-infrared fluorophore (DY-677) was covalently bound to the MBG, allowing the detection of the MBG within the organism. I performed longitudinal imaging after injection and at 6, 24 or 72 hours post injection, followed by harvesting and imaging of the injection site, selected organs (selection based on [25]) and urine (Figure 6B). I observed no systemic dispersion of the MBG, since no fluorescence signal could be detected in the organs or the urine at all investigation time points (Figure 6C), while longitudinal signal intensity was continually strong at the injection site. Hence, the MBG remain local, rendering the MBG feasible for local application in a fracture scenario. Moreover, comparing the images taken immediately after injection and at the final time point, the fluorescent area in the nuchal fold reduced in size which could be explained by sedimentation and/ or aggregation of the MBG. Histological preparations of tissue from the injection site (Figure 6D) demonstrated immune cell infiltration into the area of MBG accumulation, that evokes a slight foreign-body response, as well as the specific fluorophore-signal of the tagged MBG. No major adverse events (severe loss in body weight, behavioral changes etc.) were recorded. The low dispersion rate is beneficial for local treatment approaches as it reduces the risk for off-target and systemic side effects, moreover, the MBG are tolerated by the organism upon local application. Therefore, the MBG were utilized in the subsequent studies.

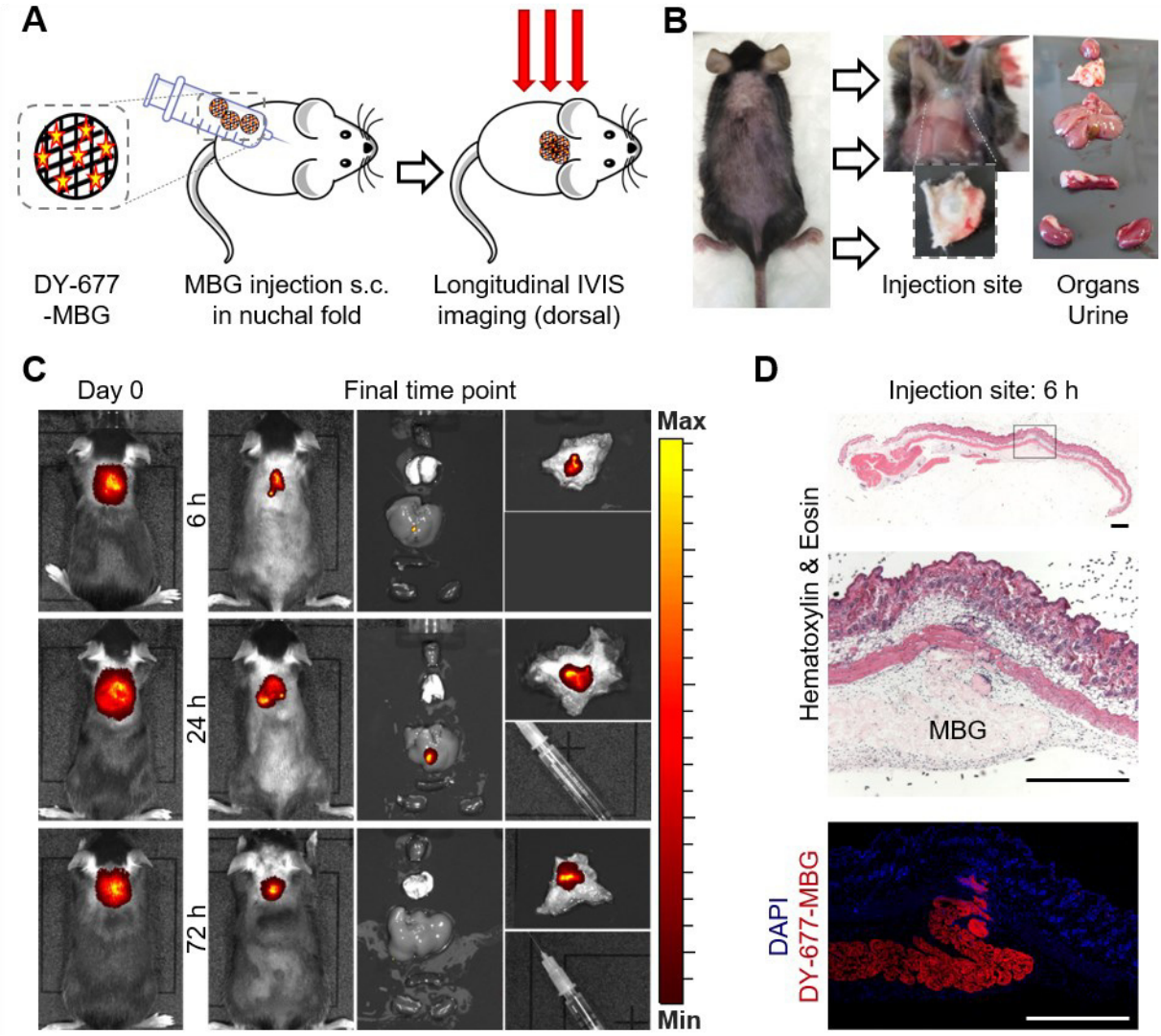


**Figure 6.** ***In vivo*** **biodistribution of subcutaneously (s.c.) injected DY-677-labeled MBG monitored by longitudinal IVIS imaging in mice. (A)** Schematic/ photographic representation of the study set-up at Day 0 and **(B)** at the final time point 6, 24 and 72 hours post injection. **(C)** Representative overlay IVIS images right after injection (Day 0) and at the final time point. At the final time point, except for an occasional fluorescence signal in the gall bladder (likely a mixed effect of minor autofluorescence of gall bladder tissue and traces of free DY-677 that preferentially accumulate in the gall bladder [26]), no accumulation of fluorescence was detected in selected organs (middle panel) or urine (right panel, bottom row per time point); the fluorescence signal remained exclusive to the injection site (right panel, top row per time point). n= 6 animals per time point. **(D)** Representative histological H&E-stained section of the injection site, boxed area is magnified in the middle image. Fluorescence signal of DY-677 (red) is distinct for the area of MBG accumulation as shown by fluorescence microscopy (blue= nuclei/ DAPI; LSM710, Zeiss). Scale bar: 1 mm, unpublished data.

### 3.1.3. *In vivo* pH-triggered substance release

The pH is tightly regulated *in vivo*, with the physiological pH of blood ranging between 7.35 and 7.45. Perturbations of homeostatic pH can be caused by diseases, for example in cancer where cancer cells preferentially utilize anaerobic respiration even in the presence of sufficient oxygen (Warburg effect)

or in hypoxic situations, leading to the generation of lactate that can acidify the local environment (discussed in [21]). Bone fracture also results in blood vessel rupture and hypoxia [27], and the associated local acidification of the fracture site has been described in the literature [11, 12]. Therefore, a pH-triggered substance release approach is an attractive candidate for localized and targeted interventions in the context of bone healing, with local, injury-dependent pH alterations acting as an endogenous trigger for substance release.

*3.1.3.1. pH-triggered drug release system validation – SIP pH-responsiveness confirmed in vivo*

The pH-sensitive SIP coating was previously developed by UCM [28], for this study it was grafted on C1Sph (average size of spheres: 150 nm, Demokritos) as another biomaterial carrier selected for the MOZART project (publication 1, [15]). For the *in vivo* validation, I injected SIP-coated C1Sph (C1Sph-SIP) loaded with a fluorophore (Ruthenium, Ru) into the nuchal fold and imaged longitudinally before, after, as well as at 24, 48 and 96 hours post injection (Figure 7A1). As the black carbon spheres are opaque and the cargo is loaded into the mesopores, no fluorescence-signal is emitted as long as the SIP coating remains intact on the surface; only the release of the fluorescent cargo can be detected as fluorescence signal. To enable the detection of potential leakage of the SIP without exogenous pH stimulus and to investigate the response to the C1Sph-SIP, C1Sph-SIP were injected s.c. without application of an exogenous pH stimulus. Over the entire testing period of 96 hours, no biomaterial-dependent fluorescence signal in the nuchal fold could be observed (Figure 7A1), while H&E-staining of the injection site (Figure 7A2) revealed only a minor foreign body response with mild cell infiltration (Figure 7A2_I) when compared to the cell infiltration into the injury site (Figure 7A2_II) caused by the needle during injection. Hence, C1Sph-SIP can be considered biocompatible and the SIP coating remained intact, keeping the mesopores closed under steady-state conditions. Subsequently, I investigated the pH responsiveness and the release kinetics of C1Sph-SIP upon exposure to an acidic pH solution (pH 4, Figure 7B) *in vitro* and *in vivo*. Figure 7C shows the release of fluorescent cargo after short- or long-term triggering (30 min and 24 h) in acidic pH solution compared to physiological pH environment (pH 7.4). Both triggering intervals induced significant cargo release, moreover the C1Sph-SIP were re-immersed in physiological fluid (pH 7.4) after the triggering period. A continuous cargo release could be observed for both conditions even after removing the pH stimulus, indicating that short-term triggering could be sufficient to induce adequate pore opening and cargo release. *In vivo*, the C1Sph-SIP were injected s.c., followed by application of an acidic pH 4 or pH 7.4 control solution into the injection site. The cargo release was monitored via longitudinal IVIS imaging. In line with the *in vitro* experiment (Figure 7C), the majority of cargo release occurred during the low pH triggering period and was not detectable for the control condition. Continual release could be observed at 24 and 72 hours post low pH triggering (Figure 7D).

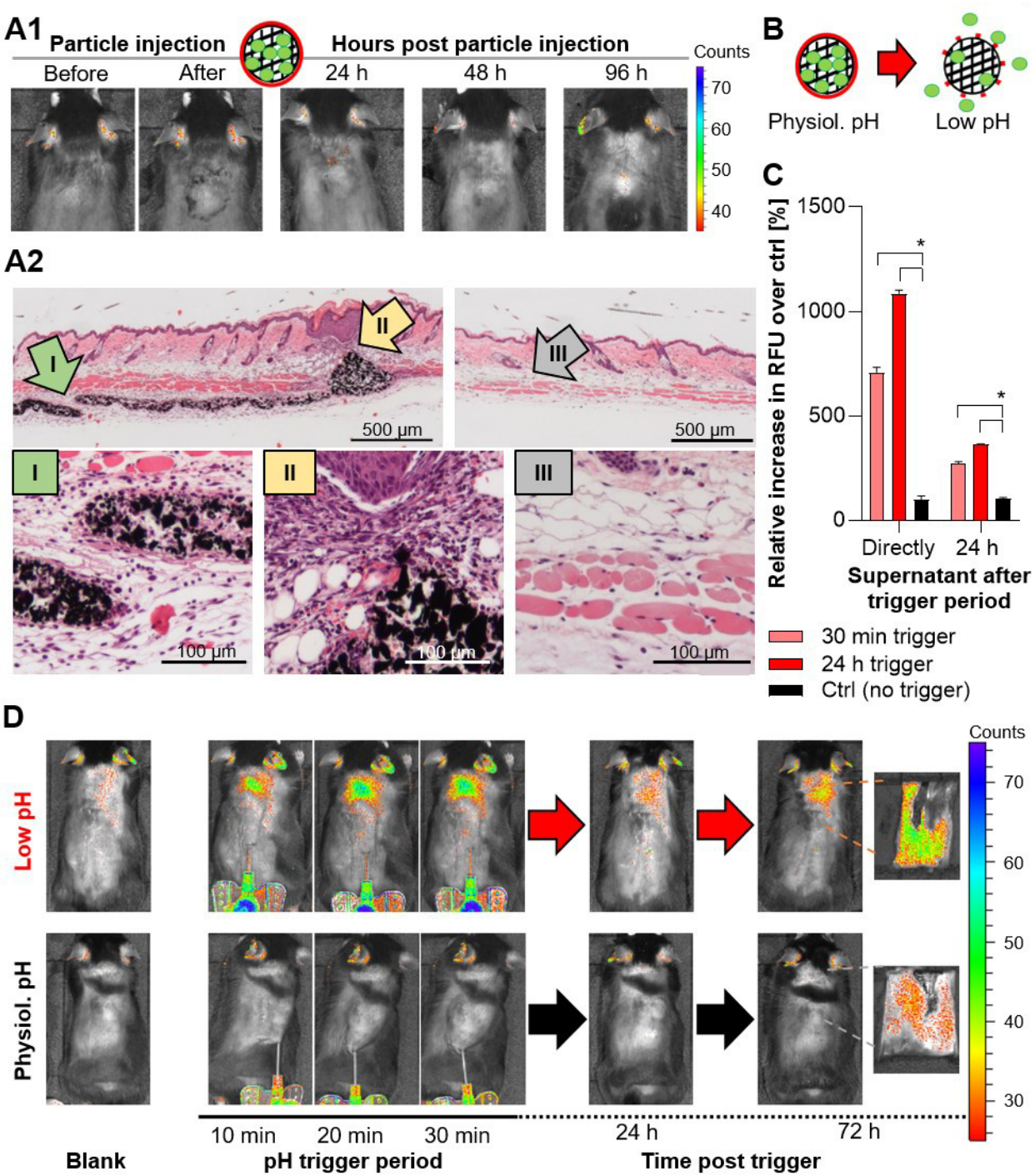


**Figure 7.** ***In vivo*** **validation of SIP-coated mesoporous carbon spheres (C1Sph-SIP) containing fluorescent cargo after s.c. injection by longitudinal IVIS imaging in mice. (A1)** Behavior of Ruthenium (Ru)-loaded C1Sph-SIP in the absence of an exogenous pH trigger. Representative overlay IVIS images before and up to 96 hours post s.c. injection in nuchal fold. No fluorescence signal could be detected over the entire testing period, indicating that the SIP remained intact and the fluorescent cargo entrapped in the C1Sph mesopores; n= 3. **(A2)** Representative histological H&E-stained sections of the injection area (left) or control skin (right), black particles represent C1Sph-SIP, 10x magnification. **(I, II)** immune cell infiltration in response to the biomaterial **(I)** or to the tissue damage induced by the injection **(II)**, compared to control skin **(III)**, 40x magnification. **(B)** Schematic representation of SIP degradation by acidic pH, resulting in pore opening and cargo release. **(C)** *In vitro* test on time-dependent SIP

degradation. 30 min or 24 hours pH triggering in acidic pH environment (pH 4) resulted in significant fluorescent cargo release (direct measurement of supernatant at the end of the trigger period) that continued even after returning the C1Sph-SIP into a pH 7.4 environment (24 h post trigger period). Fluorescence was detected in the material-free supernatant by IVIS imaging and quantified using a plate reader (Tecan Infinite Pro 200, ex/ em 450/ 620 nm); n= 3; for 24 h trigger n= 2; unpaired, two-tailed Student's t-test, * $p \leq 0.05$. **(D)** Similar set-up as in **(A),** but additional administration of acidic (top) or physiological (bottom) pH solution into the injection site, IVIS imaging during the triggering period and up to 72 hours post injection revealed fluorescent cargo release for the low pH triggered animals that was hardly detected for the control condition; n=3. (**A-D**) adapted from [15] (publication 1).

This *in vivo* study revealed excellent biocompatibility of the C1Sph-SIP, as well as demonstrated a similar *in vitro* and *in vivo* response to pH-triggering. Thus, follow-up studies on pathology-dependent local acidifications as seen in e.g. florid infections with *Staphylococcus aureus* (*S. aureus*, see Figure 9) are feasible and are currently performed.

*3.1.3.2. Identification of local target pH values after musculoskeletal injury*

In parallel to the *in vivo* validation of biocompatibility and pH-triggered responsiveness of the C1Sph-SIP, the extent of local acidification after bone fracture was determined to understand the suitability of the pH-triggered drug release strategy, employing the SIP coating, in bone healing. A literature search uncovered conflicting local pH values, mostly neglecting the early time points after fracture [12]. These early time points are highly relevant for the present novel treatment strategy with the intention to counteract healing disturbances that can occur at initial stages of the healing process. Hence, an *in vivo* study in rats was conducted (publication 2, [21]). Two size-matched musculoskeletal hematomas formed after osteotomy and muscle trauma were created within the same animal, allowing intra-individual comparison and identification of tissue-dependent effects, and the local pH was measured at 4, 10, 24 and 48 hours post injury. Local pH in both hematomas acidified significantly to mean pH values of $6.69 \pm 0.26$ (bone) and $6.89 \pm 0.34$ (muscle) compared to the pH of peripheral blood (pH of 7.35 – 7.45) (Figure 8A1, 2). Regression analysis on the local pH in osteotomy versus muscle hematoma showed no correlation of the pH values of both tissues with an $R^2$ of 0.057 (Figure 8A3). Physiologically, blood vessel rupture evokes local hypoxia and the oxygen shortage drives the cellular switch from aerobic to anaerobic respiration, thus, lactate is produced during lactate fermentation. Lactate can be transported out of the cell; thereby external lactate accumulation leads to local acidification of the ischemic environment (discussed in [21]). Accordingly, the large inter-individual variability in local pH across all time points (Figure 8A1, 2) was hypothesized to be dependent either on the cellular density within the hematoma, with more cells producing more lactate, or on respiratory metabolic activity. While local pH was not found to be correlated to cellular density (Figure 8B), the metabolomic analysis of osteotomy hematomas harvested 10 and 24 hours post osteotomy unraveled a link between tricarboxylic acid cycle (TCA cycle) activity and local pH (Figure 8C).

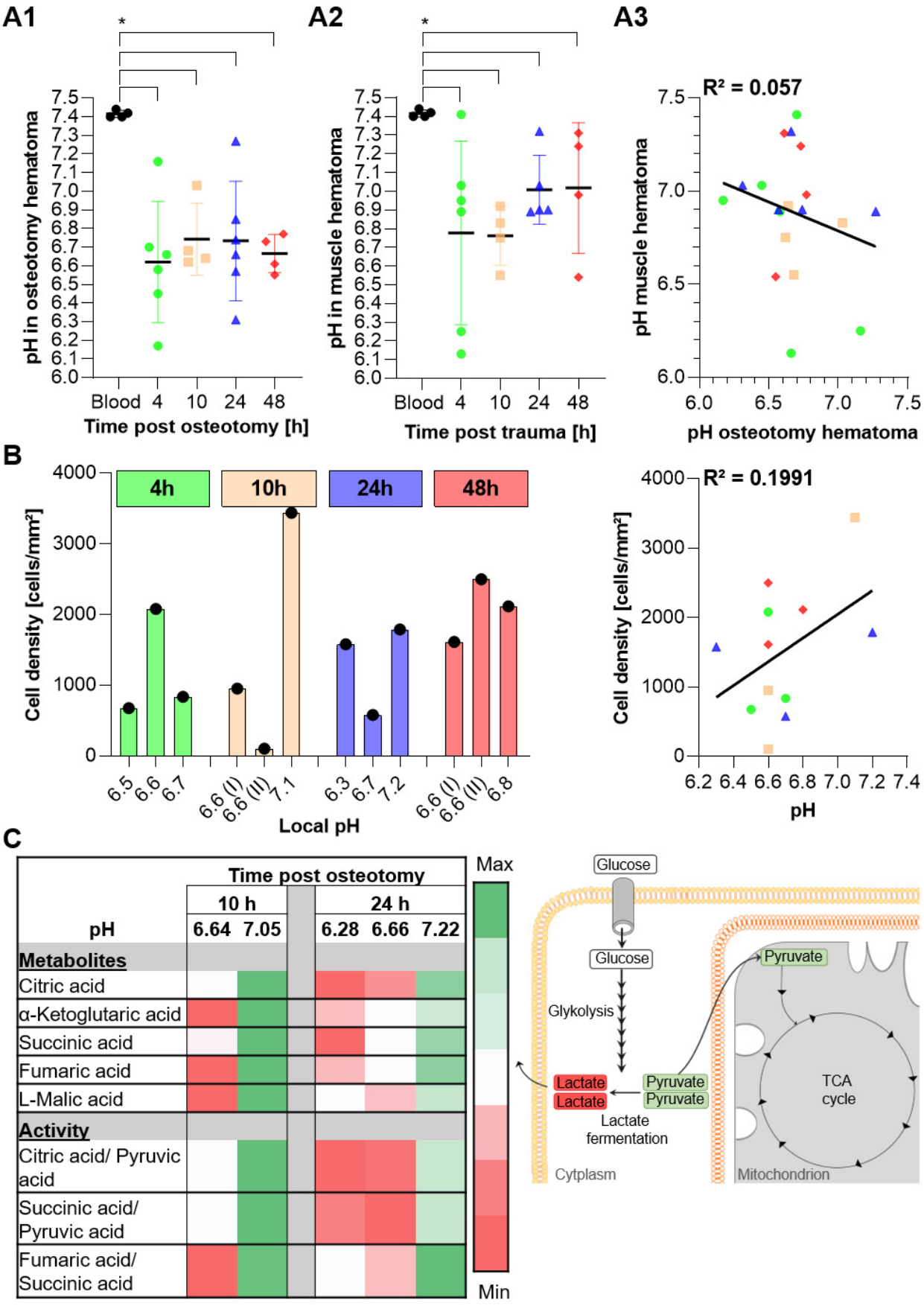


**Figure 8. Identification of target pH values after osteotomy or muscle trauma and quantification of cellular density and relative TCA metabolite abundance. (A)** pH measurement at 4 (green), 10 (orange), 24 (blue) and 48

(red) hours post osteotomy **(A1)** and muscle trauma **(A2)**. Shown are scatter plots with line at mean, each dot represents the pH value of one animal, n= 4-6, two-tailed Mann-Whitney U test was performed using the control group (blood) as comparator, * $p \leq 0.05$. **(A3)** Linear regression analysis of pH in osteotomy versus muscle hematoma per animal, both parameters passed the D'Agostino-Pearson normality test, enabling Pearson correlation coefficient calculation ($R^2 = 0.057$). **(B)** Quantification of cellular density (each bar represents one analyzed hematoma) revealing no correlation with local pH, n= 3 per time point (Linear regression analysis as in **A3**). **(C)** Heat-map of relative metabolite abundance and local pH, showing higher TCA activity in hematomas with higher pH, n= 2/ 3 for 10/ 24 hours timepoint, respectively. Simplified scheme of glucose metabolism to pyruvate and following an-/aerobic respiratory pathway. **(A-C)** Adapted from [21] (publication 2).

The higher the TCA cycle activity, the higher the local pH, indicating that the individual metabolomic activity could be causative for the variability in local pH. The identified *in vivo* target values for pH-sensitivity of the biomaterial did not match the sensitivity of the previously validated SIP coating, as SIP degradation occurs at pH values ≤ 5. Therefore, the SIP coating was discontinued in the context of bone healing. Nevertheless, pH-responsive coatings sensitive to more subtle changes as detected upon musculoskeletal injury could be added onto the technology platform in the future to enable stimuli-responsiveness in the bone healing context.

### *3.1.3.3. Local acidification upon infection – application opportunity for pH-sensitive drug release systems*

Despite the discontinuation of the SIP coating for bone healing application, I identified orthopedic infections as another cause for local acidifications, since bacterial metabolic activity can alter the external environment by secretion of acidic products. In this context, different tissues that would usually be discarded during endoprosthesis surgeries (Figure 9A) were pH measured directly after removal, grouped into tissue categories and sorted based on their infection status. Overall, comparing aseptic and septic tissue groups with each other, a trend towards decreases of mean pH was observed for the septic groups, for which the variability in measured pH was considerably larger, as exemplified by focusing on the fluid group with a mean pH of 7.31 ± 0.12 in the aseptic cases versus a pH of 7.21 ± 0.29 in septic patients (Figure 9A). In order to obtain more standardized human samples, another study focused on synovial punctuates of patients with suspected infection and subsequent pH measurements, which revealed a significant acidification of synovial fluids infected with *S. aureus* (Figure 9B). These findings form the basis for a manuscript currently under preparation. For this, I and MOZART partners are investigating SIP degradation of C1Sph-SIP loaded with different antibiotics due to *S.aureus*-induced acidification (Figure 9C). A successful infection-dependent release of antibiotics would demonstrate a possible application route of the pH-triggered drug release system for the on-demand treatment of infections.

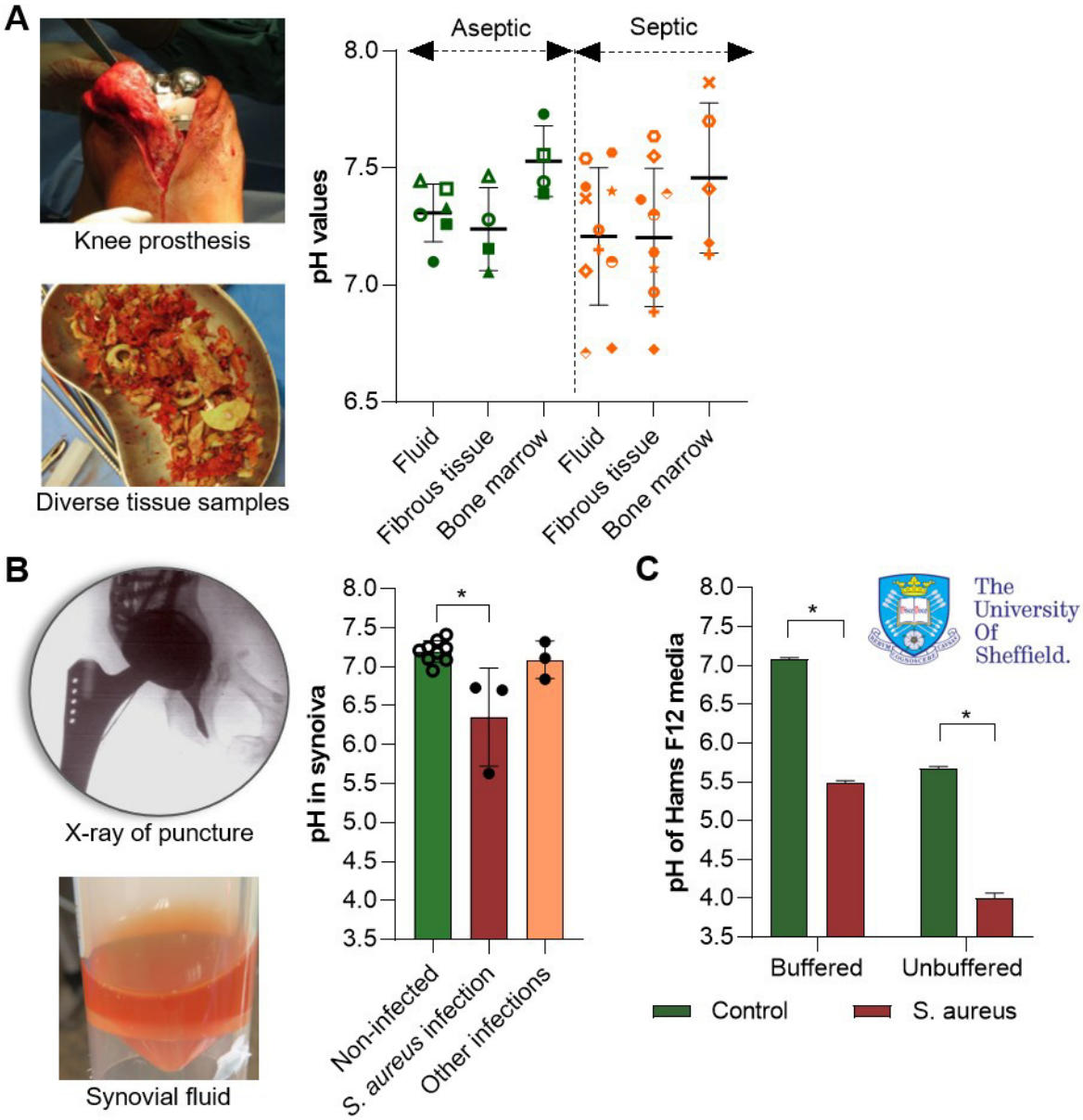


**Figure 9. Bacterial infections can acidify the local environment *in vitro* and *in vivo*. (A)** Representative images of tissues sampled from endoprosthetic surgeries and pH measurement in different tissue categories (fluid, fibrous tissue and adjacent bone marrow) combined with microbial burden analysis, n= 17 patients, shown are mean ± SD, each symbol represents tissue samples of one patient. **(B)** Radiographic image of human joint puncture and photographic image of harvested synovial fluid, followed by pH measurement and microbial burden evaluation; n= 15 patients. **(C)** Courtesy of USFD: Acidification of Hams F12 medium (buffered and unbuffered) after *S. aureus* inoculation and overnight cultivation. n= 3. **(A-B)** Mean ± SD are shown, Mann-Whitney U test, **(C)** student's t-test was performed; * $p \leq 0.05$. Manuscript in preparation.

### 3.1.4. Handling and application of biomaterial composite – Hydrogel qualifies as embedding material applied via injection

Before progressing to the final bone healing application involving the composite biomaterial, I validated the SHP407 thermosensitive hydrogel in terms of injectability into an organism (cadaver

study) with physiological body temperature and subsequent gelation (publication 3, [17]). Injection (Figure 10A) resulted in low dispersion and proper solidification of the gel, both after *s.c.* injection in the nuchal fold (Figure 10B) and administration in an osteotomy gap (Figure 10C). Moreover, both parameters were evaluated and compared among three groups: mesoporous carrier with fluorescent cargo (Ru) dispersed in physiological fluid (Figure 10D-E, Animal 1), SHP407 alone (Animal 2) and the composite of SHP407 and carrier (Animal 3, 4). A similar behavior of the hydrogel and the composite was observed with low dispersion, proper gelation and signal transmission of the fluorescent cargo (Figure 10E), allowing progression to the bone healing study.

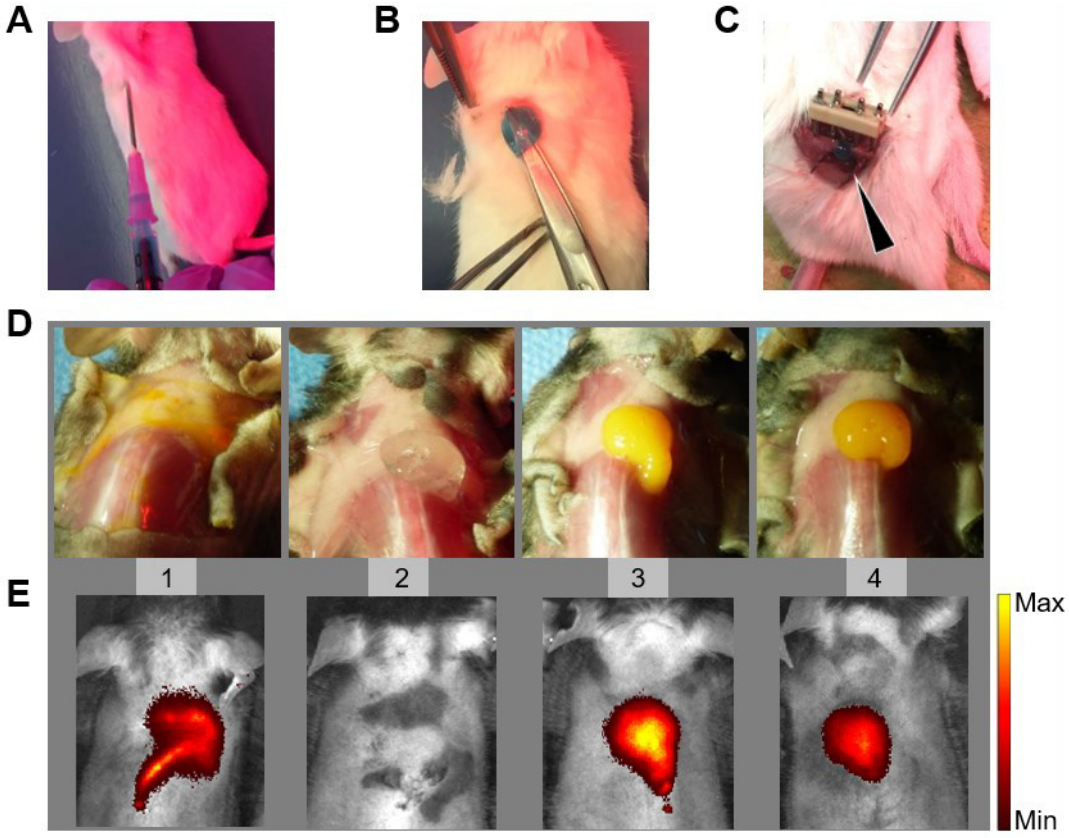


**Figure 10. *Ex vivo*/ *in situ* injection and solidification of SHP407 thermosensitive hydrogel alone or in composite with mesoporous carrier and fluorescent cargo in murine cadavers with physiological temperature. (A)** SHP407 s.c. injection via G18 needle in nuchal fold **(B)**, hydrogel solidity test 5 minutes post injection by lifting-up the hydrogel **(C)** and solidification in confined osteotomy gap area. n= 2 murine cadavers. **(D-E)** Comparative injection and gelation of carrier and cargo in physiological fluid (1), SHP407 (2), composite (3, 4), photographic images **(D)**, as well as IVIS images to detect the fluorescent cargo Ru and transmission of fluorescence through hydrogel **(E)**, n= 4 murine cadavers. **(A-E)** Adapted from [17] (publication 3).

### 3.2. Functional validation of technology platform: Selection of therapeutic ions and drugs and local application via hybrid biomaterial in bone healing

In order to improve bone healing using this technology platform, several therapeutic ions and drugs with pro-osteogenic, pro-angiogenic, anti-inflammatory and anti-microbial properties were selected based on extensive literature search performed within my PhD project, after which I analyzed their cytocompatibility and pro-regenerative response on primary MSCs. After I identified suitable ion candidates, these were doped into the MBG network and investigated by NBR in terms of biocompatibility, osteogenic and inflammatory responses in cell lines according to ISO norms. In the following, my investigations on one attractive candidate for each, therapeutic ions and drugs, will be described in more detail.

#### 3.2.1. Therapeutic ion candidate Strontium as a pro-osteogenic therapeutic ion

It is known that Strontium (Sr) has a strong effect on osteoanabolism and -catabolism, as it stimulates osteoblast function and osteoprotegerin (OPG) expression [29]. High OPG expression leads to an inhibition of osteoclast formation due to antagonistic binding to receptor activator of nuclear factor-κB ligand (RANKL). Since RANKL-RANK receptor interaction on osteoclast precursor cells are essential for osteoclast differentiation, Sr inhibits osteoclastogenesis and acts pro-osteogenically [29]. Strontium renelate is used clinically to treat severe cases of osteoporosis in elderly patients. Moreover, strontium has been assigned anti-inflammatory properties by antagonizing nuclear factor-κB (NF/κB) signaling [30], both features render Sr a first-choice candidate for implementation in the bone healing study.

Within my PhD project, the pro-osteogenic effects of Sr were confirmed at concentrations that did not affect cell metabolic activity of primary bone marrow MSCs (Figure 11A, B). Hence, this therapeutic ion was included in the bone healing study.

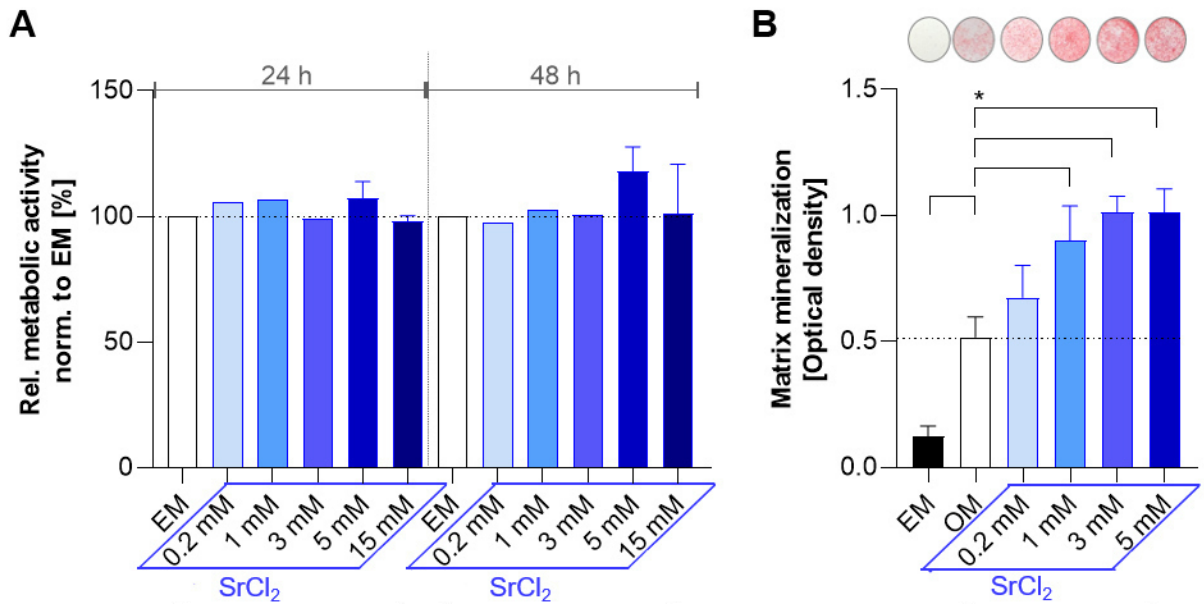


**Figure 11. *In vitro* response of rMSC to Strontium chloride ($SrCl_2$). (A)** Relative metabolic activity analyzed by Presto Blue conversion and fluorescence measurement. Normalization to positive control (cells cultivated in EM); n= 4 biological replicates (EM, 5mM Sr), n= 1 (0.2- 3 mM Sr), n= 3 (15 mM Sr). **(B)** Quantification of matrix mineralization via Alizarin Red S staining and absorption measurement at 14 days post osteogenic induction (OM). Representative images of stained wells are shown in the top panel. Comparison to positive control (cells cultivated in OM); n= 2 biological replicates. **(A, B)** ≥3 technical replicates per biological replicate; one-way ANOVA with Dunett's multiple comparison test, * $p \leq 0.05$. Unpublished data.

3.2.2. Drug candidate N-Acetylcysteine as a pro-osteogenic, pro-angiogenic and ROS-scavenging drug

N-Acetylcysteine (NAC), a known reactive oxygen species (ROS) scavenger (and inhibitor of NF/κB activation), has a broad clinical use ranging from induction of mucolysis to treating acetaminophen overdoses and utilization in cardiovascular diseases [31]. It is approved by the U.S. Food and Drug Administration (FDA) and European Medicines Agency (EMA) with a proven clinical track record and is cost-effective. In the context of bone healing, a previous study revealed increased bone formation and improved microarchitecture of newly formed bone in a rat osteotomy model in the presence of NAC [32]. Within this previous study, NAC was supplemented continuously over the healing time via the drinking water, hence, no direct information on the required local dose could be obtained.

In my PhD project, the pro-osteogenic effects of NAC were studied on primary hMSCs (Figure 12A-C), while the pro-angiogenic effects were investigated using HUVECs (Figure 12D).

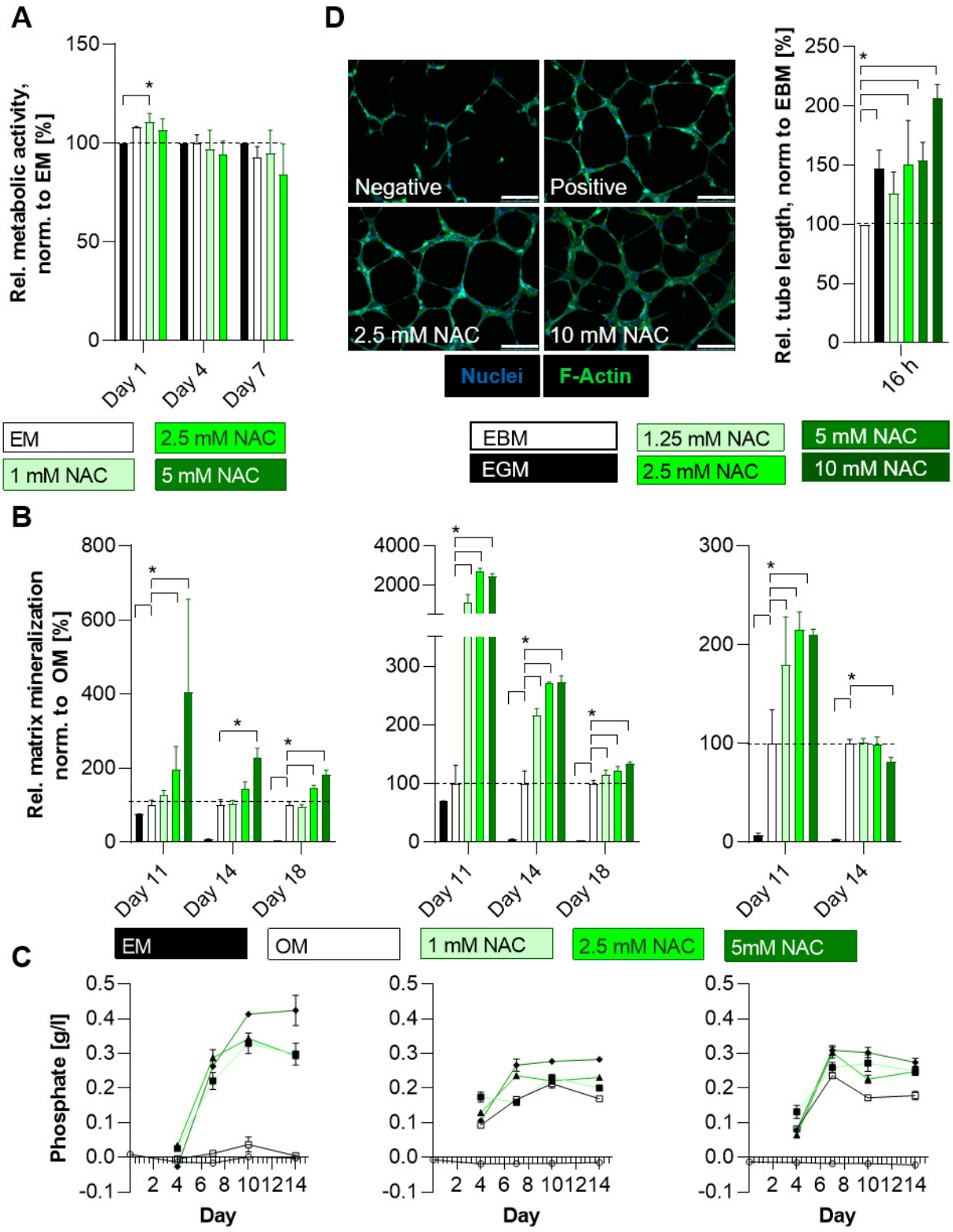


**Figure 12.** ***In vitro*** **response of hMSCs and HUVECs to N-Acetylcysteine (NAC). (A)** Relative metabolic activity analyzed by Presto Blue assay and normalization to EM. **(B)** Relative matrix mineralization as quantified by Alizarin Red S staining and normalization to positive control (OM) at 11, 14 and 18 days of osteogenic induction (OM was used for NAC conditions). Each graph shows the response of hMSCs for one donor individually. **(C)** Quantification of free inorganic phosphate in the supernatant over 14 days of osteogenic induction, supernatant of cultures used for **(B)** was utilized. Each graph shows the response of hMSCs for one donor individually. For **(A-C)** n= 3 different hMSC

donors. **(D)** Representative images of 2D-tube formation assay using HUVECs and quantification of relative tube length (Scale bar: 250 µm) stained using DAPI (blue) and F-Actin (green), normalization and comparison to negative control (EBM, NAC supplemented in EBM), EGM: positive control. n=4 (controls, 2.5 mM NAC), n= 3 (1.25, 5 mM NAC), n= 2 (10 mM NAC) independent experimental repetitions. Shown are mean ± SD. **(A-D)** ≥3 technical replicates per biological replicate/ experimental repetition; one-way ANOVA with Dunett's multiple comparison test was performed, * p≤ 0.05. Unpublished data.

Metabolic activity remained largely unaffected by NAC administration at concentrations of up to 5 mM over 7 days (Figure 12A). Despite large donor-specific variations, accelerated matrix mineralization was observed upon continuous supplementation of NAC to OM with the strongest mineralization detected at concentrations of 2.5 and 5 mM (Figure 12B). In all cases, the difference between OM control and NAC-treated groups was maximal at early time points and reduced over time, thus, induction of mineralization occurs earlier due to NAC supplementation in OM. Inorganic phosphate levels in the supernatant, a pre-requisite for matrix mineralization, were found to be highest in the 5 mM NAC group, which strengthens the finding of accelerated matrix mineralization (Figure 12C). The administration of NAC to HUVECs in a 2D-tube formation assay (Figure 12D) in EBM indicated a pro-angiogenic effect of NAC since the relative tube length increased significantly compared to the negative control (EBM).

To investigate the ROS scavenging function of NAC, murine bone marrow cells (mBMCs) were isolated from femora and ROS levels were quantified. Pre-treatment with NAC prior to ROS-induction decreased ROS levels significantly in mBMCs from control femora, as well as from contralateral and osteotomized femora 3 days post osteotomy (Figure 13A), indicating that NAC has protective activity against oxidative stress. The observed pro-osteogenic, pro-angiogenic and ROS-scavenging features prompted the design of a proof-of-concept *in vivo* study in mice, focusing on local application and dosing of NAC (Figure 13B-D). The findings revealed a positive effect of the local, one-time NAC administration on bone formation with higher concentrations (25 µg total amount) being more beneficial as observed radiologically in reconstructed µCT images (Figure 13C) and histologically by MOVAT's pentachrome staining of the fractured femora (Figure 13D). Using these results, target concentrations for the MOZART bone healing study were defined.

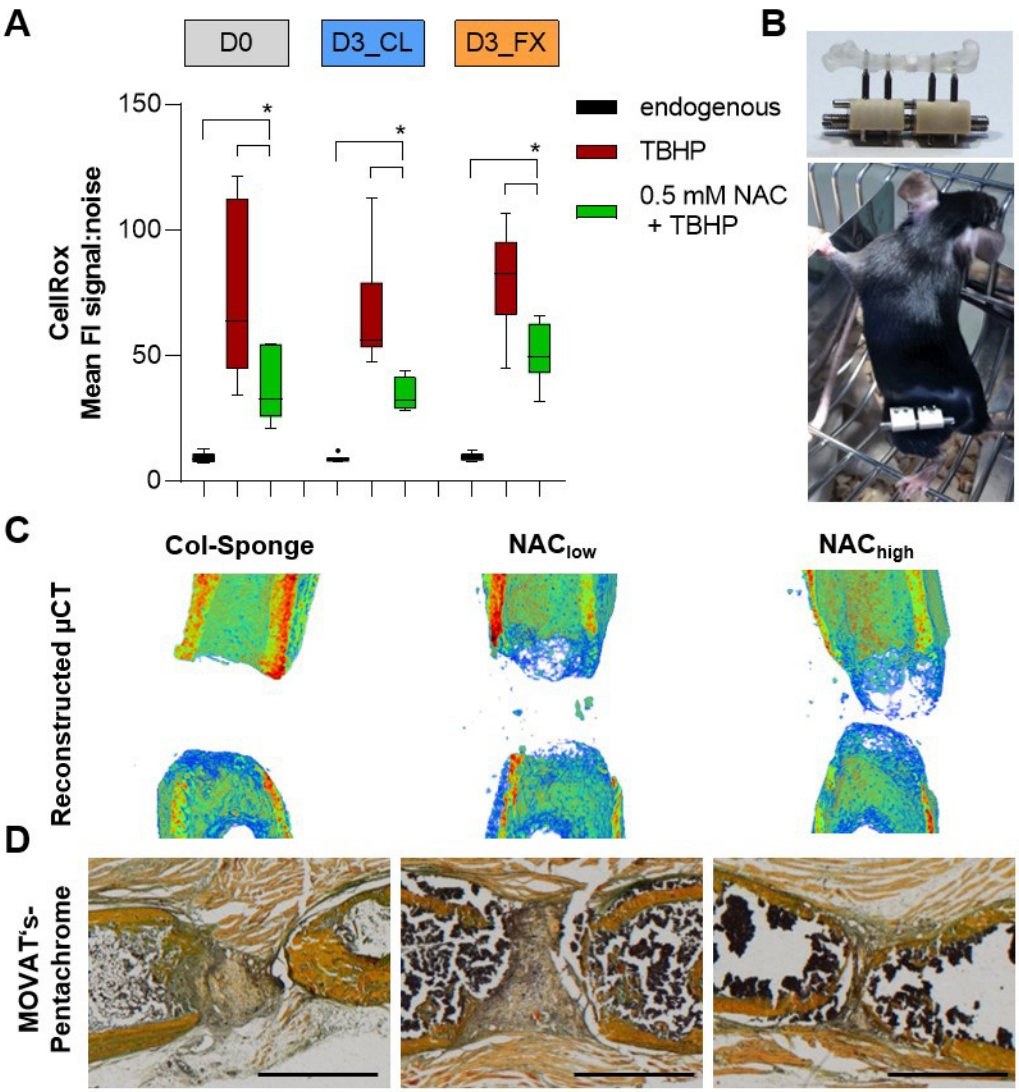


**Figure 13. *Ex/ in vivo* response to NAC treatment. (A)** *Ex vivo* measurement of ROS levels from murine bone marrow cells (mBMCs) isolated from femora: endogenous (black); after tert-butyl hydroperoxide (TBHP) stimulation to induce ROS (red); after pre-treatment with NAC, followed by ROS induction (green). Shown are ROS levels from mBMCs of control animals (D0) and osteotomized animals (contralateral: CL and fractured: FX) 3 days post osteotomy. Tukey box plot distributions are shown with line at median, n= 6-7 animals per group, two-tailed Mann-Whitney U test was performed using the 0.5 mM NAC group as comparator, * $p \leq 0.05$. **(B)** Images of external fixator with distractor to create standardized critical-sized femoral 1.4 mm defect and of murine animal model with mounted distractor. **(C)** Representative reconstructed µCT-images and **(D)** histological MOVAT's pentachrome staining 21 days post osteotomy and local application of an absorbable collagen sponge without or with two different concentrations of NAC (low: 1 µg/µl/ high: 10 µg/µl; 2.5 µl total volume) in the osteotomy gap. Scale bar: 1 mm, unpublished data.

### 3.2.3. Bone healing study: BHD with Strontium/ Copper and NAC – individual effects of ions and drugs detectable

Having identified promising ion and drug candidates, these candidates were doped and loaded in the MBG platforms/ BHDs and tested upon local application in a femoral osteotomy of a biologically

delayed rat healing model [33] (Figure 4). Drug release from MBG was confirmed by using the fluorescent drug Tetracycline (TCH) that binds to Calcium of newly deposited bone (Figure 14).

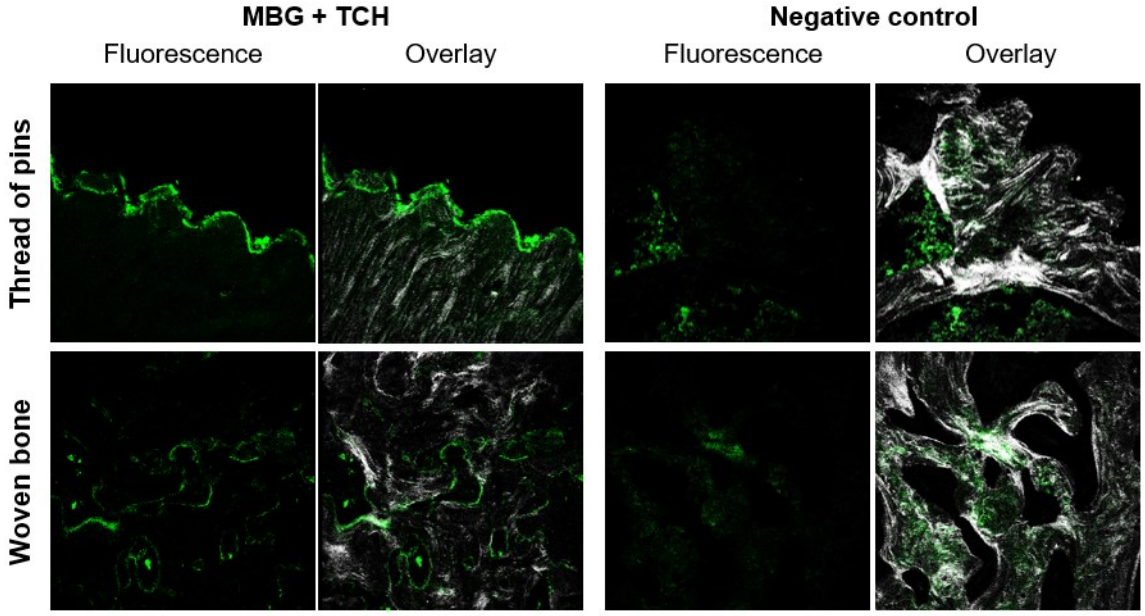


**Figure 14. Second harmonic imaging of rat femora treated with MBG loaded with Tetracycline hydrochloride (TCH) or control bone.** Top panel: image of the pin threads most proximal to the osteotomy gap, bottom panel: woven bone area within the osteotomy gap. Shown are images of fluorescence (ex/em: 488/ 493-537 nm) alone and as overlay with second harmonic imaging, depicting fibrillar collagen type I (ex/em: 910/ 450-460 nm). Both images were generated using Leica SP5 II microscope equipped with a Spectra Physics Ti:Sapphire laser (Mai Tai HP). The negative control revealed background fluorescence that is not specific for newly deposited bone. Conversely, for MBG + TCH the highest signal intensities were detected at the bone formation fronts. MBG were loaded with TCH to the maximum MBG loading capacity, carried out by FAU. Imaging was supported by Dr. Aaron X. Herrera Martin, Charité – Universitätsmedizin Berlin.

MBG loaded with NAC (~14 wt % loading) were doped either with Sr to intensify the pro-osteogenic and anti-inflammatory effect of NAC or with Copper (Cu) to enhance the pro-angiogenic potential [34] of the composite (Figure 15, for both ions: 2 molar % doping into MBG formulation). *Ex vivo* µCT analysis at 4 weeks post osteotomy revealed that the mean bone volume (BV) over total volume (TV; BV/TV) as well as the bone mineral density (BMD) was highest for the NAC treated groups (Figure 15A, B), although without statistical significance. Comparing pure MBG with both NAC groups, a subtle trend towards an increase in trabecular number (Tb.N.) and decrease in trabecular separation (Tb.Sp.) was detected for the NAC groups, which is in line with previous studies [32]. Moreover, the effects of both therapeutic ions could be identified via immunohistochemistry. Vessel-staining using the marker α-SMA yielded a trend towards an increase in relative vessel area for the pro-angiogenic group treated with NAC and Cu compared to NAC and Sr, while both groups presented with more vessels compared to the pure MBG group (Figure 15C), which can be attributed to the pro-angiogenic

activity of NAC. Quantification of bone residing, CD68+ osteoclastic cells resulted in the lowest mean value for the Sr-treated group (Figure 15D), reflecting the inhibitory effect of Sr on osteoclast formation [29].

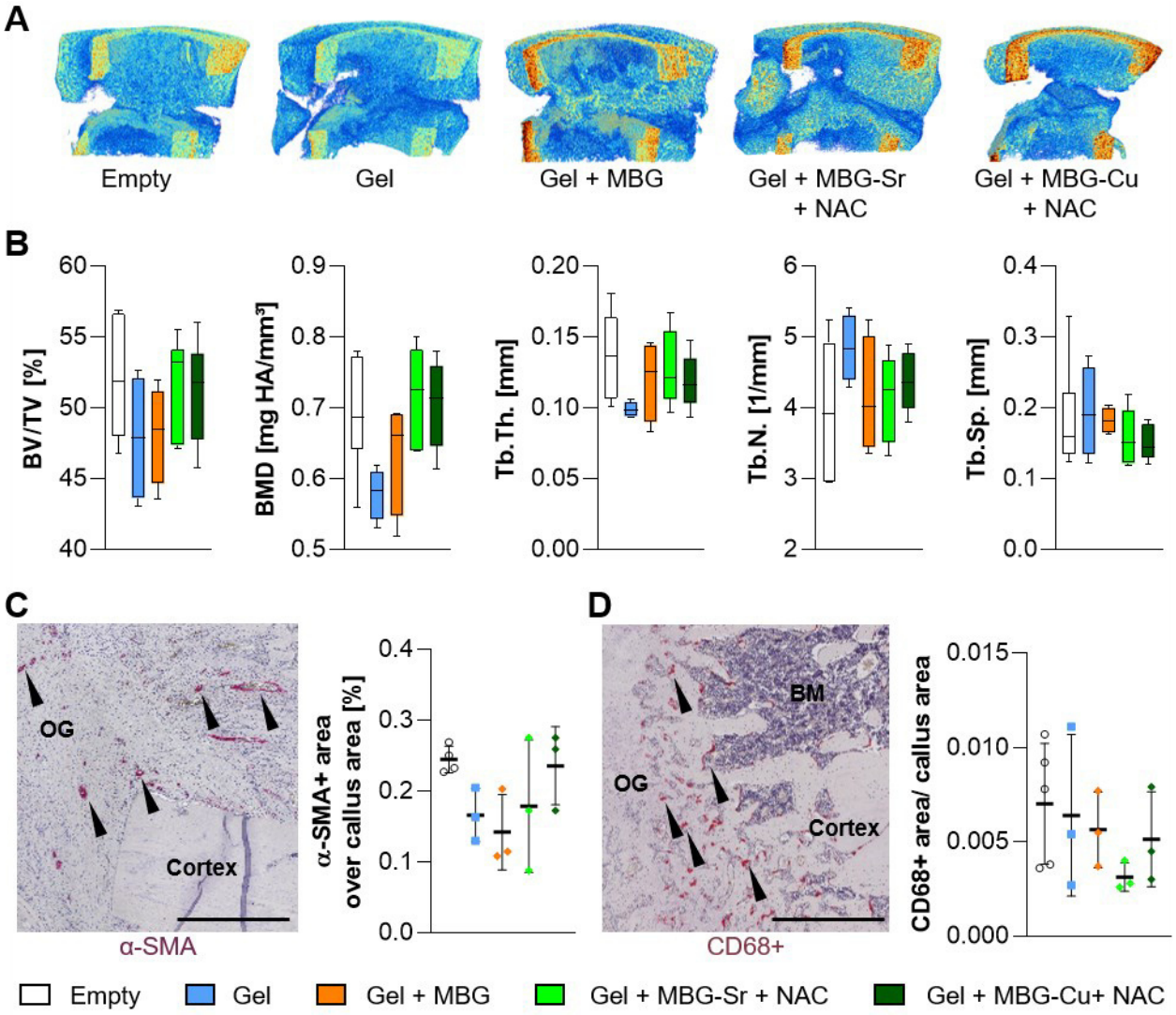


**Figure 15. *In vivo* bone healing evaluation 4 weeks post osteotomy for dual Strontium (Sr)/ Copper (Cu)-doped and NAC-loaded BHD in rat femoral osteotomy model of compromised healing. (A)** Representative, reconstructed *ex vivo* µCT images for control groups (no local treatment (empty), SHP407 (gel) and gel + pure MBG) and treatment groups (gel + Sr/ Cu-doped MBG + NAC load). **(B)** *Ex vivo* µCT analyses revealing a trend towards increases in bone volume over total volume (BV/TV), bone mineral density (BMD) as well as subtle microarchitectural (trabecular thickness (Tb.Th.), trabecular number (Tb.N.) and trabecular separation (Tb.Sp.)) changes in NAC-treated groups. n= 4-6 per group, Tukey box plot distributions are shown with line at median. **(C)** Immunohistological staining of α-SMA to detect vessel formation and **(D)** bone-residing osteoclastic CD68 cells indicating an increase in vessel area for the group treated with pro-angiogenic Cu and a decrease in osteoclastic cell abundance for the osteoclast-inhibiting Sr-treated group. **(C, D)** n= 3- 4 per group, scatter dot plots with mean ± SD are shown. scale bar: 500 µm. Legend applies for **(B – D)**. Unpublished data.

Although requiring fine-tuning of NAC and Sr/ Cu concentrations to yield stronger effects on the bone healing outcome, the observed trends can be considered a crucial and promising first step towards the development of a potent pro-osteogenic and pro-angiogenic composite.

3.2.4. Prolonged, low-dose BMP-2 release from MBG lead to superior healing

I selected BMP-2 as a positive control to demonstrate successful drug release from MBG since the release of BMP-2 was expected to result in an improved bone healing outcome. Pure MBG dissolution products showed excellent cytocompatibility on primary hMSCs (Figure 16A, B) and increased matrix mineralization (Figure 16C) [14].

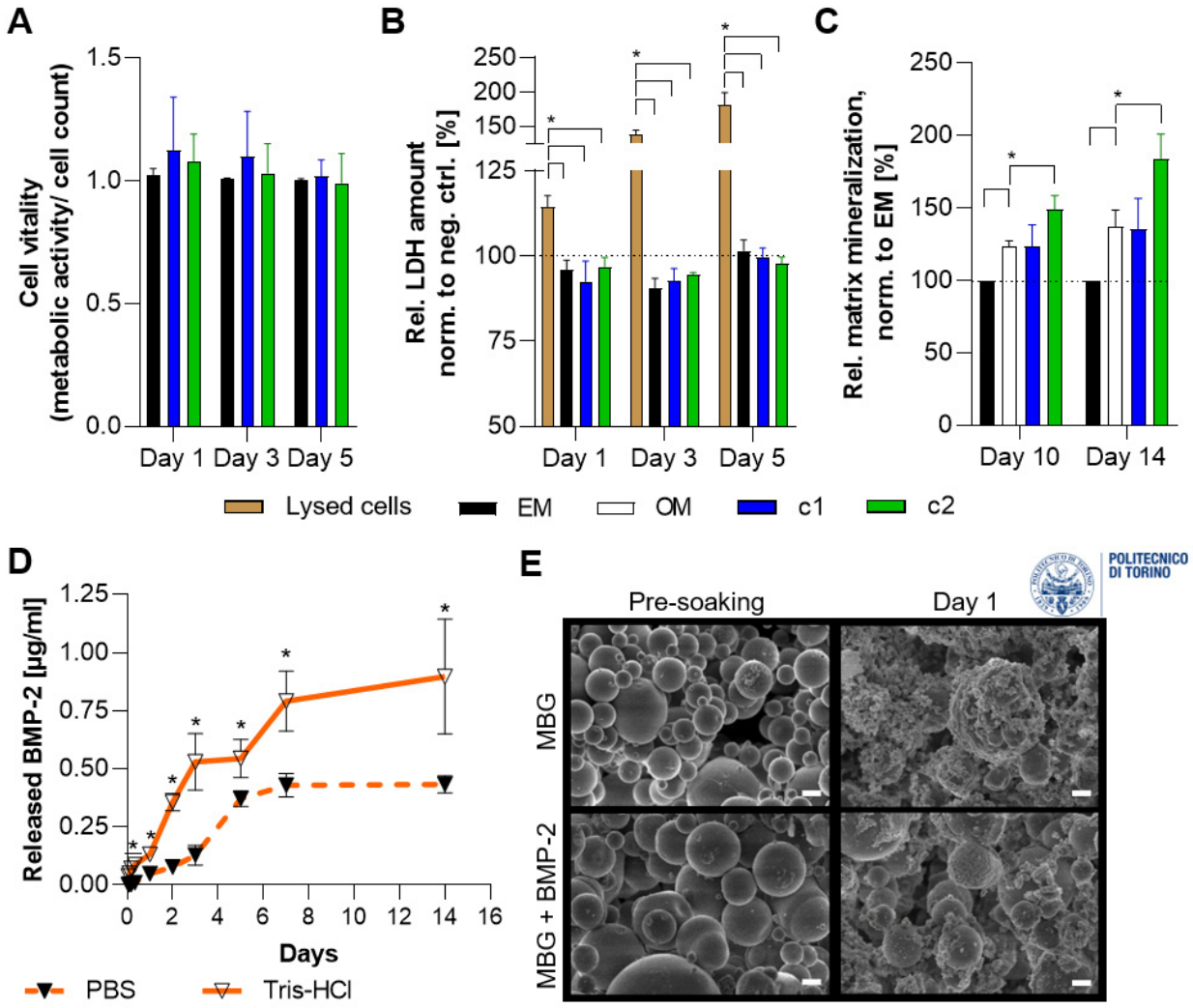


**Figure 16. hMSC response to pure MBG ionic dissolution products, BMP-2 release and MBG characterization.** **(A)** Cell vitality index (metabolic activity over cell count), indicating the viability per cell, compared to EM. **(B)** LDH secretion into supernatant to test for cytotoxicity of the MBG treatment. Cells cultured in EM were lysed at each testing time point and were used as positive control to estimate the maximal amount of LDH. **(C)** Increased matrix mineralization by MBG treatment at higher concentrations (c2) as demonstrated by Alizarin Red S staining and normalization to cell count. (**A-C**) c1= 1.5 mg/ml, c2= 5 mg/ml MBG; n= 3 hMSC from different donors, ≥ 3 technical replicates per donor, one-way ANOVA with Dunnett's multiple comparison test. **(D)** Cumulative release of BMP-2

from MBG in phosphate-free Tris-HCl and phosphate-containing PBS, adjusted to the *in vivo* dosage. n= 3, ELISA performed in duplicate, shown are mean ± SD, two-tailed student's t-test was performed per time point. **(E)** Courtesy of POLITO: MBG morphology (pre-soaking) and bioactivity testing (day 1) by soaking in simulated body fluid (SFB) and performing field emission scanning electron microscopy (FE-SEM, scale bar= 1 µm). A similar bioactivity for un-/ loaded MBGs was evidenced by hydroxyapatite-like layer formation on the MBG surface with the typical cauliflower structure. * $p<0.05$; submitted manuscript, preprint available [14].

By performing an α-BMP-2 ELISA I found prolonged, low-dose BMP-2 release from MBG which was dependent on the presence of phosphate in the elution medium (Figure 16D). Phosphate is contained in simulated body fluid (SBF) and is required for the formation of a hydroxyapatite-like layer on the MBG surface which represents a measure for the bioactivity of bioactive glasses immersed in biological fluids [23]. Bioactivity remained unaltered by BMP-2 loading, as demonstrated by field emission scanning electron microscopy (FE-SEM) analysis, carried out by POLITO (Figure 16E).

The bone healing study conducted within my PhD thesis demonstrated successful *in vivo* BMP-2 release from MBG [14], embedded in a previously tested autologous blood clot [35]. BMP-2 activity was detected upon µCT-analysis (Figure 17A), showing higher BV and TV (examples of reconstructed µCT-images: Figure 17B) and an increased mineral content within the callus (bone mineral content (BMC)). Histomorphometry on MOVAT's pentachrome stained sections of the osteotomized femora (Figure 17C, D) confirmed the increased relative area of mineralization and revealed decreased connective tissue abundance for the BMP-2 group. Taking the results together, low-dose prolonged BMP-2 release results in a superior healing outcome. The beneficial release kinetics without burst compared to the clinically utilized absorbable collagen sponge with up to 50% burst release within the first day [36] make MBG a promising alternative carrier for BMP-2 that reduces the risk of side effects due to low amounts of dissolved BMP-2 released over time.

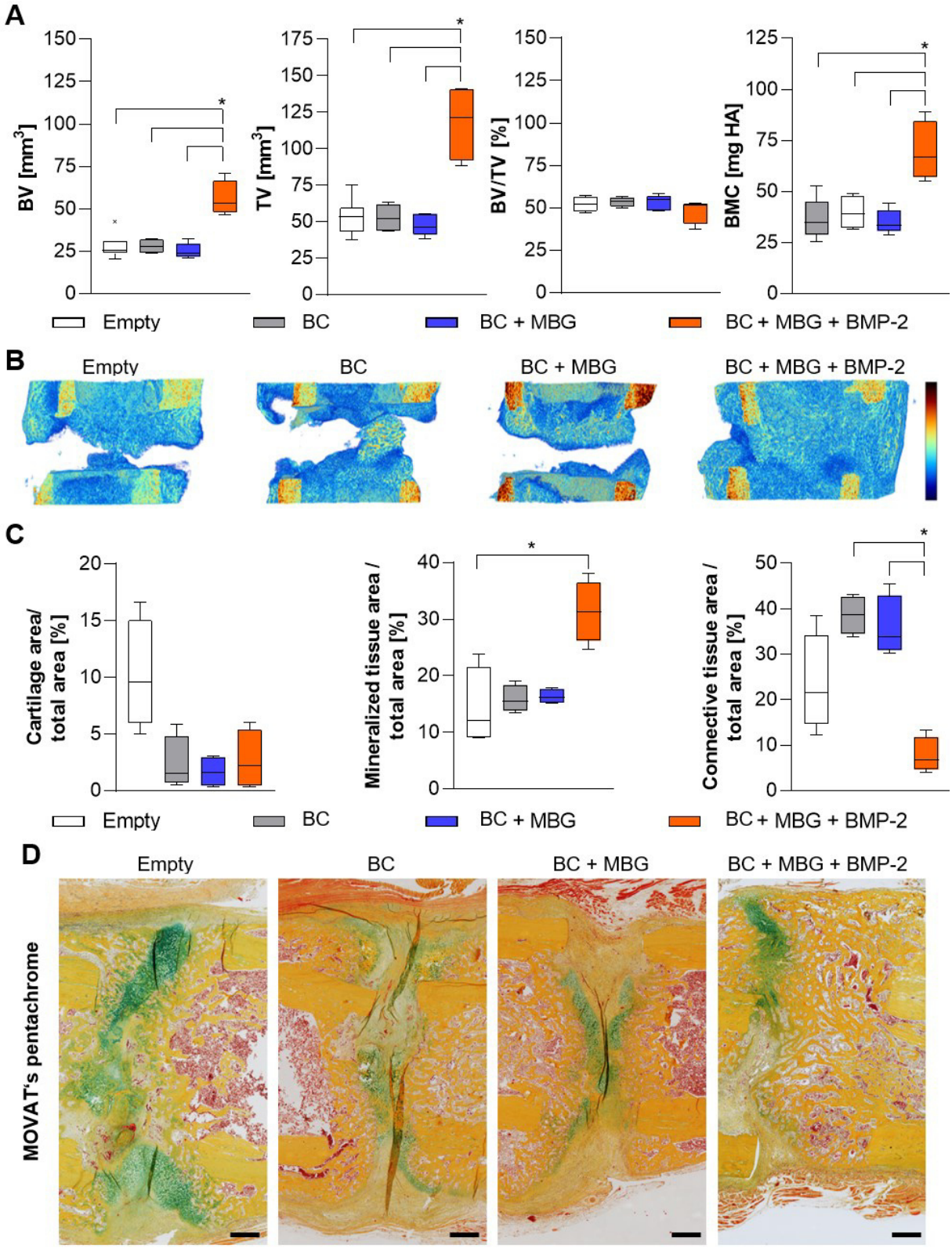


**Figure 17. *In vivo* bone healing upon low-dose, prolonged BMP-2 release from MBG. (A)** *Ex vivo* µCT analysis 4 weeks post osteotomy (empty: no local treatment) and local treatment with autologous blood clot (BC) without/ with MBG and BMP-2 load showing significantly enhanced BV and TV and bone mineral content (BMC) for the BMP-2 treated group. n= 4-6 per group, Tukey box plot distributions with line at median are shown, two-tailed Mann-Whitney U test was performed using BMP-2 as comparator. **(B)** Representative, reconstructed *ex vivo* µCT images; **(C)**

Histomorphometry to quantify relative cartilage, mineralized and connective tissue area based on the MOVAT's pentachrome staining, n=4 per group, two-tailed Mann-Whitney U test was performed using BMP-2 as comparator. (**D)** Representative images of MOVAT's pentachrome stained osteotomy areas (yellow/orange: mineralized tissue, green/blue: cartilaginous tissue, orange/ red: muscle tissue), scale bar= 500 μm. * $p<0.05$. Submitted manuscript, preprint available [14].

### 3.3. Clinical evaluation of technology platform confirming translation potential

Within my PhD project, I presented the BHD along with the standard operating protocol (SOP) on its preparation to nine expert orthopedic clinicians of the CMSC in the packaged version that could be used for commercialization. Both the SOP as well as the packaging were developed by MOZART collaboration partners. The clinicians were asked to prepare the BHD according to the SOP and to evaluate the BHD in respect to preparation, handling, overall need and possible applications by answering a customized questionnaire that I developed. Analysis of the questionnaire revealed that participants found the BHD easy to prepare and to apply, however, the time-to-usage (~30 min) was considered too long (Figure 18A). BHD preparation can be performed within the operating room (OR), if a cooling and shaking device is provided, however this is not standard OR equipment. All clinicians expressed a clinical need for the BHD and would use it if commercially available (Figure 18B). The possible applications are broad (Figure 18C), at the same time they call for the ability to fine tune the BHD as the required gelation time, gel stiffness and volumes vary according to the underlying pathology. Additionally, the concept of providing different BHDs with pro-angiogenic, pro-osteogenic, anti-inflammatory or anti-microbial features was well received. This clinical evaluation confirmed the need for novel treatment strategies and verified a possible translation of the MOZART approach.

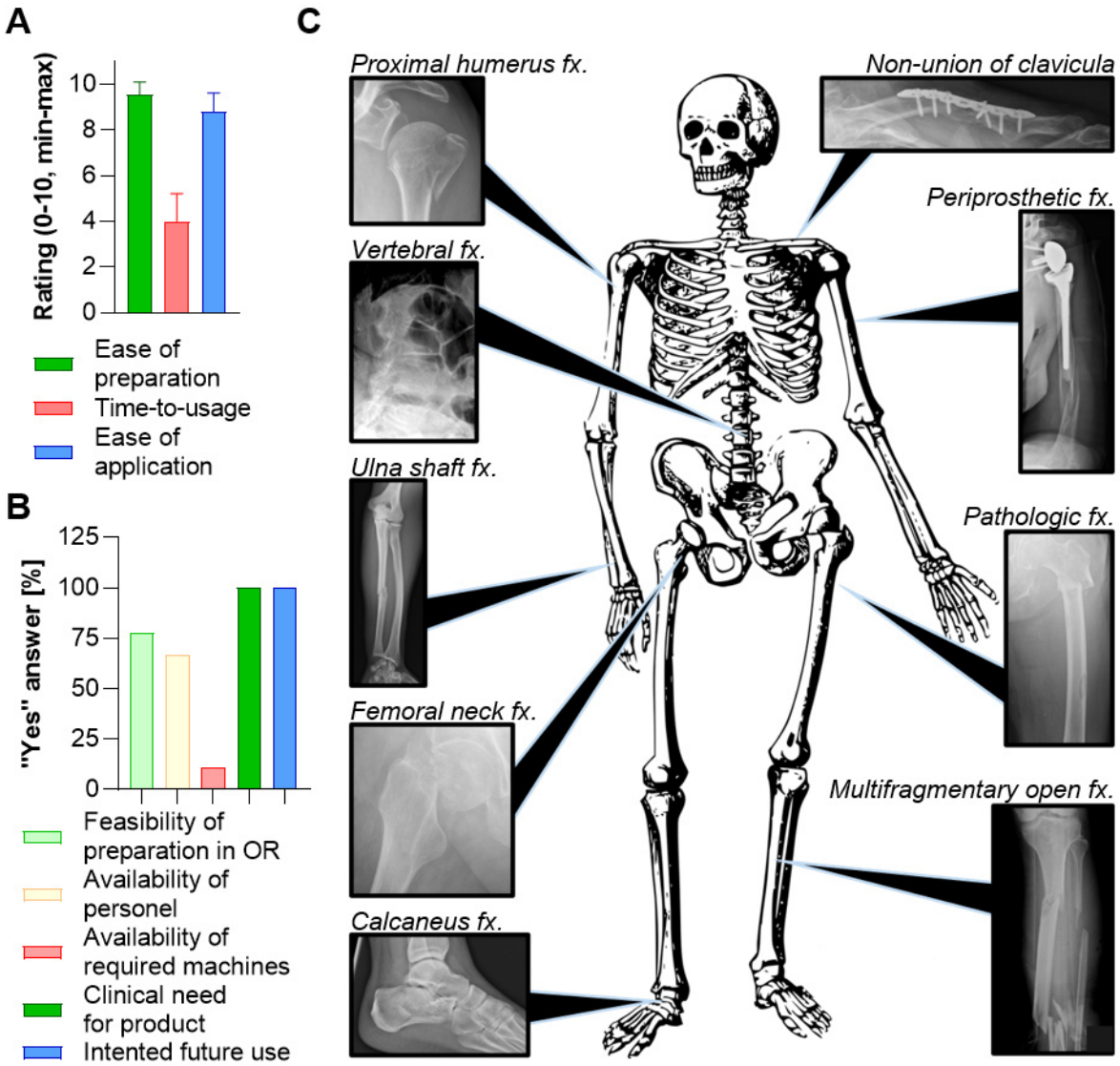


**Figure 18. Clinical evaluation of the BHD. (A, B)** Nine expert orthopedic clinicians of the CMSC, Charité – Universitätsmedizin Berlin assessed **(A)** preparation, time-to-usage, and application (on a scale of 1 (poorest) – 10 (best), shown are mean ± SD) **(B)** overall feasibility of BHD usage in the operating room (OR) as well as the clinical need and potential future use (relative amount of "Yes" answers in %), mean ± SD are shown. **(C)** Presenting the versatility of this technology platform to clinical colleagues enabled the identification of multiple applications for the BHD as indicated by representative x-ray images (courtesy of Dr. Gabriele Rußow, Charité – Universitätsmedizin Berlin) and fracture specification. Fx: fracture; unpublished data.

# 4. Discussion

### Bone healing and pharmacological interventions

Bone healing is initiated by pro-inflammatory signaling that is followed by anti-inflammatory and pro-angiogenic signaling; subsequently, pro-osteogenic processes can occur [1]. As regenerative impairments can occur at any stage of the bone healing process, different pharmacological interventions based on the individual needs are advisable (Figure 3.). When the BHD is administered as an add-on treatment for patients at risk during the first surgical intervention, this strategy could prevent the various disturbances of the healing process and could reduce the number of impaired healing cases. Functional treatment versatility requires proper patient stratification as can be achieved by measuring the patient-specific abundance of terminally differentiated effector T cells that are known to affect the healing outcome [37] (ongoing BioBone study, BMBF, headed by Charité) and considers various other patient- and injury-dependent factors. Aside from clinical studies at the Charité focusing on local immunomodulatory pharmacologic interventions (Prostacyclin, DFG, applied for) or pro-angiogenic autologous cell transplantation (CD31+ cells, BMBF, approved) in stratified patients, personalized treatment approaches are currently not available in the clinics. Moreover, to enable exchangeability or the combination of different functions, a carrier platform is needed. Effective interventions such as the usage of iliac crest autologous bone graft or administration of the osteogenic inducer BMP-2 necessitate an additional surgery or can entail considerable side effects and are, therefore, limited to selected fracture cases. The MOZART intervention strategy allows for multifunctionality or for the synergistic enhancement of effects in one target area (e.g. osteogenesis) by the combination of drug-loading and ion-doping of the MBG within the technology platform/ BHD. The injectability of the BHD makes it a minimally-invasive treatment, while the local application and consecutive dissolution of the glass network as well as diffusion of drugs out of the mesopores can result in prolonged release kinetics of ions and drugs that can be further delayed by penetration through the hydrogel [38]. At present, there is no commercial biomedical device that employs customized nano- to micron-sized mesoporous carriers that are embedded in a biodegradable polymer for local synergistic ion and drug release. Many scientific endeavors remain at lab-stage and -scale, i.e. they have not been designed for simple up-scaling and commercialization and lack proper validation in a clinically relevant setting. Industrial up-scaling has already been achieved by industrial partners for the here described technology platform, thereby facilitating future commercialization.

**Development of technology platform - Validation and customization of biomaterial components and encountered challenges**

Within my PhD project, the individual MOZART biomaterial components (carrier, SIP coating, thermosensitive hydrogel SHP407) have been biologically evaluated with respect to their suitability to be employed in the context of bone healing and for their cyto-/ and biocompatibility. Additionally, I selected ion and drug candidates and their combinations for functional customization of a modular BHD to address pro-angiogenic, pro-osteogenic, anti-inflammatory and anti-microbial therapeutic approaches. For this, I conducted numerous sub-projects in order to conclude the composition of the hybrid biomaterial to enhance bone healing. I had to coordinate these projects with the respective biomaterial partner, developed SOPs on biomaterial handling, and realized a subsequent pre-clinical *in vivo* application. I tested all the biomaterial components for the first time *in vivo* (individually or as composite) which is a key requirement for potential translation. The effect on bone regeneration of the final composites/ BHDs (Figure 19A) was investigated in a clinically relevant model of compromised bone healing in rats.

The initially proposed SIP-coating of MBG to confer pH-responsiveness, while discontinued for the bone healing application, was developed towards an endogenous pH-triggered release system to prevent and combat infection related to bone healing. The pH-sensitivity of the SIP to pH $\leq 5$ was out of range for bone healing applications in which a local mean pH of ~6.69 ± 0.26 within the first 48 hours post osteotomy was measured. Additionally, the SIP grafting on the MBG surface was not successful as the mesopores were too large (average diameter ~5– 7 nm) to be effectively closed by the SIP polymer. C1Sph emerged as an alternative MOZART carrier for which SIP-coating was successful. This enabled me to perform the *in vivo* validation of C1Sph-SIP behavior and responsiveness as well as further studies on pH-sensitive antimicrobial particles. The responsiveness of C1Sph-SIP loaded with antimicrobial agents to *S. aureus*-induced acidification is currently being investigated by collaboration partners and me.

Several combinations of ions and drugs were tested as part of different BHDs in the compromised bone healing study; however, the optimal concentrations are yet to be determined in future studies. Loading efficiencies are drug- and carrier-dependent, which can limit the uptake for e.g. large drug molecules. Additionally, the therapeutic ions and drugs were tested in combination, but not individually, for that reason, it is challenging to differentiate between individual and synergistic effects. Given the early pre-clinical stage without prior knowledge on the overall feasibility of this novel treatment approach, it was not considered reasonable to drastically increase animal numbers by performing individual and combinatorial testing. Nevertheless, I was able to successfully demonstrate the potential of the

treatment concept through confirming the reported pro-regenerative effects of the selected ions and drugs [29, 32, 34, 38] alone or upon release from the BHD. Ion and drug release from, as well as other effects evoked by MBG are highly dependent on the carrier composition, morphology, size, presentation mode and concentration [16, 24]. Keeping the MBG characteristics constant, the optimal concentrations and volumes of the individual components within the technology platform should be identified in further studies. As the industrial production routes were developed separately for the individual device components, and loading and doping remained customizable, the results of such studies could be implemented straightforwardly.

**Pre-clinical testing: the choice of animal models**

For early pre-clinical studies, rodent models are preferred due to the broad range of available downstream analysis. In line with the 3R principles, I employed animals that had to be sacrificed for reasons beyond the current research if possible (e.g. cadaver studies). The rat animal model of biologically impaired healing was developed and evaluated in house [33]. The aged rat resembles the average fracture case much closer than e.g. critical-sized defects in young animals, since the intrinsic healing capacity is reduced in the elderly patient as well as in the aged rat. The selected study end point at 4 weeks post osteotomy allows detection of beneficial effects on the bone healing outcome by different treatments, since bone healing has progressed to the mineralization phase, but is not completed in the untreated control. Moreover, application of the composite in the osteotomy gap required a large-enough void that could be created in the rat model.

**Translatable aspects of the individual and combined components of the technology platform**

<u>pH and bone healing – local acidification could be harnessed for pH-responsive drug release</u>

For the purpose of bone healing, I defined target values for pH sensitivity of biomaterials around pH 6.7 while detecting inter-individual differences that could be assigned to differences in metabolic activity in the TCA cycle [21]. Whether the different degrees of initial acidification cause variations in the bone healing outcome was beyond the scope of this study; answering this question will be essential to unravel the biological role of this local acidification. In an earlier pre-clinical study by Newmann *et al.*, it was found that the group with delayed bone healing also presented with a prolonged acidification phase [39], indicating a link between local pH alterations/ kinetics and bone healing outcome. Since local pH acidifies as a result of decreased oxygen availability and metabolite accumulation after blood vessel rupture upon injury [11, 12, 39], blood vessel formation seems to be a pre-requisite for pH recovery to physiological or alkaline levels. In the elderly, the angiogenic potential is reduced, thus, it is likely that the acidic phase is prolonged in these patients, thereby preventing

proper mineral deposition which occurs in the subsequent alkaline phase [11]. Further studies could test whether dampening/ shortening of the acidification phase could accelerate bone healing.

As mentioned above, the SIP coating is sensitive to more pronounced pH changes than found in the fracture setting. However, biomaterials that react to more subtle changes have been developed [40]. Adding such pH-sensitivity to the BHD would allow an even more targeted treatment approach and drug release with a lag time as acidification does not occur immediately after fracture (Figure 19B). This is especially relevant for immunomodulatory interventions, since initial pro-inflammatory signaling is required for proper bone healing.

pH and infection – infections qualify for pH-triggered drug release

External pH can be modified by bacterial metabolism, both *in vitro* as well as *in vivo* in the human patient as I demonstrated by measuring the pH in synovial fluids. Here, I found that *S. aureus* infections significantly reduce the local pH to a mean pH of 6.35 ± 0.63. Employing MOZART local treatment strategies with additional adequate pH responsiveness could allow for an anti-microbial therapy on endogenous demand with the infection causing the response of the drug release system (Figure 19C). In collaboration with MOZART partners, I am currently developing and testing this treatment strategy *in vitro*. Such an approach could reduce the risk for development of bacterial resistance, as the drug is only released if a threshold pH is reached, that can be created by the infection. The combination of anti-microbial ions like silver, copper and cerium with an antibiotic could exert synergistic effects and further counteract resistances as the bacteria could be killed more effectively. This question is currently being pursued by me and MOZART collaboration partners in another ongoing study.

Broad applications of the bone healing device

Within this PhD project, I tested the effect of different combinations of ions and drugs and identified N-Acetylcysteine as a pro-angiogenic and pro-osteogenic drug that can be administered locally and combined with therapeutic ions like Strontium and Copper. Pre-clinically, both ions were found to exert their expected osteoclast-inhibiting [29] and pro-angiogenic effects [34, 38], respectively, confirming the successful drug and ion release. MBG emerged as a suitable carrier for BMP-2 (submitted manuscript), exhibiting superior release kinetics with a prolonged, low-dose BMP-2 release (Figure 19D) when compared to the high burst release of the clinically used collagen sponge [13, 36]. This collagen sponge was recently described as a material that drastically impairs bone healing [20], whereas I could show that MBG did not affect healing when embedded in a blood clot. This strategy is easily translatable, since the MBG production route is cost-effective and upscaling has already been accomplished. Furthermore, the blood clot as an embedding moiety for the MBG can be created within the operating room. Both, the complete BHD, as well as BMP-2 loaded MBG open up numerous potential applications which I together with orthopedic experts have identified (Figure 19E).

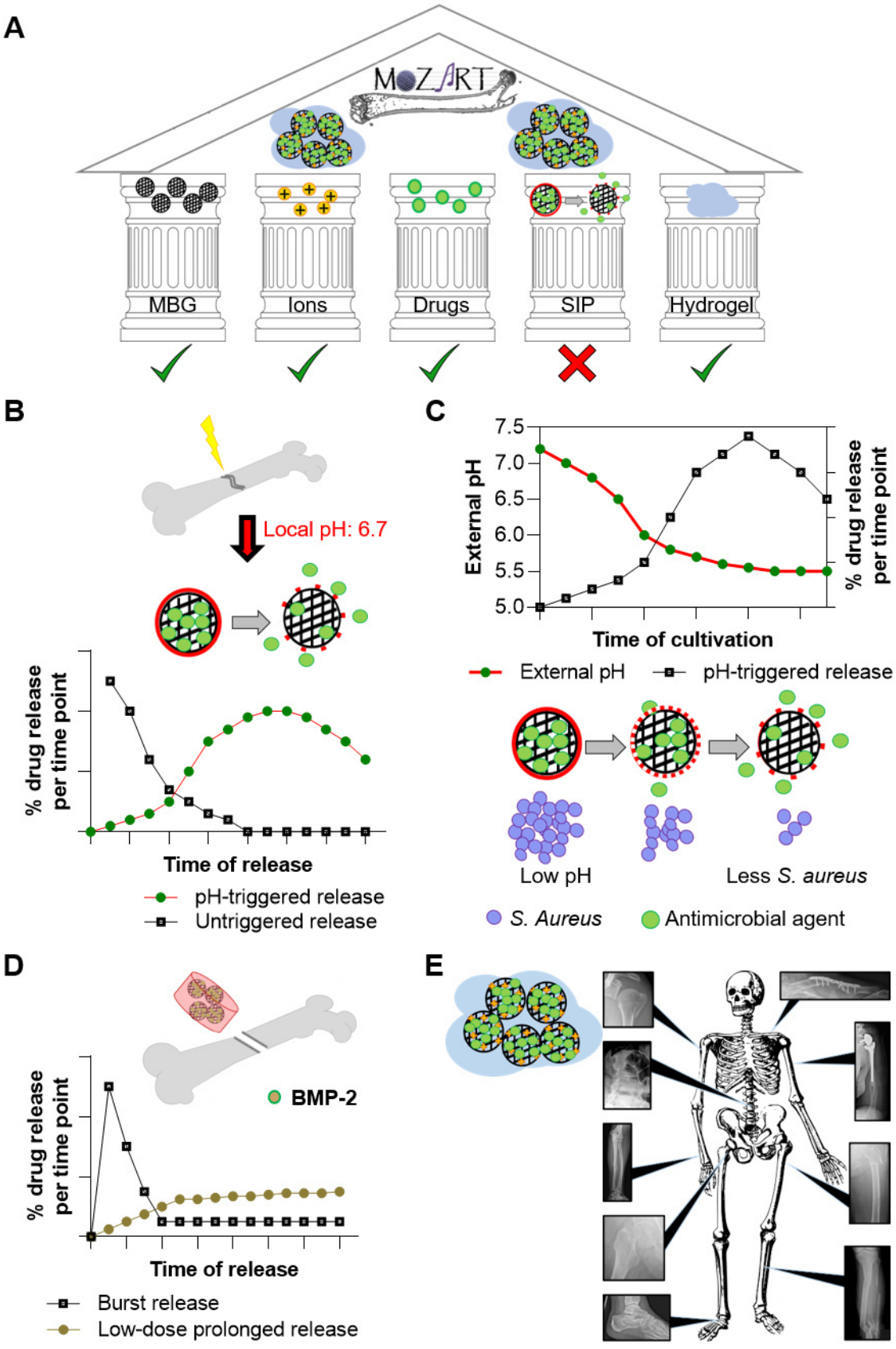


**Figure 19. Translatable aspects of this PhD project. (A)** The combination of different biomaterial components (excluding the pH-responsive SIP coating), therapeutic ions, and drugs make up the MOZART BHD that was tested in the context of bone healing in a pre-clinical animal model. **(B)** Biomaterials responsive to subtle pH changes (pH

~6.7) can be used for triggered, highly localized drug release with a lag time in fracture settings. **(C)** Metabolic activity of bacteria such as *S. aureus* can acidify their environment. pH-sensitive drug release systems can respond to this pH change by the release of antimicrobial agents. **(D)** MBG as carrier for BMP-2 yield a low-dose, prolonged release, greatly discriminating this carrier from the clinically used collagen sponge with high burst**. (E)** Identification of numerous orthopedic applications of the BHD.

A particular strength of the MOZART approach is the versatility and adjustability and, therefore its multi-functionality with respect to elicited responses and clinical specifications. Each component can be exchanged for another. Different therapeutic ions and drug combinations can be selected, embedding materials can be altered in terms of sol-gel properties and stiffness of the thermosensitive hydrogel, and stimuli-sensitivity can be added to the product. This modularity is desirable to achieve broad usage and applications. It further allows treatment personalization that is of utmost relevance to achieve the optimal clinical outcome. The medical need for such versatile interventions was assessed by Cellogic (Figure 3) and all orthopedic clinicians consulted about the BHD confirmed their desire to use such a product in the future (Figure 18).

**Conclusion/ Outlook**

Within my PhD project, I biologically evaluated the MOZART BHD components individually and in combination *in vitro* and in pre-clinical *in vivo* settings as the first step towards clinical translation. I engaged in a constant exchange with our biomaterial partners and defined therapeutic ion and drug candidates in order to exploit the full potential of the biomaterial components in a biologically appropriate manner. This approach included multiple iterations and adjustments based on physiological and application-specific boundary conditions that were uncovered during my PhD work. The developed technology platform can be employed as bone healing device, but can furthermore be utilized to combat infections. For the BHD, I identified therapeutic ions and drugs candidates, both based on extensive literature search and *in vitro* studies, as well as identified the target concentration of NAC by an *in vivo* proof-of-concept study. I confirmed successful drug release from the carrier platform by detecting the fluorophore and calcium-binding Tetracycline intercalated in newly deposited bone. Although not statistically significant, the combination of NAC with Sr or Cu indicate the desired individual effects on bone microarchitecture, osteoclast-inhibition and angiogenesis, respectively. While numerous potential applications for the BHD have been identified by me in close collaboration with clinicians, individual components and findings can likewise prove suitable for future translation. Prolonged low-dose BMP-2 release from MBG could reduce the risk of side effects as only a low dose of BMP-2 at any one time is dissolved and biologically active. Local pH changes after fracture could be exploited for pH-triggered drug release by combining MOZART carriers with highly sensitive pH-responsive materials. As pH acidification does not occur immediately after fracture [21], such a drug release system could release its cargo with a lag time which is relevant for

immunomodulatory interventions. Future studies should investigate whether the initial acidification exerts an essential function or if bone healing in general could be accelerated by dampening/ shortening the acidification phase. Lastly, selective antimicrobial treatments triggered by metabolic activity and proliferation of bacteria could be used as future add-on treatments in open fracture cases or prosthetic surgeries and could help to prevent osteomyelitis or replacement surgeries due to sepsis. Novel treatment approaches that are validated in a clinically relevant setting and can be commercially up-scaled based on developed and realized industrial production routes such as the ones presented in this thesis are urgently needed to counteract impaired healing and orthopedic infections.

# 5. References


1. Schmidt-Bleek K, Petersen A, Dienelt A, Schwarz C, Duda GN. Initiation and early control of tissue regeneration - bone healing as a model system for tissue regeneration. Expert opinion on biological therapy. 2014;14(2):247-59.
2. Marsell R, Einhorn TA. The biology of fracture healing. Injury. 2011;42(6):551-5.
3. Wu X, Li Z, Cao J, Jiao J, Wang Y, Liu G, Liu Y, Li F, Song B, Jin J, Liu Y, Wen X, Cheng S, Wan X. The association between major complications of immobility during hospitalization and quality of life among bedridden patients: A 3 month prospective multi-center study. PLoS One. 2018;13(10):e0205729.
4. Zeckey C, Mommsen P, Andruszkow H, Macke C, Frink M, Stubig T, Hufner T, Krettek C, Hildebrand F. The aseptic femoral and tibial shaft non-union in healthy patients - an analysis of the health-related quality of life and the socioeconomic outcome. Open Orthop J. 2011;5:193-7.
5. Clark D, Nakamura M, Miclau T, Marcucio R. Effects of Aging on Fracture Healing. Curr Osteoporos Rep. 2017;15(6):601-8.
6. Gruber R, Koch H, Doll BA, Tegtmeier F, Einhorn TA, Hollinger JO. Fracture healing in the elderly patient. Exp Gerontol. 2006;41(11):1080-93.
7. Franceschi C, Bonafe M, Valensin S, Olivieri F, De Luca M, Ottaviani E, De Benedictis G. Inflamm-aging. An evolutionary perspective on immunosenescence. Ann N Y Acad Sci. 2000;908:244-54.
8. World Health Organization (WHO). Ageing and health. 2018. Available online: https://www.who.int/news-room/fact-sheets/detail/ageing-and-health. (last accessed on 2 July 2020).
9. Hadji P, Klein S, Gothe H, Haussler B, Kless T, Schmidt T, Steinle T, Verheyen F, Linder R. The epidemiology of osteoporosis--Bone Evaluation Study (BEST): an analysis of routine health insurance data. Dtsch Arztebl Int. 2013;110(4):52-7.
10. Hak DJ, Fitzpatrick D, Bishop JA, Marsh JL, Tilp S, Schnettler R, Simpson H, Alt V. Delayed union and nonunions: epidemiology, clinical issues, and financial aspects. Injury. 2014;45 Suppl 2:S3-7.
11. Chakkalakal DA, Mashoof AA, Novak J, Strates BS, McGuire MH. Mineralization and pH relationships in healing skeletal defects grafted with demineralized bone matrix. J Biomed Mater Res. 1994;28(12):1439-43.
12. Newman RJ, Duthie RB, Francis MJ. Nuclear magnetic resonance studies of fracture repair. Clin Orthop Relat Res. 1985(198):297-303.
13. Schmidt-Bleek K, Willie BM, Schwabe P, Seemann P, Duda GN. BMPs in bone regeneration: Less is more effective, a paradigm-shift. Cytokine Growth Factor Rev. 2016;27:141-8.
14. Berkmann JC, Herrera Martin AX, Pontremoli C, Zheng K, Bucher CH, Ellinghaus A, Boccaccini AR, Fiorilli S, Vitale-Brovarone C, Duda GN, Schmidt-Bleek K. In vivo validation of spray-dried mesoporous bioactive glass microspheres acting as prolonged local release systems for BMP-2 to induce bone regeneration. bioRxiv. 2020:2020.03.21.001404.
15. Gisbert-Garzaran M, Berkmann JC, Giasafaki D, Lozano D, Spyrou K, Manzano M, Steriotis T, Duda GN, Schmidt-Bleek K, Charalambopoulou G, Vallet-Regi M. Engineered pH-Responsive Mesoporous Carbon Nanoparticles for Drug Delivery. ACS Appl Mater Interfaces. 2020.
16. Qazi TH, Berkmann JC, Schoon J, Geissler S, Duda GN, Boccaccini AR, Lippens E. Dosage and composition of bioactive glasses differentially regulate angiogenic and osteogenic response of human MSCs. J Biomed Mater Res A. 2018;106(11):2827-37.
17. Boffito M, Torchio A, Tonda-Turo C, Laurano R, Gisbert-Garzarán M, Berkmann JC, Cassino C, Manzano M, Duda GN, Vallet-Regí M, Schmidt-Bleek K, Ciardelli G. Hybrid Injectable Sol-Gel Systems Based on Thermo-Sensitive Polyurethane Hydrogels Carrying pH-Sensitive

Mesoporous Silica Nanoparticles for the Controlled and Triggered Release of Therapeutic Agents. Frontiers in Bioengineering and Biotechnology. 2020;8.
18. Schindelin J, Arganda-Carreras I, Frise E, Kaynig V, Longair M, Pietzsch T, Preibisch S, Rueden C, Saalfeld S, Schmid B, Tinevez JY, White DJ, Hartenstein V, Eliceiri K, Tomancak P, Cardona A. Fiji: an open-source platform for biological-image analysis. Nat Methods. 2012;9(7):676-82.
19. Wendler S, Schlundt C, Bucher CH, Birkigt J, Schipp CJ, Volk HD, Duda GN, Schmidt-Bleek K. Immune Modulation to Enhance Bone Healing-A New Concept to Induce Bone Using Prostacyclin to Locally Modulate Immunity. Front Immunol. 2019;10:713.
20. Lang A, Kirchner M, Stefanowski J, Durst M, Weber MC, Pfeiffenberger M, Damerau A, Hauser AE, Hoff P, Duda GN, Buttgereit F, Schmidt-Bleek K, Gaber T. Collagen I-based scaffolds negatively impact fracture healing in a mouse-osteotomy-model although used routinely in research and clinical application. Acta Biomater. 2019;86:171-84.
21. Berkmann JC, Herrera Martin AX, Ellinghaus A, Schlundt C, Schell H, Lippens E, Duda GN, Tsitsilonis S, Schmidt-Bleek K. Early pH Changes in Musculoskeletal Tissues upon Injury-Aerobic Catabolic Pathway Activity Linked to Inter-Individual Differences in Local pH. Int J Mol Sci. 2020;21(7).
22. Hench LL. The story of Bioglass. J Mater Sci Mater Med. 2006;17(11):967-78.
23. Hoppe A, Guldal NS, Boccaccini AR. A review of the biological response to ionic dissolution products from bioactive glasses and glass-ceramics. Biomaterials. 2011;32(11):2757-74.
24. Qazi TH, Hafeez S, Schmidt J, Duda GN, Boccaccini AR, Lippens E. Comparison of the effects of 45S5 and 1393 bioactive glass microparticles on hMSC behavior. J Biomed Mater Res A. 2017;105(10):2772-82.
25. Sui B, Zhong G, Sun J. Drug-loadable Mesoporous Bioactive Glass Nanospheres: Biodistribution, Clearance, BRL Cellular Location and Systemic Risk Assessment via (45)Ca Labelling and Histological Analysis. Sci Rep. 2016;6:33443.
26. Hamann FM, Brehm R, Pauli J, Grabolle M, Frank W, Kaiser WA, Fischer D, Resch-Genger U, Hilger I. Controlled modulation of serum protein binding and biodistribution of asymmetric cyanine dyes by variation of the number of sulfonate groups. Mol Imaging. 2011;10(4):258-69.
27. Schmidt-Bleek K, Schell H, Lienau J, Schulz N, Hoff P, Pfaff M, Schmidt G, Martin C, Perka C, Buttgereit F, Volk HD, Duda G. Initial immune reaction and angiogenesis in bone healing. J Tissue Eng Regen Med. 2014;8(2):120-30.
28. Gisbert-Garzaran M, Lozano D, Vallet-Regí M, Manzano M. Self-immolative polymers as novel pH-responsive gate keepers for drug delivery. RSC Advances. 2017;7(1):132-6.
29. Peng S, Liu XS, Huang S, Li Z, Pan H, Zhen W, Luk KD, Guo XE, Lu WW. The cross-talk between osteoclasts and osteoblasts in response to strontium treatment: involvement of osteoprotegerin. Bone. 2011;49(6):1290-8.
30. Zhang W, Zhao F, Huang D, Fu X, Li X, Chen X. Strontium-Substituted Submicrometer Bioactive Glasses Modulate Macrophage Responses for Improved Bone Regeneration. ACS Appl Mater Interfaces. 2016;8(45):30747-58.
31. Zafarullah M, Li WQ, Sylvester J, Ahmad M. Molecular mechanisms of N-acetylcysteine actions. Cell Mol Life Sci. 2003;60(1):6-20.
32. Geissler S, Textor M, Schmidt-Bleek K, Klein O, Thiele M, Ellinghaus A, Jacobi D, Ode A, Perka C, Dienelt A, Klose J, Kasper G, Duda GN, Strube P. In serum veritas-in serum sanitas? Cell non-autonomous aging compromises differentiation and survival of mesenchymal stromal cells via the oxidative stress pathway. Cell Death Dis. 2013;4:e970.
33. Preininger B, Gerigk H, Bruckner J, Perka C, Schell H, Ellinghaus A, Schmidt-Bleek K, Duda G. An experimental setup to evaluate innovative therapy options for the enhancement of bone healing using BMP as a benchmark--a pilot study. Eur Cell Mater. 2012;23:262-71; discussion 71-2.

34. Xie H, Kang YJ. Role of copper in angiogenesis and its medicinal implications. Curr Med Chem. 2009;16(10):1304-14.
35. Winkler T, Sass FA, Duda GN, Schmidt-Bleek K. A review of biomaterials in bone defect healing, remaining shortcomings and future opportunities for bone tissue engineering: The unsolved challenge. Bone Joint Res. 2018;7(3):232-43.
36. Seeherman H, Wozney J, Li R. Bone morphogenetic protein delivery systems. Spine (Phila Pa 1976). 2002;27(16 Suppl 1):S16-23.
37. Reinke S, Geissler S, Taylor WR, Schmidt-Bleek K, Juelke K, Schwachmeyer V, Dahne M, Hartwig T, Akyuz L, Meisel C, Unterwalder N, Singh NB, Reinke P, Haas NP, Volk HD, Duda GN. Terminally differentiated CD8(+) T cells negatively affect bone regeneration in humans. Sci Transl Med. 2013;5(177):177ra36.
38. Pontremoli C, Boffito M, Fiorilli S, Laurano R, Torchio A, Bari A, Tonda-Turo C, Ciardelli G, Vitale-Brovarone C. Hybrid injectable platforms for the in situ delivery of therapeutic ions from mesoporous glasses. Chemical Engineering Journal. 2018;340:103-13.
39. Newman RJ, Francis MJ, Duthie RB. Nuclear magnetic resonance studies of experimentally induced delayed fracture union. Clin Orthop Relat Res. 1987(216):253-61.
40. Chu L, Gao H, Cheng T, Zhang Y, Liu J, Huang F, Yang C, Shi L, Liu J. A charge-adaptive nanosystem for prolonged and enhanced in vivo antibiotic delivery. Chem Commun (Camb). 2016;52(37):6265-8.

## 6. Eidesstattliche Versicherung

„Ich, Julia Catherine Berkmann, versichere an Eides statt durch meine eigenhändige Unterschrift, dass ich die vorgelegte Dissertation mit dem Thema:

„Biologische Evaluation und Anpassung einer neuartigen, modularen Technologieplattform für die lokale Freisetzung von Ionen und Medikamenten in der Knochenheilung“/

‘Biological evaluation and customization of a novel modular technology platform for local ion and drug delivery in bone healing’

selbstständig und ohne nicht offengelegte Hilfe Dritter verfasst und keine anderen als die angegebenen Quellen und Hilfsmittel genutzt habe.

Alle Stellen, die wörtlich oder dem Sinne nach auf Publikationen oder Vorträgen anderer Autoren/innen beruhen, sind als solche in korrekter Zitierung kenntlich gemacht. Die Abschnitte zu Methodik (insbesondere praktische Arbeiten, Laborbestimmungen, statistische Aufarbeitung) und Resultaten (insbesondere Abbildungen, Graphiken und Tabellen) werden von mir verantwortet.

Ich versichere ferner, dass ich die in Zusammenarbeit mit anderen Personen generierten Daten, Datenauswertungen und Schlussfolgerungen korrekt gekennzeichnet und meinen eigenen Beitrag sowie die Beiträge anderer Personen korrekt kenntlich gemacht habe (siehe Anteilserklärung). Texte oder Textteile, die gemeinsam mit anderen erstellt oder verwendet wurden, habe ich korrekt kenntlich gemacht.

Meine Anteile an etwaigen Publikationen zu dieser Dissertation entsprechen denen, die in der untenstehenden gemeinsamen Erklärung mit dem/der Erstbetreuer/in, angegeben sind. Für sämtliche im Rahmen der Dissertation entstandenen Publikationen wurden die Richtlinien des ICMJE (International Committee of Medical Journal Editors; www.icmje.og) zur Autorenschaft eingehalten. Ich erkläre ferner, dass ich mich zur Einhaltung der Satzung der Charité – Universitätsmedizin Berlin zur Sicherung Guter Wissenschaftlicher Praxis verpflichte.

Weiterhin versichere ich, dass ich diese Dissertation weder in gleicher noch in ähnlicher Form bereits an einer anderen Fakultät eingereicht habe.

Die Bedeutung dieser eidesstattlichen Versicherung und die strafrechtlichen Folgen einer unwahren eidesstattlichen Versicherung (§§156, 161 des Strafgesetzbuches) sind mir bekannt und bewusst.“

Datum Unterschrift

## Anteilserklärung an den erfolgten Publikationen

Frau Julia Catherine Berkmann hatte folgenden Anteil an den folgenden Publikationen:

**Publikation 1:** Miguel Gisbert-Garzaran*, Julia C. Berkmann*, Dimitra Giasafaki, Daniel Lozano, Konstantinos Spyrou, Miguel Manzano, Theodore Steriotis, Georg N. Duda, Katharina Schmidt-Bleek,Georgia Charalambopoulou,and María Vallet-Regí. *Engineered pH-Responsive Mesoporous Carbon Nanoparticles for Drug Delivery*. ACS Applied materials and interfaces, 2020

* Equally contributing co-first authors

Beitrag im Einzelnen: Ko-Erstautorin

Aufbauend auf die Materialcharakterisierung und *in vial*/ *in vitro* Untersuchungen zu der pH-Reaktivität der mesoporigen Carbone mit pH-sensitiver SIP-Beschichtung habe ich eine Erweiterung des Manuskripts um eine *in vivo* Validierung der pH-Reaktivität des hybriden Biomaterials vorgenommen. Diese prä-klinische *in vivo* Validierung ebnet den Weg für eine künftige Translation und ermöglicht weitere klinisch-orientierte Erforschung von Anwendungsmöglichkeiten des hybriden Biomaterials.

Entsprechend habe ich das Studienkonzept und -protokoll des *in vivo* Versuchs entwickelt. Dies bedeutet im Einzelnen, dass ich ein SOP für die Materialpräparation für die *in vivo* Applikation erstellt habe, Vortestungen zur pH-Reaktivität nach 30-minütigem oder 24-stündigem pH-Stimulus zur Analyse der Anwendbarkeit des entwickelten hybriden, pH-sensitiven Biomaterials durchgeführt, an der Konzeption und Revision des Ethikantrags für den dazugehörigen Tierversuch mitgewirkt und den *in vivo* Versuch unter Aufsicht von Veterinärmedizinern durchgeführt habe. Hierzu zählen auch das longitudinale *in vivo* imaging, die Gewebeentnahme und -prozessierung, sowie die H&E-Färbung.

Mir oblag die hauptverantwortliche Datengewinnung und -analyse zu den Abbildungen 6, 7 und 8 der Veröffentlichung. Den Erstentwurf des Textanteils der *in vivo* Validierung und dazugehörigen Vortestungen (Abbildung 6, 7, 8) habe ich in allen Kapiteln der Veröffentlichung selbst erstellt. Die Veröffentlichung wurde von mir entsprechend meines Beitrags anhand von Reviewer-Kommentaren überarbeitet und kritisch interpretiert.

**Publikation 2:** Julia C. Berkmann, Aaron X. Herrera Martin, Agnes Ellinghaus, Claudia Schlundt,Hanna Schell, Evi Lippens, Georg N. Duda, Serafeim Tsitsilonis and Katharina Schmidt-Bleek. *Early pH Changes in Musculoskeletal Tissues upon Injury—Aerobic Catabolic Pathway Activity Linked to Inter-Individual Differences in Local pH*. International Journal of Molecular Sciences, 2020

Beitrag im Einzelnen: Erstautorin

Für diese Veröffentlichung oblag mir die Konzeption, Definition und Entwicklung der downstream Analysen im Anschluss an die Extraktion der Hämatome der Ratte. Bezüglich der Methodik habe ich pH-Messungen in Proben der Ratte vorgenommen, histologische Analysen übernommen, die Zelldichte in Schnitten des Hämatoms bestimmt und die metabolomische Analyse geplant, diskutiert und organisiert. Ich bin hauptverantwortlich für die Datengewinnung und -analyse für die Abbildungen 3, 4, 5 und Tabellen 1 und 2 sowie für die Visualisierung aller gezeigten Abbildungen und Tabellen. Ebenfalls habe ich das Manuskript konzipiert, den Erstentwurf geschrieben, das Manuskript entlang von Anmerkungen der Ko-Autoren überarbeitet und kritisch interpretiert. Ich habe das Manuskript selbstständig eingereicht und Anpassungen gemäß den Empfehlungen der Reviewer vorgenommen sowie eine ausführliche point-by-point Antwort auf die Einzelkommentare geschrieben.

**Publikation 3:** Monica Boffito, Alessandro Torchio, Chiara Tonda-Turo, Rossella Laurano, Miguel Gisbert-Garzarán, Julia C. Berkmann, Claudio Cassino, Miguel Manzano, Georg N. Duda, María Vallet-Regí, Katharina Schmidt-Bleek and Gianluca Ciardelli. *Hybrid Injectable Sol-Gel Systems Based on Thermo-Sensitive Polyurethane Hydrogels Carrying pH-Sensitive Mesoporous Silica Nanoparticles for the Controlled and Triggered Release of Therapeutic Agents*. Frontiers in Bioengineering and Biotechnology, 2020

Beitrag im Einzelnen: Ko-Autorin

Meine Arbeiten haben die Veröffentlichung um eine *in situ* Analyse der Applikation und Anwendbarkeit des thermosensitiven Hydrogels als „Platzhalter“ und des Biomaterialien-Komposits im murinen Kadaver mit physiologischer Körpertemperatur als Basis für spätere *in vivo* Applikationen ergänzt. Dafür habe ich das Studienkonzept/ -protokoll des *in situ* Versuches entwickelt, was die Erstellung eines SOP für die Präparation und Applikation mittels Injektion, die Aufrechterhaltung der physiologischen Körpertemperatur und die Definition der Analysemethoden (visuell und haptisch von gefärbtem und ungefärbtem Hydrogel, *in vivo* imaging für die Fragestellung der Transmission des Fluoreszenzsignals durch das Hydrogel und zur Analyse der Materialdistribution nach Injektion) beinhaltete. Ich habe unter Aufsicht von Veterinärmedizinern den *in situ* Versuch durchgeführt (Applikation des Materials, longitudinales *in vivo* imaging, Materialextraktion) und bin hauptverantwortlich für die Datengewinnung und -analyse zu den Abbildungen 4 und 7 der Veröffentlichung. Bzgl. des *in situ* Versuches (Abbildung 4 und 7) habe ich einen Erstentwurf in allen Kapiteln der Veröffentlichung erstellt und im Folgenden die Veröffentlichung überarbeitet und kritisch interpretiert.

_____

Unterschrift, Datum und Stempel des/der erstbetreuenden Hochschullehrers/in

_____

Unterschrift des Doktoranden/der Doktorandin

# 7. Publications

**Publication 1: 'Engineered pH-responsive mesoporous carbon nanoparticles for drug delivery'**

Miguel Gisbert-Garzarán[+], Julia C. Berkmann[+], Dimitra Giasafaki, Daniel Lozano, Konstantinos Spyrou, Miguel Manzano, Theodore Steriotis, Georg N. Duda, Katharina Schmidt-Bleek***,** Georgia Charalambopoulou*****, and María Vallet-Regí***,** *Engineered pH-responsive mesoporous carbon nanoparticles for drug delivery*, ACS Appl. Mater. Interfaces, 2020

https://doi.org/10.1021/acsami.0c01786

[+] shared first authors | * corresponding authors

Journal Data Filtered By: **Selected JCR Year: 2018** Selected Editions: SCIE,SSCI
Selected Categories: **"MATERIALS SCIENCE, MULTIDISCIPLINARY"**
Selected Category Scheme: WoS
**Gesamtanzahl: 293 Journale**

| Rank | Full Journal Title | Total Cites | Journal Impact Factor | Eigenfactor Score |
|---|---|---|---|---|
| 22 | CHEMISTRY OF MATERIALS | 106,568 | 10.159 | 0.150260 |
| 23 | npj Computational Materials | 954 | 9.200 | 0.003660 |
| 24 | Nanoscale Horizons | 888 | 9.095 | 0.002340 |
| 25 | Nano-Micro Letters | 2,209 | 9.043 | 0.003590 |
| 26 | Nano Research | 16,517 | 8.515 | 0.031810 |
| 27 | ACS Applied Materials & Interfaces | 170,096 | 8.456 | 0.366360 |

**Publication 2: 'Early pH changes in musculoskeletal tissues upon injury – Aerobic catabolic pathway activity linked to inter-individual differences in local pH'**

Julia C. Berkmann, Aaron X. Herrera Martin, Agnes Ellinghaus, Claudia Schlundt, Hanna Schell, Evi Lippens, Georg N. Duda, Serafeim Tsitsilonis*, Katharina Schmidt-Bleek*, *Early pH Changes in Musculoskeletal Tissues upon Injury-Aerobic Catabolic Pathway Activity Linked to Inter-Individual Differences in Local pH*, Int J Mol Sci. 2020

* corresponding authors

Journal Data Filtered By: **Selected JCR Year: 2018** Selected Editions: SCIE,SSCI Selected Categories: **"BIOCHEMISTRY and MOLECULAR BIOLOGY"** Selected Category Scheme: WoS
**Gesamtanzahl: 298 Journale**

| Rank | Full Journal Title | Total Cites | Journal Impact Factor | Eigenfactor Score |
|---|---|---|---|---|
| 65 | BIOELECTROCHEMISTRY | 4,476 | 4.474 | 0.004050 |
| 66 | BIOCHIMICA ET BIOPHYSICA ACTA-BIOENERGETICS | 12,823 | 4.441 | 0.017160 |
| 67 | EXPERT REVIEWS IN MOLECULAR MEDICINE | 1,758 | 4.407 | 0.001450 |
| 68 | BIOCHIMICA ET BIOPHYSICA ACTA-MOLECULAR AND CELL BIOLOGY OF LIPIDS | 9,688 | 4.402 | 0.018080 |
| 69 | BIOESSAYS | 9,911 | 4.396 | 0.016740 |
| 70 | ACS Chemical Biology | 11,691 | 4.374 | 0.036930 |
| 71 | BIOCONJUGATE CHEMISTRY | 15,840 | 4.349 | 0.020240 |
| 72 | AMERICAN JOURNAL OF RESPIRATORY CELL AND MOLECULAR BIOLOGY | 12,166 | 4.340 | 0.016110 |
| 73 | BIOCHEMICAL JOURNAL | 46,764 | 4.331 | 0.030420 |
| 74 | BIOCHIMICA ET BIOPHYSICA ACTA-MOLECULAR BASIS OF DISEASE | 14,373 | 4.328 | 0.024840 |
| 75 | BIOCHEMICAL SOCIETY TRANSACTIONS | 12,535 | 4.291 | 0.018720 |
| 76 | ADDICTION BIOLOGY | 4,055 | 4.223 | 0.008820 |
| 77 | GLYCOBIOLOGY | 7,752 | 4.194 | 0.008980 |
| 78 | INTERNATIONAL JOURNAL OF MOLECULAR SCIENCES | 53,148 | 4.183 | 0.114880 |

International Journal of
*Molecular Sciences*

MDPI

*Article*

# Early pH Changes in Musculoskeletal Tissues upon Injury—Aerobic Catabolic Pathway Activity Linked to Inter-Individual Differences in Local pH

**Julia C. Berkmann [1,2], Aaron X. Herrera Martin [1,2], Agnes Ellinghaus [3], Claudia Schlundt [1], Hanna Schell [1], Evi Lippens [1], Georg N. Duda [1,3], Serafeim Tsitsilonis [1,4,†] and Katharina Schmidt-Bleek [1,3,*,†]**

1 Julius Wolff Institut, Charité–Universitätsmedizin Berlin, 13353 Berlin, Germany; julia-catherine.berkmann@charite.de (J.C.B.); aaron.herrera@charite.de (A.X.H.M.); claudia.schlundt@charite.de (C.S.); hanna.schell@web.de (H.S.); evi.mm.lippens@gmail.com (E.L.); georg.duda@charite.de (G.N.D.); serafeim.tsitsilonis@charite.de (S.T.)
2 Berlin-Brandenburg School for Regenerative Therapies, Charité–Universitätsmedizin Berlin, 13353 Berlin, Germany
3 BIH Center for Regenerative Therapies, Charité–Universitätsmedizin Berlin, Berlin 10178, Germany; agnes.ellinghaus@charite.de
4 Center for Musculoskeletal Surgery, Charité–Universitätsmedizin Berlin, 13357 Berlin, Germany
* Correspondence: katharina.schmidt-bleek@charite.de; Tel.: +49-(0)30-450-659209; Fax: +49-(0)30-450-559938
† These authors contributed equally to this work.

Received: 20 February 2020; Accepted: 2 April 2020; Published: 4 April 2020


**Abstract:** Local pH is stated to acidify after bone fracture. However, the time course and degree of acidification remain unknown. Whether the acidification pattern within a fracture hematoma is applicable to adjacent muscle hematoma or is exclusive to this regenerative tissue has not been studied to date. Thus, in this study, we aimed to unravel the extent and pattern of acidification in vivo during the early phase post musculoskeletal injury. Local pH changes after fracture and muscle trauma were measured simultaneously in two pre-clinical animal models (sheep/rats) immediately after and up to 48 h post injury. The rat fracture hematoma was further analyzed histologically and metabolomically. In vivo pH measurements in bone and muscle hematoma revealed a local acidification in both animal models, yielding mean pH values in rats of 6.69 and 6.89, with pronounced intra- and inter-individual differences. The metabolomic analysis of the hematomas indicated a link between reduction in tricarboxylic acid cycle activity and pH, thus, metabolic activity within the injured tissues could be causative for the different pH values. The significant acidification within the early musculoskeletal hematoma could enable the employment of the pH for novel, sought-after treatments that allow for spatially and temporally controlled drug release.

**Keywords:** pH change; musculoskeletal system; bone healing; muscle injury; initial healing phase; pH-triggered drug release

## 1. Introduction

The pH is tightly regulated in the living organism, with values ranging from 7.35 to 7.45. There are only a few situations known in which a deviation from the physiological pH is not associated with sickness—for example, the acidification of muscle tissue during high muscle activity [1,2]. Disease-associated pH deviations occur under conditions in which oxygen cannot be properly transported into the tissues, e.g., after injuries due to a rupture of blood vessels or ischemic disorders [2], which induces local hypoxia [3,4] along with tissue damage. Another reason for perturbation of

homeostatic pH is described by the Warburg effect [5] in cancer cells, which favor aerobic glycolysis over oxidative phosphorylation [3], resulting in a decrease in external pH, especially in hypoxic regions of the tumor [6]. All the above examples share a common underlying principle: a change in metabolic processes towards anaerobic lactate fermentation as the main pathway for energy generation by glucose catabolism. This indicates that metabolic activity can alter the local environment, such as when acidic metabolites are transported out of the cell and thereby acidify the microenvironment [7]. Since significant deviations from physiological pH are strongly associated with the disease state of the organism, the pH could be considered a marker for certain diseases. In wound healing, the pH value is suggested as a parameter for both diagnostic and theranostic purposes [8]. Moreover, recent advances in the field of stimuli-responsive drug delivery [9,10] allow for utilization of the pH as an endogenous trigger for drug release in wound healing [11] and solid tumors [9,12,13].

It is well known that the pH is a parameter of utmost importance for bone homeostasis and the skeleton exerts a homeostatic role in buffering excessive acids [14–16]. Osteoclasts can be activated by acidic pH, with local acidification in resorption pits being one of the mechanisms of action for bone catabolic processes [17,18]. Osteoblasts, on the contrary, are sensitive to acidosis, which can decrease or even inhibit matrix mineralization [18,19]. Moreover, it is widely accepted that bone fracture evokes a local acidification of the fracture environment [20,21]. However, the timing and the extent of acidification remain largely unknown. Street et al. studied pH changes upon injury by comparing the pH values of supernatants of human fracture hematomas with hemolyzed control plasma [22]. No deviation from physiological pH was observed in either control plasma samples or supernatants collected from hematomas obtained approximately 12 h post fracture. However, the sample preparation method included centrifugation, freezing and thawing [22], a protocol that might have affected the pH. In another study, the relationship between mineralization and pH value was investigated in a rat osteotomy model [23]. The pH of the bone repair tissue was lower than the pH of control serum during the first week after osteotomy with a pH of 7.2 as the lowest value measured at two days post fracture followed by a continuous increase. The finding of an initial pH drop post osteotomy is in line with a number of studies summarized by Newman et al. [24]. Comparing the mean minimum pH values and the recording time points used in these studies, which involved various species from rodents to dogs to humans, the pH values measured within the first 8 days post fracture ranged from 4.2 to 7.19 [24]. Thus, the data remains inconclusive, as there is wide variation in the recorded values between the studies. This may be due to the individual study design and measurement time points, especially for the early healing time points, where data is scarce. Therefore, no reliable statement can be made about the pH of the fracture hematoma.

In this study, we aimed to investigate the changes and dynamics in pH in the musculoskeletal system after injury to define target pH values for novel pH-dependent treatment approaches. To understand how the local pH is affected at early stages of the bone healing cascade and whether the effect on pH due to bone fracture can be compared to other injuries of the musculoskeletal system, a sheep and a rat model were utilized to monitor immediate to early deviations in pH values in vivo up to 48 h after injury. To the best of our knowledge, this is the first study conducting parallel pH measurements in hematomas originating from the injury of two musculoskeletal tissues within the same animal, which therefore excludes issues of animal-specific differences that could affect this comparison. We observed acidification in both fracture and muscle hematomas without clear tissue-dependent effects. At all time points, and in both hematomas, high inter-individual differences were detected. Focusing on the fracture hematoma, we aimed to unravel the cause of this inter-individual variability by studying cellular density and aerobic catabolic activity. While no correlation of cellular density and pH was detected, a link between tricarboxylic acid cycle and local pH could be demonstrated. In light of a continuous demand for novel, pharmacological interventions to treat cases of musculoskeletal impaired healing after trauma, providing actual in vivo local pH values after injury could be of high relevance for the development of stimuli-responsive drug release systems.

*Int. J. Mol. Sci.* **2020**, *21*, 2513 3 of 18

## 2. Results

Based on the aim of this study to provide target values for the development of pH-sensitive biomaterials that can be applied in the context of bone regeneration, we focused on early phases post injury and on the hematomas formed after bone or muscle trauma. Bone and muscle are highly vascularized key tissues of the musculoskeletal system. In the clinic, patients usually present with a mixed muscular and skeletal trauma. However, in order to distinguish between hematomas arising from a trauma to either bone or muscle, standardized, isolated defects were chosen. Moreover, in previous studies comparing bone fracture and soft tissue hematoma, we unraveled distinct differences in terms of cellular composition, pro-/anti-inflammatory cytokine secretion and gene expression [25,26]. Therefore, we investigated whether all the above differences are accompanied by variations in pH changes as well.

### *2.1. Sheep Study: pH Drop upon Hypoxia Following Injury*

For the investigation of changes in the local pH within the hematoma, a pilot in vivo pH measurement in sheep was initiated directly after injury, thereby allowing for the monitoring of changes in the very early phases of healing. This measurement was integrated in another study, thereby following the 3R principles (replace, reduce, refine) [27]. The pH within the osteotomy hematoma ($n$ = 4) and the muscle trauma hematoma ($n$ = 4) was tracked over three hours (Figure 1A, B). A pH drop was detected in the osteotomy hematoma in the majority of animals (Figure 1A), albeit with pronounced inter-individual variations. After 3 h, the mean pH of all animals was 7.21 ± 0.13. Except for one animal, this local acidification was also detected in muscle hematomas (Figure 1B) with stronger pH deviations and a mean pH of 7.04 ± 0.3.

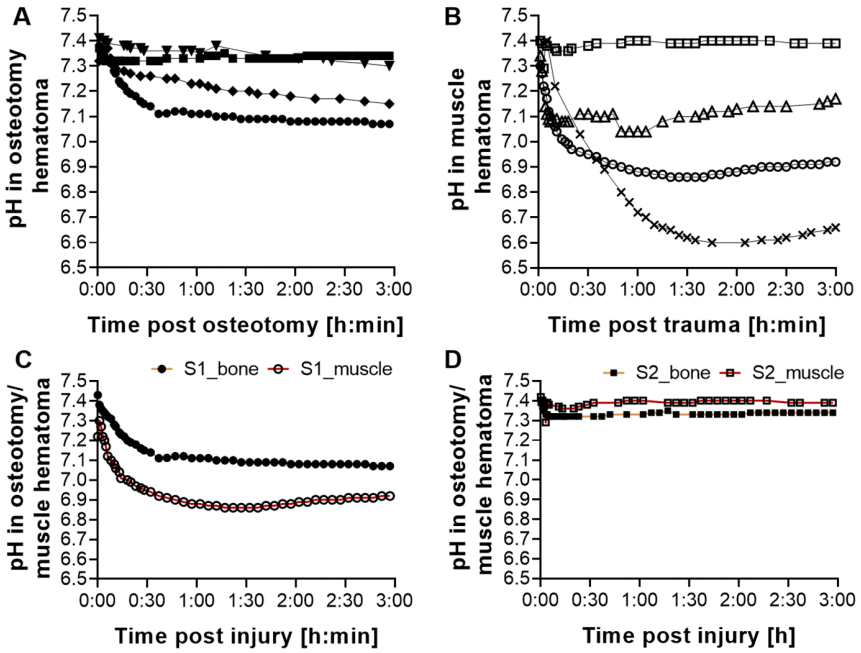


**Figure 1.** Local acidification in emerging hematomas after osteotomy and muscle trauma. Measurement of pH values over the indicated time in a proximal tibia shaft (**A**) and muscle injury in the Vastus lateralis (**B**) that corresponded in size to the tibia bone injury. Each line in the graph represents the development in local pH for one animal. While a drop in pH was detected in both bone and muscle hematoma for most animals, the inter-individual variations were high. The range of pH variations was broader after muscle trauma. Parallel pH measurement of bone and muscle hematoma for two animals (**C**,**D**) revealed intra-individual variations in addition to the values measured inter-individually. Each line in the graph represents the development in local pH separately for the osteotomy (yellow line) and muscle (red line) hematoma within the same animal (S1 or S2).

In order to investigate whether the inter-individual variations would be similar in both muscle and osteotomy hematoma, a parallel pH measurement was conducted in two animals (Figure 1C,D). Interestingly, in addition to the inter-individual variations, intra-individual differences were also observed. While in one animal, the pH in the osteotomy hematoma was lower compared to the muscle pH, it was the opposite in the second animal. Hence, these findings indicate a general acidification of the forming hematomas without clear tissue-dependent effects. Due to the embedding of this study in an ongoing in vivo study, in line with the 3R principles, the number of animals and access to defect sites were restricted, and, furthermore, the time span for measurement was limited to the very early phases of musculoskeletal healing.

### 2.2. Gene Expression Analysis in Sheep Fracture Hematoma

In an earlier study in sheep, the fracture hematoma of a stable fixed osteotomy of the tibia at 1, 4, 12, 24, 36, 48 and 60 h was harvested in order to conduct gene expression analysis [25]. The aim was to understand cellular reactions with respect to changes in the local environment. If the cellular processes were still ongoing, then the cells should express genes allowing for the transport of glucose into the cell due to increased energy demands. In conditions of oxygen deprivation, glycolysis and subsequent lactate fermentation generate less energy/ATP per mol glucose than aerobic respiration, therefore, glucose transporter genes must be upregulated to meet energy demands. Accordingly, the glucose transporter 1 (*GLUT1*) was analyzed to determine enhanced glucose uptake. In addition, hypoxia-inducible factor-1α (*HIF-1α*), a gene upregulated during hypoxia, heme oxygenase-1 (*HMOX1*), a pro-angiogenic, anti-inflammatory and cytoprotective protein [25,28] that can be induced by injury, and glyceraldehyde-3-phosphate dehydrogenase (*GAPDH*), a classically used house-keeping gene and glycolytic enzyme, were also analyzed (Figure 2). Increased *GLUT1* expression at 4 h post osteotomy indicates that cells try to enhance the import of glucose post injury. *HMOX1* increased in the hematoma with the mounting hypoxic stress, peaking at 36 h post fracture. Similarly, *HIF-1α* showed the highest induction at 36 h post osteotomy, suggesting that the tissue is indeed hypoxic. *GAPDH* has been shown to be regulated by hypoxia in different cell types [29,30]. In line with the literature, *GAPDH*, showing a first peak at 12 h after vessel disruption indicating a shortage of oxygen, followed the pattern of *HIF-1α* expression in this study as well.

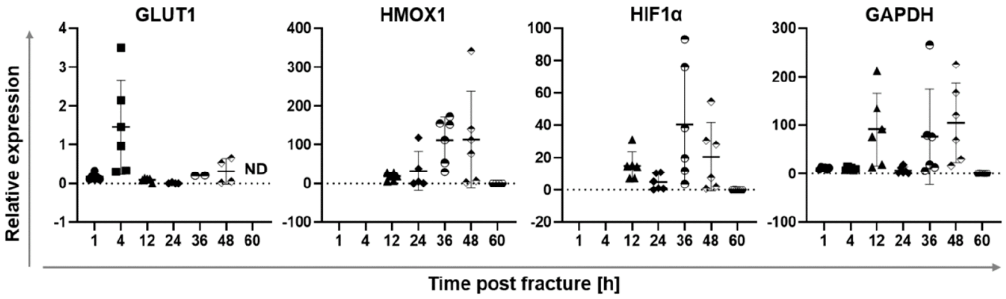


**Figure 2.** Gene expression in osteotomy hematoma tissue at 1, 4, 12, 24, 36 and 48 h post osteotomy. Samples were generated in an earlier study and gene expression of selected targets of interest was analyzed. *HIF-1α*, *GLUT1* and *HMOX1* have been previously published (adapted from [25]). *HIF-1α* and *HMOX1* expression was analyzed starting from 12 h post fracture. Results are depicted as scatter plots, each point represents the mean gene expression detected in the osteotomy hematoma for one animal. All samples were measured in triplicate. For all animals per time point ($n = 6$) the mean gene expression ± SD is shown. Different signs (circle, square, triangle and rhombus) indicate the different time points. ND: non-detectable expression.

This data indicates that the genetic response to developing hypoxia is not immediate, as indicated by the lack of upregulation of *GLUT1* and *GAPDH* genes at 1 h post injury, but develops over time. It is initiated by an upregulation of *GLUT1* expression at 4 h, followed by an increased expression of

hypoxia-related and -regulated genes. Combining these insights with the mild decrease in local pH of the fracture hematoma measured in sheep in the pilot in vivo study up to 3 h post fracture (Figure 1) suggests that hypoxic effects and, thus, hypoxia-induced pH acidification could be more pronounced at later time points post fracture. Therefore, another animal study was performed to analyze longer time periods after injury in order to test the hypothesis that lower pH values due to oxygen shortage would emerge with more time.

### *2.3. Rat study: pH Drop during Hematoma Maturation Following Injury*

For the analysis of pH development over a longer time period, an in vivo pH measurement in the osteotomy gap of rats at 4, 10, 24 and 48 h post osteotomy was initiated (Figure 3A), which includes the phases of hematoma formation, pro-inflammation and initial anti-inflammatory reaction of the bone healing process with the latter initiating revascularization [31]. Revascularization could be detected in the rat osteotomy hematoma at three days post osteotomy in another study [32]. Hence, with our experimental time interval, we aimed to cover the entire hypoxic phase.

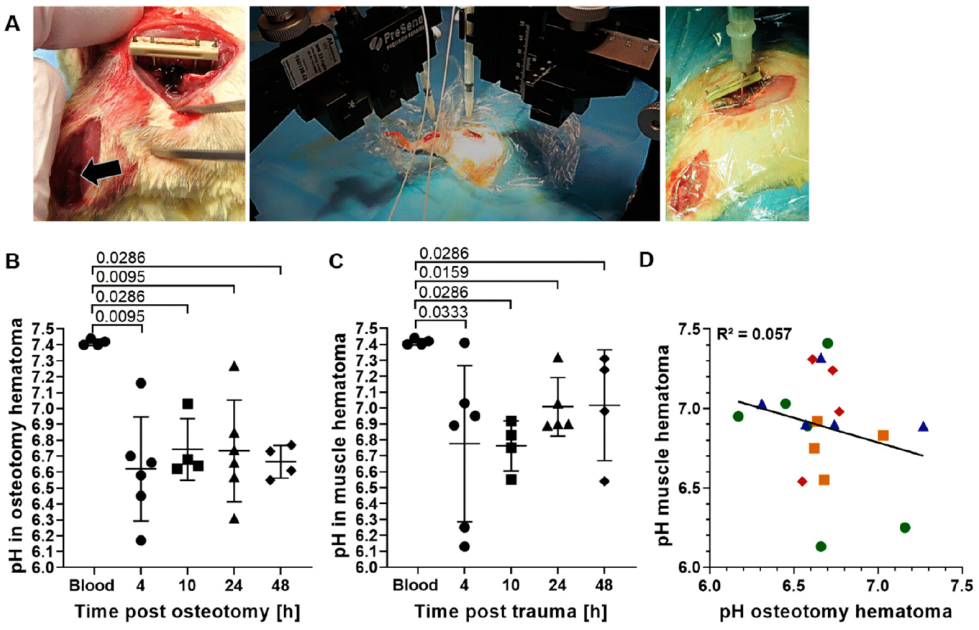


**Figure 3.** In vivo pH measurement at 4, 10, 24 and 48 h post osteotomy and muscle trauma. (**A**) Surgical approach and in vivo pH measurement. From left to right: muscle trauma and Musculus soleus (arrow) and osteotomy with a 5 mm gap size and an external fixation (RISystems); simultaneous and continuous pH measurement within muscle and osteotomy hematoma using optical microsensors (PreSens Precision Sensing) with precise positioning via micromanipulators; close-up image of placement of the pH sensor in the osteotomy hematoma. (**B**) Scatter plot of individual mean pH of the osteotomy hematoma per time point. (**C**) Scatter plot of individual mean pH of the hematoma formed after muscle trauma per time point. For (**B**) and (**C**): Each value depicted (point per time point) represents the measurement of the respective hematoma for one animal. Mean ± SD is shown for at least four animals per time point. Circles: 4 h, squares: 10 h, triangle: 24 h and rhombus: 48 h time point post injury. Two-way Mann–Whitney U test was performed, comparing the measurement time points to control (blood). (**D**): Local pH in osteotomy hematoma plotted against local pH in muscle hematoma. Linear regression line is depicted for better visualization. Both parameters ($n$= 19) passed the D'Agostino–Pearson normality test ($\alpha$= 0.05, QQ plot depicted in Supplementary Figure S2A). Hence, Pearson correlation was calculated, yielding an $R^2$ value of 0.057. Green circles: 4 h, yellow squares: 10 h, blue triangles: 24 h, and red rhombus: 48 h.

In a first test, the physiological pH in freshly collected blood from rats ($n$ = 4) was confirmed to be in the same range as the physiological pH in human blood, with a mean of 7.41 ± 0.02, and was used as comparator for the pH measured in the hematomas.

The in vivo measurement of the osteotomy hematoma at all investigation time points revealed a significant decrease in pH, with mean pH values ranging from 6.62 ± 0.33 to 6.74 ± 0.19 (Figure 3B). The individual pH variations per animal over the measurement period were negligible with a mean SD of 0.02 (Supplementary Figure S1B). However, the inter-individual differences at each time point were substantial, as seen by the rather large variation of the data for the analyzed time points. Similar to the osteotomy hematoma, a significant drop from physiological pH as well as pronounced inter-individual differences were observed within the muscle hematoma at all time points (Figure 3C). The mean pH of muscle hematoma per time point was slightly higher compared to the osteotomy hematoma, ranging from 6.76 ± 0.16 to 7.02 ± 0.35. Moreover, the mean pH per time point was found to increase only for the muscle hematomas between the 10 and 24 h time point from 6.8 to 7.0, while the mean pH in bone hematoma remained constant over the testing period (Figure 3B,C).

The high inter-individual differences seen in the hematomas of both musculoskeletal tissues raised the question whether the extent of acidification in both hematomas would be similar or whether either the bone or muscle hematoma would be consistently more acidic within each individual animal. Since the pH in both hematomas was measured in parallel in the same animal (Figure 3A), the difference between pH values of both tissues could be calculated individually (Table 1). In case of a general pattern of higher acidification of one hematoma group compared to the other, the pH could be postulated to be dependent on the tissue that the hematoma originated from. In line with our findings in sheep (Figure 1C,D), no clear pattern in hematoma acidification was observed over the entire testing period, meaning that for some animals, the osteotomy hematoma was more acidic than the muscle hematoma, while it was the reverse for others (Table 1). Despite the lack of a constant pattern for all time points, at later time points (24 and 48 h), the majority of bone hematomas were found to be more acidic than the muscle hematoma. This finding is supported by a linear regression analysis of the local pH within both hematomas, with each point representing an individual animal (Figure 3D). Here, the calculation of Pearson correlation yielded an $R^2$ value of 0.057, indicating that the local pH in osteotomy and muscle hematoma are not correlated.

**Table 1.** Difference in pH values measured within the osteotomy and muscle hematoma per animal and time point. At all time points, the difference between both pH values was quite variable between animals and did not follow the same trend.

| Time Point | Δ pH (Fracture Hematoma - Muscle Trauma) | | | |
|---|---|---|---|---|
| | 4 h | 10 h | 24 h | 48 h |
| Individual Δ pH per animal and time point | 0.53 | −0.13 | −0.33 | −0.70 |
| | 0.92 | −0.28 | −0.16 | −0.21 |
| | −0.58 | 0.13 | −0.71 | −0.51 |
| | −0.31 | 0.20 | −0.66 | 0.01 |
| | −0.78 | | 0.38 | |
| | −0.71 | | | |

Similar to the in vivo pH measurement in sheep, the in vivo pH measurement in rats confirmed the acidification within both hematomas, but with a stronger degree of acidification in the rat study. Moreover, in both studies, no clear tissue-dependent effects of pH acidification pattern for bone and muscle hematomas could be detected (Figure 1C,D, Figure 3D, Table 1) and pronounced inter-individual differences within each hematoma group were observed.

### *2.4. Factors Influencing the Variability in Local pH*

#### 2.4.1. The Cellularity of the Hematoma Does Not Correlate with Local pH

We next aimed to unravel the underlying cause for the inter-individual variability in pH values by quantifying the number of cells found in the osteotomy hematoma. As a result of injury-induced oxygen shortage, we hypothesized that the cells shift to anaerobic respiration and, thus, the number of cells would positively correlate with the amount of generated lactate, leading to a pH change. To test this hypothesis, the rat osteotomy hematomas were sectioned and H&E stained, and then the respective images were analyzed for cell number in conjunction with the measured pH (Figure 4). At all investigation time points, cellular density and local pH were not found to follow a similar pattern (Figure 4A), with cellular density not being correlated to pH (Figure 4B). At 10 h post injury, the hematoma with a pH of 7.1 shows areas of high cellular density that are not present in the more acidic hematoma (pH 6.6 (I)) as well as an overall higher cellular density (Figure 4A,C). At the 24 h time point, the cellular density of the most (pH 6.3) and least (pH 7.22) acidic hematoma exhibit approximately similar cellular densities (Figure 4A,C). Thus, this histological investigation disproved the hypothesis of a direct relationship between cell density and reduced pH.

#### 2.4.2. Differences in Metabolic Processes within the Hematoma Linked to Local pH

Since the cellularity of the hematoma did not correlate with the local pH value, we hypothesized that potential differences in metabolic processes within the cells of the hematoma could have caused different degrees of local acidification. Therefore, we investigated metabolites of the catabolic glucose pathway within the rat osteotomy hematomas. To avoid the influence of cellularity, the relative abundance of metabolites was quantified by normalization to the median intensity per sample using the whole data matrix of each hematoma. Based on the gene expression data in sheep, which showed a first upregulation of hypoxia-related genes at 12 h (Figure 2) and additional previous findings, indicating a major shift in cellular response in the time interval between 12 and 24 h [25], the fracture hematomas at 10 and 24 h were chosen for metabolomic analysis.

First, it was crucial to confirm the presence of D-glucose as the starting metabolite for all cellular respiratory processes. Calculating the ratios of relative quantities of D-glucose to the metabolites representing the first and the last step of the glycolytic cycle (D-glucose-6-phosphate and pyruvic acid) revealed that D-glucose was available in greater quantity than downstream metabolites for all the hematomas analyzed. This indicates that metabolic respiratory processes could occur and should not be stalled due to glucose shortage (Table 2).

**Table 2.** Ratios demonstrating glycolytic activity at 10 and 24 h post osteotomy.

| Time Post Osteotomy | 10 h | | 24 h | | |
|---|---|---|---|---|---|
| **Local pH** | **6.64** | **7.05** | **6.28** | **6.66** | **7.22** |
| **D-glucose 6-phosphate/D-glucose** | 0.001 | 0.003 | 0.171 | 0.004 | 0.017 |
| **Pyruvic acid/D-glucose** | 0.158 | 0.236 | 0.584 | 0.685 | 0.247 |

Under anaerobic conditions, lactic acid is produced and is pumped into the extracellular space, which results in an acidification of the local environment [33]. In our metabolomics analysis, lactic acid, which would give a direct indication for potential differences in anaerobic glucose catabolic pathways, could not be detected. However, differences in aerobic pathway activities could also provide evidence for a link of metabolic activity and pH. Thus, metabolites of the tricarboxylic acid (TCA) cycle as a key component of the aerobic respiration were studied. Figure 5A exhibits a metabolic heat map for relative quantities of metabolites belonging to the TCA cycle as well as for ratios of glycolysis and TCA metabolites in conjunction with the pH per hematoma at 10 and 24 h post injury. Figure 5B illustrates the pathways underlying cellular respiration, including the aerobic as well as the anaerobic energy generation via glucose catabolism. Interestingly, the relative quantity of TCA metabolites

followed the same pattern as the pH—lower relative amounts of TCA metabolites were detected in hematomas with low pH compared to samples with higher pH of the same time point (Figure 5A). This was true for both the 10 and 24 h time points and is also reflected by the ratios of TCA metabolites against the end product of glycolysis, pyruvic acid. Moreover, forming a ratio of two consecutive TCA metabolites revealed the same trends. Taken together, this indicates that TCA activity seems to be higher in hematoma tissues with a higher pH. Thereby, aerobic metabolic activity can be related to local pH, with a higher pH being linked to higher activity in TCA activity, while local pH does not seem to be cellularity dependent.

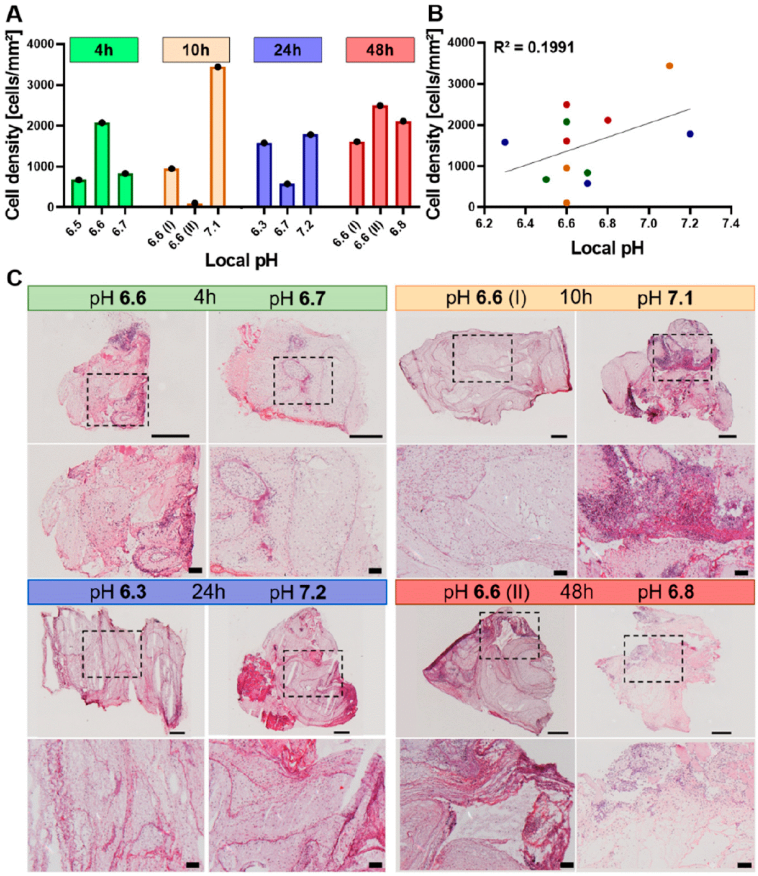


**Figure 4.** No direct link between the cellularity of hematoma and pH value. (**A**) Quantification of cells contained in the H&E-stained sections per $mm^2$ of hematoma grouped by time point and pH ($n$ = 3 for each time point). The total hematoma area was measured in $mm^2$, cells were identified by hematoxylin staining the nuclei and the density was calculated by dividing the total cell count by the total hematoma surface area. (**B**) Cellular density of all hematomas (4, 10, 24, 48 h) plotted against local pH. Linear regression line is depicted for better visualization. Both parameters passed the D'Agostino–Pearson normality test ($\alpha$= 0.05, QQ plot depicted in Supplementary Figure S2B,C). Hence, Pearson correlation was calculated, yielding an $R^2$ value of 0.1991. (C) Representative H&E-stained sections of osteotomy hematomas at 4, 10, 24 and 48 h post osteotomy. Samples with a differing pH were chosen as examples for visualization. For each time point, the overview (top panel) and the close-up image (bottom panel) are shown in conjunction with the in vivo measured pH. The dashed box in the overview image indicates the area that is magnified in the bottom panel. Purple dots represent nuclei of cells, whereas the light to strong pink color stains structures such as cytoplasm, proteins and connective tissue. The scale bars indicate 500 µm for the overview image taken at 5x magnification or 100 µm for the close-up image taken at 10x magnification.

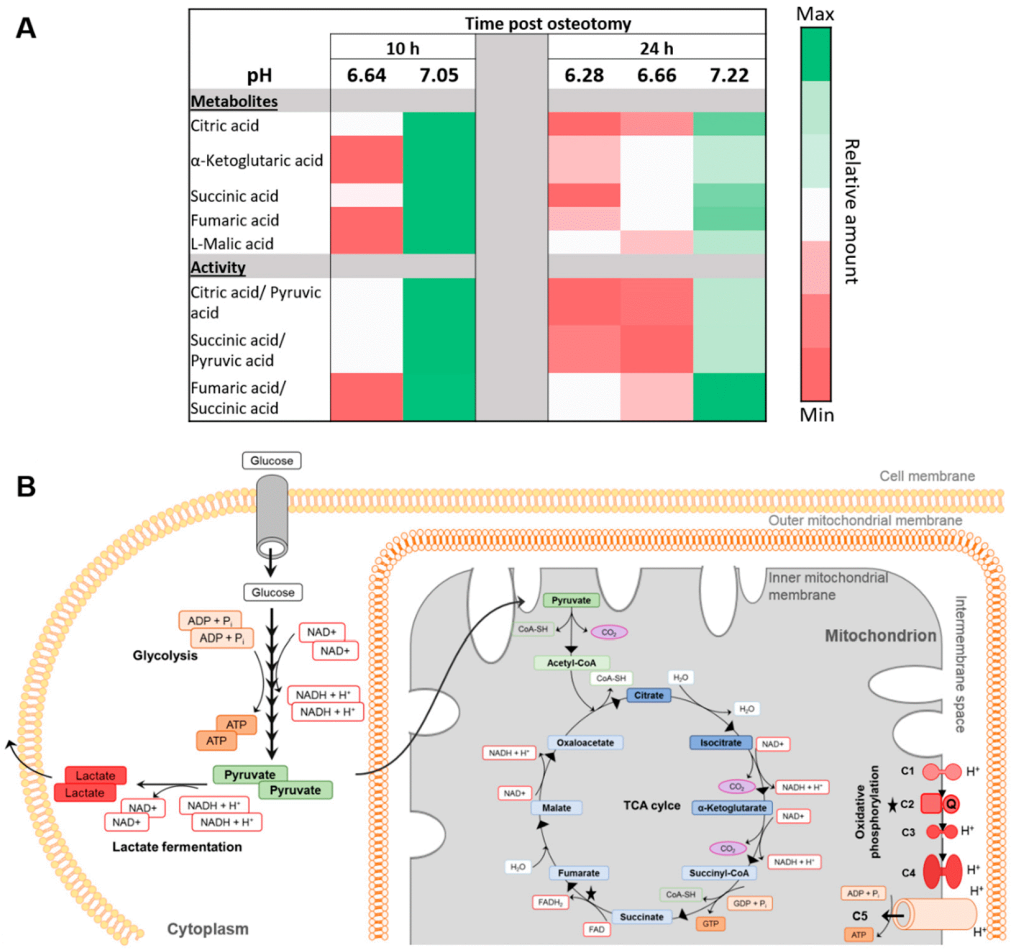


**Figure 5.** Metabolomic analysis of osteotomy hematomas—correlation between TCA activity and pH. (**A**) Heatmap of metabolites of the TCA and ratios between TCA and glycolysis products for 10 h ($n = 2$) or 24 h ($n = 3$) post osteotomy in conjunction with the individual pH measured in each hematoma samples that is represented here. (**B**) Simplified scheme of metabolic pathways underlying cellular respiration. Glycolysis occurs under aerobic and anaerobic conditions. Recovery of $NAD^+$ under anaerobic conditions occurs in eukaryotic cells exclusively via lactate fermentation. Lactate is transported across cell membranes by cotransport with protons, thereby an acidification of the extracellular environment can occur. Under aerobic conditions, pyruvate enters the mitochondrion and participates in the TCA cycle. Energy in the form of ATP is generated during oxidative phosphorylation via proton shuttling through complex (**C**) 1, 3 and 4 into the intermembrane space and proton retrieval along the gradient by complex 5 (proton pump). Oxygen is needed at the end of the electron transport chain to generate $H_2O$.

## 3. Discussion

In this study, we investigated pH deviations from the physiological range during the very early to early phases post injury up to 48 h in vivo in sheep and rats to provide target pH values for novel pH-dependent treatment approaches. The pH changes were measured simultaneously in two injured tissues of the musculoskeletal system, the hematoma formed upon bone fracture and muscle trauma. To the best of our knowledge, this is the first study to examine pH changes in two musculoskeletal tissues in parallel in the same animal, thereby avoiding animal-specific variability. Local acidification was observed in the majority of both bone and muscle tissues in sheep, as well as in rats for which the mean pH dropped significantly below physiological pH (Figure 1, Figure 3). Gene expression studies in sheep fracture hematoma revealed the hypoxia-related upregulation of genes such as

*GLUT1* to be initiated not immediately after injury, but starting at 4 h (Figure 2) [25]. Moreover, the hypoxia-sensitive expression of *GAPDH* could be demonstrated, which has been described for in vitro cell systems [29,30], but has not been previously reported for ex vivo sheep hematoma tissue. The observed local acidification supports published literature on pH deviations after fracture [24] and muscle injury [34]. However, in this study, we were focusing on very early to early healing phases, for which results of pH measurements were scarce and, so far, inconclusive. Moreover, we measured the extent of local acidification in vivo, which differentiates these findings from a number of previous studies that were summarized by Newman et al. [24]. Indeed, it became apparent during our study that the way the measurements are performed, e.g., the storage of the samples before measurement or the use of anti-coagulants, has a decisive influence on the results (Supplementary Figure S3), which indicates the significance of in vivo pH measurements. Interestingly, in vivo nuclear magnet resonance (NMR)-based pH measurements of rat fracture hematomas in another study showed the lowest pH of 7.19 within the fracture hematoma after two days, which was the first measurement time point [24]. In the current study, the average pH of the rat fracture hematoma at 48 h post fracture was 6.67 ± 0.1, the maximum pH measured at this time point was 6.77. Comparing all the previous studies mentioned [24], the results of the NMR and our pH measurements are among the most similar, despite utilizing different measurement methods. Of note, the non-invasive Raman spectroscopy approach utilized by Newman et al. [24] is an estimation of pH based on the magnetic resonances of phosphorus nuclei within tissues, which might explain the differences in the measured pH values. The local pH measured after muscle incision in another study [34] revealed a local mean acidification of 6.96 ± 0.04 at 24 h post incision, which is in strong agreement with our pH measurement in the muscle hematoma yielding mean pH values of 7.01 ± 0.18 at 24 h post osteotomy. Considering the acidification of the muscle or osteotomy hematoma intra-individually in sheep and rats, this study revealed a dissimilarity in extent and pattern of acidification among all animals. Thus, local acidification upon injury of these musculoskeletal tissues seems to occur without distinct tissue-dependent effects during the early healing phases, despite subtle differences in the kinetics of local recovery of physiological pH (Figure 3).

Moreover, we detected pronounced inter-individual differences in pH values of the hematomas at all investigated time points. Thus, we aimed to unravel potential underlying causes for this variability. The rupture of blood vessels upon injury creates hypoxic conditions (Figure 2) [2–4,35] and evokes the switch to anaerobic energy supply [3,4], resulting in lactate production (Figure 5B) and, thus, causing local tissue acidification (Figure 1, Figure 3) [23,24,36]. While histological analysis showed that cellular density within the hematoma is not causative for changes in tissue pH (Figure 4), metabolic analyses indicated that the pH is linked to the activity of cellular respiration pathways (Figure 5). In all samples, D-glucose was detectable, allowing for glycolysis to occur. According to the Pasteur effect, fermentation is inhibited in the presence of oxygen [37]. The metabolism of glucose is regulated by allosteric inhibition or activation of glycolytic enzymes. Whereas ATP and some metabolites of the glycolysis and TCA cycle decrease the rate of glycolysis, AMP, ADP and Pi (so-called low-energy metabolites) increase the rate [37,38]. Hypoxia leads to a decrease in oxidative phosphorylation (OXPHOS), which increases the abundance of low-energy metabolites and, thus, increases the glycolysis rate. To meet the energy demand, pyruvate has to be reduced to lactate instead of entering TCA cycling, thereby, a reduction in TCA activity links to an increase in lactate fermentation. Accordingly, when glycolysis coupled to lactate fermentation is the main pathway to ensure energy supply, aerobic respiration consisting of the TCA cycle and OXPHOS is reduced or stalled. TCA cycle and OXPHOS are coupled, since NADH and FADH2 need to be oxidized in the electron transport chain to allow for continuous TCA cycle activity. Since we could not detect lactate during our metabolomic analysis, as it is eluted at the beginning of the chromatogram and therefore not always detectable, we focused on metabolites of the TCA cycle. As mentioned above, the underlying assumption was that a higher activity in TCA cycle would reversely indicate a lower activity in anaerobic lactate fermentation, since ATP, NAD+, and FAD can be generated more effectively. Conversely, the reduction of TCA activity could be an indirect indication for increased lactate fermentation. It should be noted

that additional processes affecting TCA metabolite abundance exist, as some TCA intermediates can be used for biosynthesis and be replenished by other mechanisms such as glutaminolysis [39]. However, this is beyond the scope of this investigation, which compares the hematomas of one tissue separately for each time point. According to our findings, in hematomas with a comparatively higher pH, the TCA cycle seems to be more active as shown by higher relative amounts of TCA metabolites and TCA metabolite to pyruvic acid ratios compared to hematoma samples of the same time point with a lower pH value. Remarkably, the ratio of fumaric acid over succinic acid also related to pH, i.e., higher pH values correspond to a higher ratio of these metabolites (Figure 5A). The enzyme succinate dehydrogenase subunit A catalyzes the conversion of succinic acid to fumaric acid. This enzyme participates in both the TCA cycle and the electron transport chain/OXPHOS and thereby couples both processes [39,40]. A higher rate of TCA cycle and succinate dehydrogenase activity could suggest that aerobic respiration can still take place and, therefore, less pyruvic acid would be fermented to lactate, leading to reduced tissue acidification and a less pronounced pH drop. Intriguingly, work by Khacho et al. suggests that mild extracellular acidosis, which can be evoked by hypoxia, can indeed induce a restructuring of mitochondria, thereby maintaining efficient ATP production by the mitochondria, despite oxygen shortage [33].

The knowledge gained in this study could pave the way for novel pH-mediated local treatments of musculoskeletal injuries by defining target values for pH sensitivity that would need to be matched by suitable biomaterial development. In a study by Chu et al., a nanosystem was developed that exhibits a more than doubled cumulative drug release in a pH 6.5 compared to a 7.4 environment [41], hinting at the technical feasibility of pH-mediated interventions after injury with mean target values of 6.69 and 6.89. The need for novel pharmacological interventions for musculoskeletal injuries becomes apparent by appreciating that 10%–20% of bone fracture cases exhibit delayed healing or develop into non-unions [42,43]. Injuries of the musculoskeletal system represent a major health issue, with fractures making up approximately 16% of injuries that were treated in medical care in the US in 2012 [44]. This percentage is predicted to rise due to an aging population with a prolonged life span [45]. An increase in age coincides with a rather pro-inflammatory systemic milieu, a phenomenon called "inflamm-aging" [46], and a higher prevalence of comorbidities such as obesity and diabetes, both limiting the regenerative capacity, e.g., in fracture cases [47]. Furthermore, as a clear relationship between the local pH of healing bone tissue and mineral deposition has been described [23], future studies could additionally investigate whether the extent of tissue acidification post injury corresponds to different healing capacities, thereby potentially further increasing the demand for such therapies. A prolonged local acidification phase can be assumed to impact the progression of bone healing, as abundant clinical evidence exists on systemic acidosis patients that present decreased bone quality and increased fracture risk [48–53] and mineral deposition occurs during the local alkalization phase that follows the initial acidification [23]. Some studies observed a direct link between the degree of systemic acidosis and fracture risk [51] or bone quality parameters such as bone mineral density (BMD) and bone loss rates [53]. Moreover, a pre-clinical study compared the pH dynamics and time to union as an indicator for mineral deposition in normal and experimentally delayed bone healing [36]. A prolonged phase of local acidification and overall reduced subsequent alkalization was detected for the delayed healing group that coincided with an increased time to union and, thus, slower mineral deposition. Together, these studies evidence a clear relation between systemic pH and bone quality as well as suggest a link between healing delay and hampered local pH dynamics.

In conclusion, despite high inter-individual differences, a significant pH drop was observed in our study within the rat osteotomy and muscle hematoma across all time points investigated. Further, the detected range of pH value changes in different tissues and individuals appears to be linked to the different TCA cycle activity within the injured tissue—even without a vascular supply of oxygen. Using biomaterials sufficiently sensitive to mild deviations from physiological pH, pH-mediated local treatments could be conceivable for both bone and muscle injuries. However, further studies are needed to identify a stable and reproducible pH drop across multiple tissues and injuries and to

investigate a possible relationship between tissue acidification/alkalization dynamics and different healing outcomes in bone regeneration in clinically relevant animal models. For this, the comparison and longitudinal pH measurement in an age-related model of compromised healing [54] versus a young, normal healing model could prove insightful. Based on previous findings that provide evidence for an impaired re-vascularization in rodent fracture models in aged compared to young animals [32,55], a prolonged hypoxic phase causing an extended local acidification phase seems probable, but needs to be studied in depth. Since similar observations of age-dependent hampered angiogenic capacities were made in elderly human patients [56,57], a clinical application of such knowledge appears feasible, underlining the need for future research in this area.

## 4. Materials and Methods

### *4.1. Animal Studies*

Depending on the expected size of the sample, specimen characteristics and measurement set-up, different pH sensors were employed within this study. For the initial pilot study in sheep, we focused on the development of local pH immediately post injury, while for the rat study, we monitored pH changes over a longer time frame to understand how local pH is affected by early hematoma maturation processes.

### *4.2. Sheep Study*

The in vivo study in sheep was performed in accordance with the German Animal Welfare Act and was approved by the local animal protection authorities (Landesamt für Gesundheit und Soziales, LaGeSo; permit number G0216/13, approval: 28.10.2013; additional pH measurement approved in December 2015). The in vivo study was conducted in accordance with the German Animal Welfare Act, the National Institutes of Health Guide for Care and Use of Laboratory Animals and the Animal Research: Reporting of In vivo Experiments (ARRIVE) guidelines. The sheep in this trial were part of a larger study using adult female merino mix sheep (>2.5 years) for osteochondral healing, for which additional pH measurements at the endpoint of the study were approved by the local authorities, thereby following the "reduce" of the 3R principles (replace, reduce, refine) [27]. For the osteochondral healing study in which the pH measurement was included, the animals were held under deep anesthesia by a mixture of anesthesia gas (1.8%–2.0% isoflurane, 20%–30% nitrous oxide, pure oxygen) for 3 h before sacrifice. Within this time period, the pH measurement was integrated. The measuring period was determined by the above-mentioned ongoing animal study. Thus, only the immediate to early pH changes up to 3 h post injury could be investigated. Fentanyl dihydrogen citrate (Rotexmedica, Trittau, Germany) was given as intra-venous bolus injections repeatedly for analgesia.

A 6 mm drill hole in the shaft of the right tibia, as a representation of a forming hematoma after bone fracture, and/or a size-matched muscle trauma in the main body of the Vastus lateralis of the Musculus quadriceps by the use of a scalpel was created in a standardized manner without ceasing muscle function completely. Since the measurements occurred at the study end point and the forming hematoma was the tissue of interest, a complete osteotomy was avoided, as additional external fixation measures were not possible without disturbing the region used for the osteochondral study. The drill hole size and location were chosen to allow the entrance of the pH sensor into the medullary cavity. As the diameter of the bone marrow shaft is rather small, the proximal tibia was chosen. Here, the bone widens and allows immersion of the pH sensor in the bone marrow tissue. The pH sensor was inserted centrally into the defect, i.e., into the liquid phase of the injury-induced bleeding prior to coagulation, followed by suturing of the skin and pH measurement of the developing hematomas. The pH of the developing hematomas from both musculoskeletal tissues was measured. Measurements started right after injury and lasted for 180 min (max. measurement interval of 10 min) using a classical electrochemical pH microelectrode (8220BNWP Orion™ PerpHecT™ ROSS™ Thermo Fisher Scientific, Waltham, MA, USA). A total of 8 animals were measured, and the study size and allocation to the

different hematoma groups were dictated by the lead study (4 animals: muscle hematoma; 4 animals: bone hematoma; and in 2 animals of both groups muscle and bone hematomas were created).

### *4.3. Gene Expression Analysis*

Hematoma samples were generated in an earlier study and results from the expression analysis were partly published before in another context [25]. In brief, hematomas were generated by a stable fixated osteotomy in the tibia of sheep and harvested at 1, 4, 12, 24, 36, 48 and 60 h after surgery ($n$ = 6 per time point). A total of 150 mg of hematoma tissue was used for total RNA isolation. A volume of 1 mL of TRIzol (Invitrogen, Carlsbad, CA, USA) was used for homogenization with an ultra turrax. Subsequently, 200 µl chloroform (VWR, Radnor, PA, USA) was applied, and samples were mixed and incubated for 10 min before centrifugation. The upper phase was collected and diluted in a 1:2 ratio with 2-propanol. After centrifugation, the pellet was resuspended in 75% ethanol. Following centrifugation, the pellet was dried at 37 °C and resuspended in 20 µl diethylpyrocarbonate (DEPC) water. After incubation with 80 µl DNase Mix (Quiagen, Düsseldorf, Germany) for 15 min, the procedure was repeated. The final pellet was resuspended in RNase-free water for 10 min at 50 °C. Quality and quantity of the RNA was measured by spectrophotometry, and RNA was stored at -80 °C until further use. cDNA synthesis was carried out using random primers (Invitrogen, Carlsbad, CA, USA) and MMLV-Reverse Transcriptase-RNaseH Minus (Promega, Madison, WI, USA). Primers were designed to perform at 62 °C and to give rise to 150–300 bp products (Tib Molbiol, Berlin, Germany). PCR was performed using the iQ$^{TM}$Supermix (BIO-RAD, Hercules, CA, USA) and SYBR®Green (Invitrogen, Carlsbad, CA, USA) with an iQ$^{TM}$5 Cycler (BIO-RAD, Hercules, CA, USA). Cyclophilin A was applied as a housekeeping gene after determining the best stability in expression within this tissue using geNorm. For data analysis, the $2^{\Delta CT}$ method was used.

### *4.4. Rat Study*

The in vivo study in rat was performed in accordance with the German Animal Welfare Act and was approved by the local animal protection authorities (Landesamt für Gesundheit und Soziales, LaGeSo; permit number G0017/16, approval: 31.03.2016). The study design is graphically illustrated in the Supplements (Figure S4). The in vivo study was conducted in accordance with the German Animal Welfare Act, the National Institutes of Health Guide for Care and Use of Laboratory Animals and the ARRIVE guidelines. In total, 24 female Sprague–Dawley rats (12 weeks old) were included in this study. They were kept under obligatory hygiene standards as monitored according the FELASA standards. Water and food were available to the animals ad libitum, and the rats were kept in groups and randomly assigned to the different investigation time points. The temperature was set to 20 ± 2 °C and a light/dark period of 12 h was utilized.

During the surgery, they all received a balanced isoflurane (Forene, Abott, Wiesbaden, Germany) anesthesia mixed with oxygen and analgesics. After induction of anesthesia, analgetic (Buprenorphine, RB Pharmaceuticals, Berkshire, UK) and antibiotic bolus (Clindamycine, Ratiopharm, Ulm, Germany) treatment and application of eye ointment, the animals were placed on a heating plate set at 37 °C. For the osteotomy, after exposure of the bone, an external fixator (RISystem, Davos, Switzerland) was mounted on the lateral aspect of the femur, an osteotomy gap of 5 mm was created with a Gigli saw and a saw guide, thereby allowing hematoma formation. In this study, in contrast to the sheep study, a complete osteotomy was required due to otherwise spatial limitation for the forming hematoma that could have impeded the pH measurements. For the muscle trauma, the skin at the shank was cut caudally, the Musculus gastrocnemius was mobilized bluntly and the underlying Musculus soleus was isolated and crushed 2 times for 20 s with a clamp.

To investigate the pH changes following injury in a pre-clinical model, measurements were conducted at 4, 10, 24 and 48 h post injury. Our studies showed [25,26] that hypoxic conditions and the cellular reactions stabilize between 4 and 12 h (upregulation of *GLUT1* and *HIF1α*), indicating that acidification due to anaerobic energy metabolism will increase during hematoma maturation.

For the measurement in the small rat hematoma, a microinvasive needle-type optical pH microsensor (pH-1 micro combined with needle-type sensor (NTH-HP5), PreSens Precision Sensing, Regensburg, Germany) that includes a silica-based microfiber optic pH sensor system (sensor tip below 150 µm) for implementation in animal tissue [58] and on-the-spot continuous measurement within small volumes was utilized. This technique is based on the dual life time reference (DLR) method that uses two different fluorescent dyes, one dye being pH sensitive, and measures the pH-dependent phase shift of the two simultaneously excited fluorophores [59,60]. This microinvasive optical pH microsensor has been successfully utilized in previous studies to measure longitudinal pH in vivo in rodent animal models [34,61] and is moreover used for in vitro pH measurements [61,62]. Prior to the in vivo measurement, an in-house validation of the PreSens pH microsensors was accomplished by measuring the pH in human blood samples (Supplementary Figure S1A). For each investigation time point of the in vivo study, the pH within the hematomas was measured over a time period of two hours with a measurement interval of 10 s. For the time point 4 h after injury, the animals were kept in anesthesia until finalization. For all other time points, the animals recovered from anesthesia, were allowed normal activity and were treated with analgesia (Tramadolhydrochloride, Grünenthal, Aachen, Germany) that is optimized for this intervention for the other time points [63], before being anesthetized again for pH measurement. The last 30 min of the measurement were used for the evaluation of the pH values at the respective time points. The measurement was performed for $n = 6$ animals per time point (24 animals in total), and each measurement was an endpoint. Differences in final number of animals per time point depicted in the figures were due to sporadic premature deaths during anesthesia or technical issues with the optical pH sensor. After sacrifice, the osteotomy and muscle hematomas were harvested and stored at −80°C until further analyses.

### *4.5. Additional Analysis of Rat Fracture Hematoma*

#### 4.5.1. Histological Analysis of Rat Fracture Hematoma

For the histological analysis, the fracture hematomas were cut into sections that were 5 µm thick using the CryoStat (CM3050 S, Leica, Wetzlar, Germany). After 10 minutes of fixation with 4% formaldehyde, hematoxylin and eosin (H&E) staining was applied. Images were taken at given magnifications (5x and 10x) using a bright field microscope (Axioskop 40, Zeiss, Oberkochen, Germany). Cell density was estimated by calculating the number of cells detectable due to the hematoxylin-stained nuclei per hematoma surface area in $mm^2$ using the FiJi/ImageJ [64] software.

#### 4.5.2. Metabolomics Study of Rat fracture Hematoma

The sample preparation was performed according to metaSysX GmbH (Potsdam, Germany) standard procedure, a modified protocol from Giavalisco et al. [65]. Measurements were carried out with an Agilent Technologies Gas Chromatography (Agilent Technologies, Santa Clara, CA, USA) coupled to a Leco Pegasus HT mass spectrometer (Leco Instrumente, Mönchengladbach, Germany, which consists of an electron impact ionization source and a time of flight mass analyzer. Column: 30 m DB35; starting temp: 85 °C for 2 minutes; gradient: 15 °C per minute up to 360 °C. NetCDF files that were exported from the Leco Pegasus software were imported to "R". The Bioconductor package TargetSearch was used to transform retention time to retention index (RI), to align the chromatograms, to extract the peaks, and to annotate them by comparing the spectra and the RI to the Fiehn Library and to a user-created library. Annotation of peaks was manually confirmed in Leco Pegasus. Analytes were quantified using a unique mass. The data was normalized to the sample median.

### *4.6. Statistics*

Detailed information on all statistical analyses performed, including sample size and depicted values are included in the figure legends. A two-way Mann–Whitney U test was applied when indicated. To test for correlation, the D'Agostino–Pearson normality test was conducted ($\alpha$= 0.05) on

all parameters (local pH in osteotomy/muscle hematoma and cellular density on the entire data set including all time points), followed by Pearson correlation analysis and $R^2$ calculation. To perform the statistical analysis, we used GraphPad Prism® (Version 8.0; GraphPad Software, San Diego, CA, USA). The confidence interval was set to 0.95, and $p < 0.05$ was considered significant. Exact $p$-values for significant changes are stated in the figures.

**Supplementary Materials:** Supplementary materials can be found at http://www.mdpi.com/1422-0067/21/7/2513/s1.

**Author Contributions:** J.C.B., conceptualization, formal analysis, investigation, methodology, software, visualization, writing—original draft, and writing—review and editing; A.X.H.M., resources, software, and writing—review and editing; A.E., investigation, methodology, and writing—review and editing; C.S., investigation, and writing—review and editing; H.S., investigation, methodology, and writing—review and editing; E.L., conceptualization, funding acquisition, investigation, and writing—review and editing; G.N.D., supervision, and writing—review and editing; S.T., conceptualization, and writing—review and editing; K.S.-B., conceptualization, funding acquisition, investigation, methodology, project administration, supervision, and writing—review and editing. All authors have read and agreed to the published version of the manuscript.

**Funding:** This project has received funding from the European Union's Horizon 2020 research and innovation program under grant agreement No 685872 (MOZART) and has been supported through the German Research Foundation (FG 2195-DFG SCHM2977) and the Friede Springer Stiftung.

**Acknowledgments:** We thank Sabine Stumpp (Julius Wolff Institut, Charité Universitätsmedizin Berlin) for assistance in the histological preparation of the hematoma samples. Moreover, we acknowledge the Open Access Publication Fund of the Charité – Universitätsmedizin Berlin, Germany.

**Conflicts of Interest:** The authors declare no conflict of interest.

## Abbreviations

| | |
|---|---|
| DPEC | Diethylpyrocarbonate water |
| *GAPDH* | Gylcerinaldehyde-3-phosphate dehydrogenase |
| *GLUT1* | Glucose transporter 1 |
| *HIF-1α* | Hypoxia-inducible factor-1α |
| *HMOX1* | Heme oxygenase-1 |
| H&E | Hematoxylin and eosin |

## References

1. Messonnier, L.; Kristensen, M.; Juel, C.; Denis, C. Importance of pH regulation and lactate/H+ transport capacity for work production during supramaximal exercise in humans. *J. Appl. Physiol.* **2007**, *102*, 1936–1944. [CrossRef] [PubMed]
2. Mekhail, K.; Gunaratnam, L.; Bonicalzi, M.-E.; Lee, S. HIF activation by pH-dependent nucleolar sequestration of VHL. *Nature* **2004**, *6*, 642–647. [CrossRef] [PubMed]
3. Sørensen, B.S.; Busk, M.; Overgaard, J.; Horsman, M.; Alsner, J. Simultaneous Hypoxia and Low Extracellular pH Suppress Overall Metabolic Rate and Protein Synthesis In Vitro. *PLoS ONE* **2015**, *10*, e0134955. [CrossRef] [PubMed]
4. King, T.C. Cell Injury, Cellular Responses to Injury, and Cell Death. In *Elsevier's Integrated Pathology*; Mosby Elsevier: Philadelphia, PA, USA, 2007; pp. 1–20.
5. Liberti, M.; Locasale, J.W. The Warburg Effect: How Does it Benefit Cancer Cells? *Trends Biochem. Sci.* **2016**, *41*, 211–218. [CrossRef]
6. Boidot, R.; Vegran, F.; Meulle, A.; Le Breton, A.; Dessy, C.; Sonveaux, P.; Lizard-Nacol, S.; Feron, O. Regulation of Monocarboxylate Transporter MCT1 Expression by p53 Mediates Inward and Outward Lactate Fluxes in Tumors. *Cancer Res.* **2011**, *72*, 939–948. [CrossRef]
7. Johnson, C.H.; Ivanisevic, J.; Siuzdak, G. Metabolomics: Beyond biomarkers and towards mechanisms. *Nat. Rev. Mol. Cell Boil.* **2016**, *17*, 451–459. [CrossRef]
8. Dargaville, T.; Farrugia, B.L.; Broadbent, J.A.; Pace, S.; Upton, Z.; Voelcker, N.H. Sensors and imaging for wound healing: A review. *Biosens. Bioelectron.* **2013**, *41*, 30–42. [CrossRef]
9. Gisbert-Garzarán, M.; Manzano, M.; Vallet-Regi, M. pH-Responsive Mesoporous Silica and Carbon Nanoparticles for Drug Delivery. *Bioengineering* **2017**, *4*, 3. [CrossRef]

10. Liu, N.; Yang, F.; Xiong, F.; Gu, N. The Smart Drug Delivery System and Its Clinical Potential. *Theranostics* **2016**, *6*, 1306–1323. [CrossRef] [PubMed]
11. Jiang, H.; Ochoa, M.; Waimin, J.F.; Rahimi, R.; Ziaie, B. A pH-regulated drug delivery dermal patch for targeting infected regions in chronic wounds. *Lab Chip* **2019**, *19*, 2265–2274. [CrossRef] [PubMed]
12. He, X.; Li, J.; An, S.; Jiang, C. pH-sensitive drug-delivery systems for tumor targeting. *Ther. Deliv.* **2013**, *4*, 1499–1510. [CrossRef] [PubMed]
13. Tang, H.; Zhao, W.; Yu, J.; Zhao, C. Recent Development of pH-Responsive Polymers for Cancer Nanomedicine. *Molecules* **2018**, *24*, 4. [CrossRef] [PubMed]
14. Goodman, A.D.; Lemann, J.; Lennon, E.J.; Relman, A.S. Production, Excretion, and Net Balance of Fixed Acid in Patients with Renal Acidosis. *J. Clin. Investig.* **1965**, *44*, 495–506. [CrossRef] [PubMed]
15. Lemann, J.; Litzow, J.R.; Lennon, E.J. The effects of chronic acid loads in normal man: Further evidence for the participation of bone mineral in the defense against chronic metabolic acidosis. *J. Clin. Investig.* **1966**, *45*, 1608–1614. [CrossRef]
16. Relman, A.S. The acidosis of renal disease. *Am. J. Med.* **1968**, *44*, 706–713. [CrossRef]
17. Arnett, T.R.; Dempster, D.W. Perspectives: Protons and osteoclasts. *J. Bone Miner. Res.* **2009**, *5*, 1099–1103. [CrossRef]
18. Arnett, T.R. Extracellular pH regulates bone cell function. *J. Nutr.* **2008**, *138*, 415S–418S. [CrossRef]
19. Green, J.; Yamaguchi, D.T.; Kleeman, C.R.; Muallem, S. Cytosolic pH regulation in osteoblasts. Regulation of anion exchange by intracellular pH and Ca2+ ions. *J. Gen. Physiol.* **1990**, *95*, 121–145. [CrossRef]
20. Kolar, P.; Schmidt-Bleek, K.; Schell, H.; Gaber, T.; Toben, D.; Schmidmaier, G.; Perka, C.; Buttgereit, F.; Duda, G.N. The Early Fracture Hematoma and Its Potential Role in Fracture Healing. *Tissue Eng. Part B Rev.* **2010**, *16*, 427–434. [CrossRef]
21. Schell, H.; Duda, G.N.; Peters, A.; Tsitsilonis, S.; Johnson, K.A.; Schmidt-Bleek, K. The haematoma and its role in bone healing. *J. Exp. Orthop.* **2017**, *4*, 5. [CrossRef]
22. Street, J.; Winter, D.; Wang, J.H.; Wakai, A.; McGuinness, A.; Redmond, H.P. Is human fracture hematoma inherently angiogenic? *Clin. Orthop. Relat. Res.* **2000**, *378*, 224–237. [CrossRef] [PubMed]
23. Chakkalakal, D.A.; Mashoof, A.A.; Novák, J.; Strates, B.S.; McGuire, M.H. Mineralization and pH relationships in healing skeletal defects grafted with demineralized bone matrix. *J. Biomed. Mater. Res.* **1994**, *28*, 1439–1443. [CrossRef] [PubMed]
24. Newman, R.J.; Duthie, R.B.; Francis, M.J.O. Nuclear Magnetic Resonance Studies of Fracture Repair. *Clin. Orthop. Relat. Res.* **1985**, *198*, 297–303. [CrossRef]
25. Schmidt-Bleek, K.; Schell, H.; Lienau, J.; Schulz, N.; Hoff, P.; Pfaff, M.; Schmidt, G.; Martin, C.; Perka, C.; Buttgereit, F.; et al. Initial immune reaction and angiogenesis in bone healing. *J. Tissue Eng. Regen. Med.* **2012**, *8*, 120–130. [CrossRef]
26. Schmidt-Bleek, K.; Schell, H.; Kolar, P.; Pfaff, M.; Perka, C.; Buttgereit, F.; Duda, G.N.; Lienau, J. Cellular composition of the initial fracture hematoma compared to a muscle hematoma: A study in sheep. *J. Orthop. Res.* **2009**, *27*, 1147–1151. [CrossRef]
27. Russell, W.M.S.; Burch, R.L. *The Principles of Humane Experimental Technique*; Methuen & Co, Ltd.: London, UK, 1959.
28. Grochot-Przeczek, A.; Kotlinowski, J.; Kozakowska, M.; Starowicz, K.; Jagodzinska, J.; Stachurska, A.; Volger, O.L.; Bukowska-Strakova, K.; Florczyk, U.; Tertil, M.; et al. Heme oxygenase-1 is required for angiogenic function of bone marrow-derived progenitor cells: Role in therapeutic revascularization. *Antioxid. Redox Signal.* **2014**, *20*, 1677–1692. [CrossRef]
29. Higashimura, Y.; Nakajima, Y.; Yamaji, R.; Harada, N.; Shibasaki, F.; Nakano, Y.; Inui, H. Up-regulation of glyceraldehyde-3-phosphate dehydrogenase gene expression by HIF-1 activity depending on Sp1 in hypoxic breast cancer cells. *Arch. Biochem. Biophys.* **2011**, *509*, 1–8. [CrossRef]
30. Yamaji, R.; Fujita, K.; Takahashi, S.; Yoneda, H.; Nagao, K.; Masuda, W.; Naito, M.; Tsuruo, T.; Miyatake, K.; Inui, H.; et al. Hypoxia up-regulates glyceraldehyde-3-phosphate dehydrogenase in mouse brain capillary endothelial cells: Involvement of Na+/Ca2+ exchanger. *Biochim. Biophys. Acta* **2003**, *1593*, 269–276. [CrossRef]
31. Schmidt-Bleek, K.; Petersen, A.; Dienelt, A.; Schwarz, C.; Duda, G.N. Initiation and early control of tissue regeneration—bone healing as a model system for tissue regeneration. *Expert Opin. Boil. Ther.* **2014**, *14*, 247–259. [CrossRef]

32. Löffler, J.; Sass, F.A.; Filter, S.; Rose, A.; Ellinghaus, A.; Duda, G.N.; Dienelt, A. Compromised Bone Healing in Aged Rats Is Associated with Impaired M2 Macrophage Function. *Front. Immunol.* **2019**, *10*, 2443. [CrossRef]
33. Khacho, M.; Tarabay, M.; Patten, D.; Khacho, P.; Maclaurin, J.G.; Guadagno, J.; Bergeron, R.; Cregan, S.P.; Harper, M.-E.; Park, D.S.; et al. Acidosis overrides oxygen deprivation to maintain mitochondrial function and cell survival. *Nat. Commun.* **2014**, *5*, 3550. [CrossRef] [PubMed]
34. Woo, Y.C.; Park, S.S.; Subieta, A.R.; Brennan, T. Changes in tissue pH and temperature after incision indicate acidosis may contribute to postoperative pain. *Anesthesiol.* **2004**, *101*, 468–475. [CrossRef] [PubMed]
35. Nicoll, R.; Howard, J. The acid—Ash hypothesis revisited: A reassessment of the impact of dietary acidity on bone. *J. Bone Miner. Metab.* **2014**, *32*, 469–475. [CrossRef] [PubMed]
36. Newman, R.J.; Francis, M.J.O.; Duthie, R.B. Nuclear Magnetic Resonance Studies of Experimentally Induced Delayed Fracture Union. *Clin. Orthop. Relat. Res.* **1987**, *216*, 253–261. [CrossRef]
37. Wu, R.; Racker, E. Regulatory mechanisms in carbohydrate metabolism. IV. Pasteur effect and Crabtree effect in ascites tumor cells. *J. Boil. Chem.* **1959**, *234*, 1036–1041.
38. Payen, V.L.; Brisson, L.; Dewhirst, M.W.; Sonveaux, P. Common Responses of Tumors and Wounds to Hypoxia. *Cancer J.* **2015**, *21*, 75–87. [CrossRef]
39. Martínez-Reyes, I.; Chandel, N.S. Mitochondrial TCA cycle metabolites control physiology and disease. *Nat. Commun.* **2020**, *11*, 102–111. [CrossRef]
40. Oyedotun, K.S.; Lemire, B.D. The Quaternary Structure of the Saccharomyces cerevisiae Succinate Dehydrogenase: Homology modeling, cofactor docking, and molecular dynamics simulation studies. *J. Boil. Chem.* **2003**, *279*, 9424–9431. [CrossRef]
41. Chu, L.; Gao, H.; Cheng, T.; Zhang, Y.; Liu, J.; Huang, F.; Yang, C.; Shi, L.; Liu, J. A charge-adaptive nanosystem for prolonged and enhanced in vivo antibiotic delivery. *Chem. Commun.* **2016**, *52*, 6265–6268. [CrossRef]
42. Einhorn, T.A.; Lane, J.M. Significant advances have been made in the way surgeons treat fractures. *Clin. Orthop. Relat. Res.* **1998**, *335*, 2–3. [CrossRef]
43. Haas, N.P. Callus modulation–fiction or reality? *Der Chir.* **2000**, *71*, 987–988. [CrossRef] [PubMed]
44. United States Bone and Joint Initiative. *The Burden of Musculoskeletal Diseases in the United States*, 3rd ed.; United States Bone and Joint Initiative: Rosemont, IL, USA, 2014.
45. *Ageing and Health.* World Health Organization. 2018. Available online: https://www.who.int/news-room/fact-sheets/detail/ageing-and-health (accessed on 6 January 2020).
46. Manini, T.M. Development of physical disability in older adults. *Curr. Aging Sci.* **2011**, *4*, 184–191. [CrossRef] [PubMed]
47. Gruber, R.; Koch, H.; Doll, B.A.; Tegtmeier, F.; Einhorn, T.; Hollinger, J.O. Fracture healing in the elderly patient. *Exp. Gerontol.* **2006**, *41*, 1080–1093. [CrossRef] [PubMed]
48. Frassetto, L.; Morris, R.C.; Sellmeyer, D.E.; Todd, K.; Sebastian, A. Diet, evolution and aging–the pathophysiologic effects of the post-agricultural inversion of the potassium-to-sodium and base-to-chloride ratios in the human diet. *Eur. J. Nutr.* **2001**, *40*, 200–213. [CrossRef]
49. Frassetto, L.; Sebastian, A. How metabolic acidosis and oxidative stress alone and interacting may increase the risk of fracture in diabetic subjects. *Med. Hypotheses* **2012**, *79*, 189–192. [CrossRef]
50. Gupta, A.; Atoria, C.L.; Ehdaie, B.; Shariat, S.F.; Rabbani, F.; Herr, H.W.; Bochner, B.H.; Elkin, E.B. Risk of Fracture After Radical Cystectomy and Urinary Diversion for Bladder Cancer. *J. Clin. Oncol.* **2014**, *32*, 3291–3298. [CrossRef]
51. Kato, A.; Kido, R.; Onishi, Y.; Kurita, N.; Fukagawa, M.; Akizawa, T.; Fukuhara, S. Association of Serum Bicarbonate with Bone Fractures in Hemodialysis Patients: The Mineral and Bone Disorder Outcomes Study for Japanese CKD Stage 5D Patients (MBD-5D). *Nephron Clin. Pr.* **2014**, *128*, 79–87. [CrossRef]
52. Starke, A.; Corsenca, A.; Kohler, T.; Knubben, J.; Kraenzlin, M.; Uebelhart, D.; Wüthrich, R.P.; Von Rechenberg, B.; Müller, R.; Ambühl, P.M. Correction of Metabolic Acidosis with Potassium Citrate in Renal Transplant Patients and its Effect on Bone Quality. *Clin. J. Am. Soc. Nephrol.* **2012**, *7*, 1461–1472. [CrossRef]
53. Tabatabai, L.S.; Cummings, S.R.; Tylavsky, F.A.; Bauer, D.C.; Cauley, J.A.; Kritchevsky, S.B.; Newman, A.B.; Simonsick, E.M.; Harris, T.B.; Sebastián, A.; et al. Arterialized venous bicarbonate is associated with lower bone mineral density and an increased rate of bone loss in older men and women. *J. Clin. Endocrinol. Metab.* **2015**, *100*, 1343–1349. [CrossRef]

54. Preininger, B.; Gerigk, H.; Bruckner, J.; Perka, C.; Schell, H.; Ellinghaus, A.; Schmidt-Bleek, K.; Duda, G. An experimental setup to evaluate innovative therapy options for the enhancement of bone healing using BMP as a benchmark—A pilot study. *Eur. Cells Mater.* **2012**, *23*, 262–272. [CrossRef]
55. Lu, C.; Hansen, E.; Sapozhnikova, A.; Hu, D.; Miclau, T.; Marcucio, R.S. Effect of age on vascularization during fracture repair. *J. Orthop. Res.* **2008**, *26*, 1384–1389. [CrossRef] [PubMed]
56. Hankenson, K.D.; Dishowitz, M.; Gray, C.; Schenker, M. Angiogenesis in bone regeneration. *Injury* **2011**, *42*, 556–561. [CrossRef] [PubMed]
57. Lähteenvuo, J.; Rosenzweig, A. Effects of aging on angiogenesis. *Circ. Res.* **2012**, *110*, 1252–1264. [CrossRef]
58. *Optical pH Sensors & Meters*, version pH-18-01; PreSens Precision Sensing GmbH: Regensburg, Germany, 2018.
59. Huber, C.; Klimant, I.; Krause, C.; Werner, T.; Mayr, T.; Wolfbeis, O.S. Optical sensor for seawater salinity. *Anal. Bioanal. Chem.* **2001**, *368*, 196–202. [CrossRef]
60. Liebsch, G.; Klimant, I.; Krause, C.; Wolfbeis, O.S. Fluorescent imaging of pH with optical sensors using time domain dual lifetime referencing. *Anal. Chem.* **2001**, *73*, 4354–4363. [CrossRef] [PubMed]
61. Beck-Broichsitter, B.E.; Christofzik, D.; Daschner, F.; Knöchel, R.; Smeets, R.; Warnke, P.; Wiltfang, J.; Becker, S.T. Endocultivation: Metabolism During Heterotopic OsteoinductionIn Vivo—Monitoring with Fiber Optic Detection Devices. *Tissue Eng. Part C Methods* **2012**, *18*, 740–746. [CrossRef]
62. Jonitz, A.; Lochner, K.; Lindner, T.; Hansmann, D.; Marrot, A.; Bader, R. Oxygen consumption, acidification and migration capacity of human primary osteoblasts within a three-dimensional tantalum scaffold. *J. Mater. Sci. Mater. Electron.* **2011**, *22*, 2089–2095. [CrossRef]
63. Jirkof, P.; Durst, M.; Klopfleisch, R.; Palme, R.; Thöne-Reineke, C.; Buttgereit, F.; Schmidt-Bleek, K.; Lang, A. Administration of Tramadol or Buprenorphine via the drinking water for post-operative analgesia in a mouse-osteotomy model. *Sci. Rep.* **2019**, *9*, 10749. [CrossRef]
64. Schindelin, J.; Arganda-Carreras, I.; Frise, E.; Kaynig, V.; Longair, M.; Pietzsch, T.; Preibisch, S.; Rueden, C.; Saalfeld, S.; Schmid, B.; et al. Fiji: An open-source platform for biological-image analysis. *Nat. Methods* **2012**, *9*, 676–682. [CrossRef]
65. Giavalisco, P.; Köhl, K.; Hummel, J.; Seiwert, B.; Willmitzer, L. 13C Isotope-Labeled Metabolomes Allowing for Improved Compound Annotation and Relative Quantification in Liquid Chromatography-Mass Spectrometry-based Metabolomic Research. *Anal. Chem.* **2009**, *81*, 6546–6551. [CrossRef]

**Publication 3: 'Hybrid injectable sol-gel systems based on thermo-sensitive polyurethane hydrogels carrying pH-sensitive mesoporous silica nanoparticles for the controlled and triggered release of therapeutic agents'**

Monica Boffito, Alessandro Torchio, Chiara Tonda-Turo, Rossella Laurano, Miguel Gisbert-Garzarán, Julia C. Berkmann, Claudio Cassino, Miguel Manzano, Georg N. Duda, María Vallet-Regí, Katharina Schmidt-Bleek and Gianluca Ciardelli, *Hybrid injectable sol-gel systems based on thermo-sensitive*
*polyurethane hydrogels carrying pH-sensitive mesoporous silica nanoparticles for the controlled and triggered release of therapeutic agents*, Frontiers in Bioengineering and Biotechnology, 2020

Journal Data Filtered By: **Selected JCR Year: 2018** Selected Editions: SCIE,SSCI Selected Categories: **"MULTIDISCIPLINARY SCIENCES"** Selected Category Scheme: WoS
**Gesamtanzahl: 69 Journale**

| Rank | Full Journal Title | Total Cites | Journal Impact Factor | Eigenfactor Score |
|---|---|---|---|---|
| 1 | NATURE | 745,692 | 43.070 | 1.285010 |
| 2 | SCIENCE | 680,994 | 41.037 | 1.070190 |
| 3 | National Science Review | 1,842 | 13.222 | 0.006500 |
| 4 | Science Advances | 21,901 | 12.804 | 0.110010 |
| 5 | Nature Communications | 243,793 | 11.878 | 1.103290 |
| 6 | Nature Human Behaviour | 1,230 | 10.575 | 0.006550 |
| 7 | PROCEEDINGS OF THE NATIONAL ACADEMY OF SCIENCES OF THE UNITED STATES OF AMERICA | 661,118 | 9.580 | 1.022190 |
| 8 | Science Bulletin | 3,569 | 6.277 | 0.009840 |
| 9 | Scientific Data | 3,240 | 5.929 | 0.015610 |
| 10 | Frontiers in Bioengineering and Biotechnology | 1,994 | 5.122 | 0.006540 |

frontiers in Bioengineering and Biotechnology

ORIGINAL RESEARCH
published: 19 May 2020
doi: 10.3389/fbioe.2020.00384

# Hybrid Injectable Sol-Gel Systems Based on Thermo-Sensitive Polyurethane Hydrogels Carrying pH-Sensitive Mesoporous Silica Nanoparticles for the Controlled and Triggered Release of Therapeutic Agents

*Monica Boffito[1]*, Alessandro Torchio[1,2], Chiara Tonda-Turo[1], Rossella Laurano[1,2], Miguel Gisbert-Garzarán[3,4], Julia C. Berkmann[5], Claudio Cassino[6], Miguel Manzano[3,4], Georg N. Duda[5,7], María Vallet-Regí[3,4], Katharina Schmidt-Bleek[5,7] and Gianluca Ciardelli[1]*

[1] Department of Mechanical and Aerospace Engineering, Politecnico di Torino, Turin, Italy, [2] Department of Surgical Sciences, Università degli Studi di Torino, Turin, Italy, [3] Departamento de Química en Ciencias Farmacéuticas, Instituto de Investigación Sanitaria del Hospital, Universidad Complutense de Madrid, Madrid, Spain, [4] CIBER de Bioingeniería, Biomateriales y Nanomedicina (CIBER-BBN), Madrid, Spain, [5] Julius Wolff Institut, Charité - Universitätsmedizin Berlin, Berlin, Germany, [6] Department of Science and Technological Innovation, Università del Piemonte Orientale, Alessandria, Italy, [7] BIH Center for Regenerative Therapies, Charité - Universitätsmedizin Berlin, Berlin, Germany

OPEN ACCESS

**Edited by:**
*Maria Chatzinikolaidou, University of Crete, Greece*

**Reviewed by:**
*Xin Zhao, Hong Kong Polytechnic University, Hong Kong*
*Tzu-Wei Wang, National Tsing Hua University, Taiwan*

***Correspondence:**
*Monica Boffito*
*monica.boffito@polito.it*

**Specialty section:**
*This article was submitted to Tissue Engineering and Regenerative Medicine, a section of the journal Frontiers in Bioengineering and Biotechnology*

**Received:** *15 February 2020*
**Accepted:** *07 April 2020*
**Published:** *19 May 2020*

**Citation:**
*Boffito M, Torchio A, Tonda-Turo C, Laurano R, Gisbert-Garzarán M, Berkmann JC, Cassino C, Manzano M, Duda GN, Vallet-Regí M, Schmidt-Bleek K and Ciardelli G (2020) Hybrid Injectable Sol-Gel Systems Based on Thermo-Sensitive Polyurethane Hydrogels Carrying pH-Sensitive Mesoporous Silica Nanoparticles for the Controlled and Triggered Release of Therapeutic Agents. Front. Bioeng. Biotechnol. 8:384. doi: 10.3389/fbioe.2020.00384*

Injectable therapeutic formulations locally releasing their cargo with tunable kinetics in response to external biochemical/physical cues are gaining interest in the scientific community, with the aim to overcome the cons of traditional administration routes. In this work, we proposed an alternative solution to this challenging goal by combining thermo-sensitive hydrogels based on custom-made amphiphilic poly(ether urethane)s (PEUs) and mesoporous silica nanoparticles coated with a self-immolative polymer sensitive to acid pH (MSN-CS-SIP). By exploiting PEU chemical versatility, Boc-protected amino groups were introduced as PEU building block (PEU-Boc), which were then subjected to a deprotection reaction to expose pendant primary amines along the polymer backbone (PEU-$NH_2$, 3E18 -$NH_2$/$g_{PEU\text{-}NH2}$) with the aim to accelerate system response to external acid pH environment. Then, thermo-sensitive hydrogels were designed (15% w/v) showing fast gelation in physiological conditions (approximately 5 min), while no significant changes in gelation temperature and kinetics were induced by the Boc-deprotection. Conversely, free amines in PEU-$NH_2$ effectively enhanced and accelerated acid pH transfer (pH 5) through hydrogel thickness (PEU-Boc and PEU-$NH_2$ gels covered approximately 42 and 52% of the pH delta between their initial pH and the pH of the surrounding buffer within 30 min incubation, respectively). MSN-CS-SIP carrying a fluorescent cargo as model drug (MSN-CS-SIP-Ru) were then encapsulated within the hydrogels with no significant effects on their thermo-sensitivity. Injectability and *in situ* gelation at 37°C were demonstrated *ex vivo* through sub-cutaneous injection

in rodents. Moreover, MSN-CS-SIP-Ru-loaded gels turned out to be detectable through the skin by IVIS imaging. Cargo acid pH-triggered delivery from PEU-Boc and PEU-$NH_2$ gels was finally demonstrated through drug release tests in neutral and acid pH environments (in acid pH environment approximately 2-fold higher cargo release). Additionally, acid-triggered payload release from PEU-$NH_2$ gels was significantly higher compared to PEU-Boc systems at 3 and 4 days incubation. The herein designed hybrid injectable formulations could thus represent a significant step forward in the development of multi-stimuli sensitive drug carriers. Indeed, being able to adapt their behavior in response to biochemical cues from the surrounding physio-pathological environment, these formulations can effectively trigger the release of their payload according to therapeutic needs.

**Keywords: thermo-sensitive hydrogels, polyurethane, pH-sensitive mesoporous silica nanoparticles, self-immolative polymer, triggered drug release, stimuli-responsive**

## INTRODUCTION

The design of injectable therapeutic formulations locally releasing their cargo with controlled and prolonged kinetics is becoming an urgent need in the biomedical field. Indeed, such an approach is expected to open a new chapter in the treatment of pathological states, with the huge potential to progressively overcome the typical drawbacks of gold standard administration approaches (e.g., need to repeatedly administer high drug dosages, undesired side effects, drug accumulation in non-target tissues and organs). Additionally, a proper engineering of newly designed injectable formulations could eventually lead to an in depth control over their properties, thus allowing the achievement of the best delivery profiles ensuring the cargo to be released within the therapeutic window in the target tissue for the required time interval. Among the potential approaches under investigation in the scientific community, the design of hydrogels for drug release applications is gaining huge interest, with an increasing number of research works on this topic published annually (a 10–15% annual increase has been registered over the last 10 years, PubMed's database). In their general definition, hydrogels are three-dimensional cross-linked networks able to absorb a remarkable amount of water/physiological fluids from the surrounding environment and characterized by a soft consistence, which makes them similar to living soft tissues (Ahmed, 2015; Ozcelik, 2016). Among the wide variety of available hydrogels, thermo-sensitive sol-gel systems that undergo a temperature-driven gelation with increasing temperature up to the physiological value represent a promising alternative as drug delivery systems (Boffito et al., 2014). Indeed, they are easily injectable in the sol/semi-gel state and perfectly take the shape of the defect cavity prior to complete gelation. Additionally, they can be easily loaded with therapeutic agents, which are then locally released over time in a sustained and controlled way. Interestingly, in the case of thermo-sensitive hydrogels based on amphiphilic polymers, both hydrophilic and hydrophobic drugs can be easily encapsulated at high concentration by exploiting the arrangement of the polymeric chains into micelles, which are also the driving-force for system transition from the sol to the gel state (Xi et al., 2014; Boffito et al., 2016, 2019a,b; Anggelia et al., 2019). Payload release from thermo-sensitive hydrogels is usually driven by passive diffusion, swelling/erosion or the co-presence of both diffusion and swelling/erosion phenomena (Huang et al., 2019). A further tuning of payload release kinetics and mechanism can be obtained by pre-loading therapeutic agents into nano- or micro-carriers, such as mesoporous silica or polymeric particles. For instance, Geng et al. (2011) incorporated vascular endothelial growth factor (VEGF)-loaded poly(lactic-*co*-glycolic acid) particles into Pluronic F127-based hydrogels for application in bladder reconstruction. Later, a similar approach was adopted by Chen et al. (2018) that reported the incorporation of VEGF-loaded polymeric microspheres into injectable thermo-sensitive hydrogels based on a star-shaped poly(D,L-lactic-*co*-glycolic acid)-*b*-methoxy poly(ethylene glycol) (PLGA-mPEG) block copolymer, demonstrating the capability of the gels to delay VEGF release from the particles. Pontremoli et al. (2018) reported the development of hybrid sol-gel systems based on a custom-made poly(ether urethane) (PEU) containing F127 as building block and ion-doped bioactive glasses (MBGs) in the form of nanoparticles or microspheres, demonstrating that the resulting composite formulations allowed a prolonged and sustained release of copper ions over time. Later, the same authors described similar injectable formulations co-releasing copper ions and ibuprofen (Boffito et al., 2019b). Interestingly, they demonstrated that drugs could be released from hybrid formulations with an anomalous mechanism resulting from the existence of a double diffusive barrier (i.e., the hydrogel and the mesoporous framework) the drug molecules must pass through before being released in the surrounding aqueous medium. On the other hand, in the case of therapeutic ion release, different mechanisms turned out to be involved in the progressive delivery of ion species, i.e., ion exchange reactions within the MBG framework followed by diffusion through the hydrogel network.

Additional control over payload release can be reached by providing the designed systems with the capability to respond to physical and/or biochemical cues from the surrounding

environment, thus making it possible to finely modulate and trigger the release of encapsulated therapeutics. For instance, reactive oxygen species (ROS)-dependent drug release was reported by Gupta et al. (2014) from thermo-sensitive hydrogels based on a ABC triblock polymer containing a ROS-sensitive poly(propylene sulfide) building block. Near-infrared (NIR) light-induced drug delivery was achieved by embedding gold nanorods into thermo-sensitive poly(N-isopropylacrylamide) (PNIPAM) hydrogels which underwent shrinkage upon local heating of the nanorods due to NIR light irradiation, resulting in the triggered release of encapsulated drugs (Jiang et al., 2019). Carbon nanotubes were also used with the same goal by Dong et al. (2017) that exploited their photo-thermal effect to trigger the release of doxorubicin from thermo-sensitive hydrogels based on a poly(ε-caprolactone)-*b*-poly(ethylene glycol)-*b*-poly(ε-caprolactone) (PCL-PEG-PCL) triblock copolymer. However, differently from the former approach, triggered release was achieved in this case by exploiting a gel-to-sol transition occurring within the hydrogels in response to local heating induced by NIR light application. Another widely explored stimulus to achieve a triggered drug release *in situ* exploits pH variations. The design of drug delivery systems able to respond to specific pH values, thus accelerating the release of their payload in well-defined conditions, could effectively represent a successful strategy in the treatment of all pathological conditions characterized by pH changes in the surrounding milieu [e.g., tumor and chronic skin wound environments are characterized by acid and alkaline pH, respectively (Kanamala et al., 2016; Bullock et al., 2019)]. The goal of triggering payload release in response to external pH is usually achieved by chemically modifying hydrogel-forming polymers. For instance, Guar gum was block copolymerized with PNIPAM by Lang et al. (2006) to provide thermo-sensitive PNIPAM-based hydrogels with additional pH-sensitivity (slower release of sinomenine hydrochloride at pH 6.8 compared to pH 1.0). More recently, N-isopropylacrylamide (NIPAM), itaconamic acid (AIM) and β-cyclodextrin (β-CD) were copolymerized to get a polymer which aqueous solutions showed responsiveness to temperature and pH provided by NIPAM and AIM, respectively, and additional capability to encapsulate drug molecules due to β-CD moieties (Rwei et al., 2016). Similar results were also published by Roy et al. (2019) that developed pH- and thermo-responsive gels by grafting and crosslinking PNIPAM and poly(methacrylic acid) on β-cyclodextrins for preferential release of metronidazole and ofloxacin at colonic pH (i.e., 7.4) instead of stomach pH (acid pH). As an alternative to this approach, pH-sensitive release of a cargo can be also achieved by blending hydrogel-forming materials with pH-sensitive polymers. For instance, Zhang et al. (2018) developed injectable hydrogels modulating doxorubicin release in response to external pH (i.e., faster release in acid pH environment) by mixing chitosan, hyaluronic acid and β-sodium glycerophosphate. Later, a similar approach was adopted by Chatterjee et al. (2019) that recently reported the design of dual-responsive (pH and temperature) hydrogels by blending F127, N,N,N-trimethyl chitosan and polyethylene glycolated hyaluronic acid. In the same year, tissue adhesive and acid pH-responsive hydrogels were designed starting from chitosan-grafted-dihydrocaffeic acid and oxidized pullulan that underwent chemical crosslinking via a Schiff base reaction upon mixing (Liang et al., 2019).

Finally, as a last approach to design pH-sensitive drug-releasing gels, composite formulations combining cargo-loaded particles within a hydrogel vehicle phase have been also described in literature. For instance, Wang et al. (2010) encapsulated molecularly imprinted pH-sensitive nanospheres loaded with dexamethasone-21 phosphate disodium into UV-crosslinked gels as potential coating of implantable biosensors. In the same year, chitosan/poly-γ-glutamic acid nanoparticles loaded with amoxicillin were incorporated into pH-sensitive alginate-based hydrogels (Chang et al., 2010). Later, triggered camptothecin (CPT) release at mild acid pH values was achieved by loading CPT-containing nanoparticles based on an acid-sensitive β-cyclodextrin derivative (i.e., acetalated-β-cyclodextrin) into supramolecular hydrogels prepared starting from graphene oxide and poly(vinyl alcohol) (Ye and Hu, 2016). Lastly, Qindeel et al. (2019) described hybrid formulations for transdermal drug delivery resulting from the encapsulation of pH-sensitive nanoparticles into Carbopol 934-based hydrogels.

Within this constantly evolving scenario, in the present work we proposed an alternative approach to design injectable therapeutical formulations showing concurrent temperature- and pH-sensitivity, which allow easy injection and gelation under mild conditions and triggered payload release, respectively. In detail, this goal was achieved by combining the thermo-sensitivity of a custom-made amphiphilic poly(ether urethane) and the pH responsiveness of mesoporous silica nanoparticles (MSNs), which pore openings have been plugged by a self-immolative polymer (SIP) sensitive to acid pH (MSN-CS-SIP). Furthermore, to accelerate system response to pH changes, thus making acid pH transmission from the surrounding environment through hydrogel thickness faster, the wide versatility of polyurethane chemistry was exploited to introduce pendant primary amines along PEU backbone. In detail, the PEU used in this work was synthesized by chain extending Poloxamer® 407 with an aliphatic non-toxic diisocyanate and an amino-acid derived diol containing Boc-protected amino-groups (NHP407). Then, amino group exposure along PEU backbone (SHP407) resulted from the optimization of the Boc deprotection procedure in terms of chloroform/trifluoroacetic acid volume ratio. The successful synthesis of NHP407 and SHP407 was demonstrated by Size Exclusion Chromatography (SEC), Fourier Transformed Infrared (FTIR) Spectroscopy, Proton Nuclear Magnetic Resonance ($^1$H NMR) Spectroscopy and Orange II Sodium Salt colorimetric assay. Then, thermo-sensitive hydrogels were designed by solubilizing the PEUs in aqueous media and their gelation was qualitatively and quantitatively characterized by tube inverting and rheological tests. The capability of the hydrogels to transmit the pH of the surrounding environment through their thickness was studied by means of contact tests with buffer solutions at different pH values (pH 5 and 7.4). Finally, MSN-CS-SIP were embedded within the hydrogels and the effect of particle encapsulation on the temperature-driven sol-to-gel transition of the hybrid formulations was investigated through rheology. SIP-coated MSNs carrying a fluorescent cargo

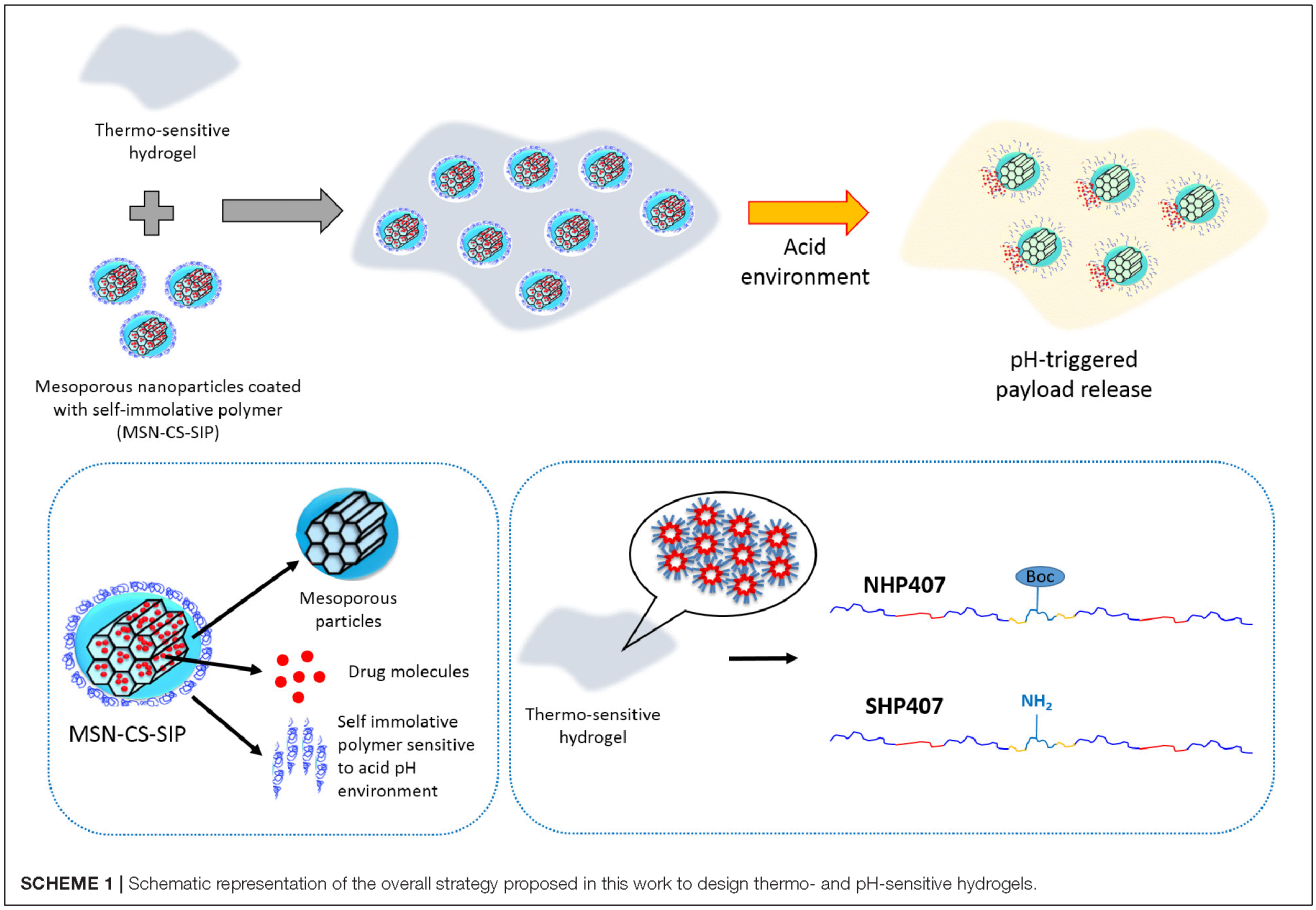


**SCHEME 1** | Schematic representation of the overall strategy proposed in this work to design thermo- and pH-sensitive hydrogels.

as model drug were then encapsulated within the hydrogels and its pH-triggered release was investigated by incubating the gels in neutral and acid pH media. Injectability and *in situ* dispersion and gelation were finally assessed *ex vivo* through subcutaneous injection in rodents. **Scheme 1** summarizes the overall strategy we adopted to design the thermo- and pH-sensitive gels described in this work.

## MATERIALS AND METHODS

### Polymer Synthesis and Characterization

#### Materials

The building blocks used for PEU synthesis, i.e., Poloxamer® 407 (P407, poly(ethylene oxide)-poly(propylene oxide)-poly(ethylene oxide), PEO-PPO-PEO, $\overline{M}_n$ 12600 Da, 70% w/w PEO), 1,6-hexamethylene diisocyanate (HDI) and N-Boc serinol were purchased from Sigma Aldrich, Italy. Before use, they were treated to remove residual moisture and stabilizers. Briefly, P407 was dried under reduced pressure at 100°C for 8 h and then cooled down to 30°C under vacuum, N-Boc serinol was dried at room temperature (RT) under vacuum in a dessicator, HDI was distilled under reduced pressure and stored in a dessicator until use. Butynorate was purchased from Sigma Aldrich, Italy and used as received. All solvents were purchased from Carlo Erba Reagents, Italy in the analytical grade and used as received with the exception of 1,2-dichloroethane (DCE) which was anhydrified over activated molecular sieves (3 Å, Sigma Aldrich, Italy, activation at 120°C, atmospheric pressure, overnight) at RT and under nitrogen flow for 8 h. All required glassware for PEU synthesis was dried overnight at 120°C.

#### Poly(ether urethane) Synthesis

The poly(ether urethane) used in this work was synthesized according to Boffito et al. (2016). Briefly, the synthesis was carried out in solution (i.e., anhydrous DCE) under nitrogen flow through a pre-polymerization approach. Initially, P407 was solubilized in anhydrous DCE (20% w/v) and equilibrated at 80°C. Then, HDI (2:1 molar ratio with respect to P407) and butynorate (0.1% w/w with respect to P407) were added to the P407 solution and the prepolymerization step started. After 150 min, the temperature of the reaction mixture was lowered to 60°C, N-Boc serinol was added (3% w/v in anhydrous DCE) and the chain extension reaction was carried on for 90 min. Finally, upon temperature decrease to RT and passivation of residual isocyanate groups with MeOH, the synthesized PEU was collected by precipitation in excess petroleum ether (4:1 volume ratio with respect to DCE). PEU was then purified by precipitating its solution (30% w/v in DCE) in a mixture of diethyl ether and MeOH (98:2 v/v, 5:1 volume ratio with respect

to DCE). The polymer was finally collected by centrifugation (Hettich, MIKRO 220R, 6000 rpm, 0°C, 20 min), dried overnight under the fume hood and stored at 4°C under nitrogen until use.

Hereafter, the as-synthesized PEU will be referred to with the acronym NHP407, where N, H and P407 identify the chain extender, the diisocyanate and the macrodiol used for its synthesis, respectively.

### Exposure of Free Amines Along Poly(ether urethane) Backbone

The selection of N-Boc serinol as PEU building block allowed the exposure of free amines along its backbone through a Boc-deprotection reaction. According to the protocols usually adopted in peptide synthesis reactions to deprotect Boc-protected amines of amino acids, the deprotection reaction was carried out in acid conditions (Blondelle and Houghten, 1993). Briefly, 10 g of NHP407 were solubilized in 225 ml of chloroform ($CHCl_3$) at RT for 120 min (under stirring at 250 rpm) and then 25 ml of trifluoroacetic acid (TFA) were added to the solution and the mixture (overall 4% w/v polymer concentration, $CHCl_3$/TFA 90/10 volume ratio) was left to react for 60 min at RT. At the end of the deprotection reaction, solvents were evaporated under vacuum using a rotary evaporator (Buchi Rotavapor Labortechnik AG) and the collected polymer was washed twice using chloroform (10% w/v) to completely evaporate TFA residues. Finally, the polymer was solubilized in distilled water (5% w/v) at 4°C overnight and dialyzed (cellulose membrane cut-off 10–12 kDa, Sigma Aldrich, Italy) against distilled water for 2 days (water refresh three times/day) to completely wash out Boc groups and residual $CHCl_3$ and TFA molecules. Deprotected polymer was then freeze dried (Martin Christ ALPHA 2–4 LSC) and stored under vacuum at 4°C until use. This deprotection protocol resulted from an optimization process, which is thoroughly described in **Supplementary Material**.

Hereafter, the collected polymer after the Boc-deprotection reaction will be referred to with the acronym SHP407.

### Attenuated Total Reflectance Fourier Transform Infrared Spectroscopy

Attenuated Total Reflectance Fourier Transform Infrared (ATR-FTIR) spectroscopic analyses were performed to (i) assess the success of NHP407 synthesis, and (ii) verify the absence of degradation and $CHCl_3$/TFA residues in SHP407. ATR-FTIR spectra resulted from 16 scans registered at RT within the spectral range 6000–400 $cm^{-1}$ (resolution 4 $cm^{-1}$) using a Perkin Elmer Spectrum 100 instrument equipped with an ATR accessory with diamond crystal (UART KRS5). Spectra analysis and peak identification were conducted using the Perkin Elmer Spectrum software.

### Size Exclusion Chromatography

Number Average and Weight Average Molecular Weights ($\overline{M}_n$ and $\overline{M}_w$, respectively) and Polydispersity Index (D) of NHP407 and SHP407 samples were estimated using an Agilent Technologies 1200 Series (USA) instrument equipped with a Refractive Index detector (RID) and two Waters Styragel columns (HR2 and HR4). Analyses were conducted using tetrahydrofuran (THF, inhibitor-free, CHROMASOLV® Plus, for HPLC, ≥99.9%, Sigma Aldrich, Italy) as eluent at 35°C and 0.4 ml/min flow rate. SEC samples were prepared by filtering a polymer solution (2 mg/ml in THF) through a 0.45 μm syringe filter (Whatman). Registered RID signals as a function of elution time were then analyzed using Excel software (Microsoft Corporation) to estimate $\overline{M}_n$, $\overline{M}_w$, and D relative to a calibration curve based on polystyrene standards ($\overline{M}_n$ within the range 740–180,000 Da).

### Proton Nuclear Magnetic Resonance Spectroscopy

Proton Nuclear Magnetic Resonance spectra of NHP407 and SHP407 samples were recorded in anhydrous deuterated dimethyl sulfoxide (DMSO-d6, 99.8% D with 0.03% TMS, Sigma Aldrich, Italy) by means of an Avance III Bruker spectrometer equipped with a 11.74 T superconducting magnet (500 MHz $^1H$ Larmor frequency), a Bruker BBFO direct probe and a Bruker BVT 3000 unit for temperature control. The spectra were registered at 25°C and resulted from 12 scans, with 10 s relaxation time. $^1H$ NMR spectra were referenced to TMS signal at 0 ppm.

### Quantification of Exposed Amines Through Orange II Sodium Salt Colorimetric Assay

Primary amines exposed along polymer backbone upon Boc-removal were quantified according to the method recently published by Laurano et al. (2020) that adapted to water-soluble polymers the protocol usually used to quantify amino groups exposed on polymer surfaces (Noel et al., 2011). Briefly, the polymer was dissolved (0.04% w/v) in an Orange II Sodium Salt (Sigma Aldrich, Italy) aqueous solution (0.175 mg/ml in double distilled water, $ddH_2O$) previously adjusted at pH 3 and then the resulting solutions were incubated for 18 h at RT, in the dark. Samples were then dialyzed against $ddH_2O$ (Sigma Aldrich, Italy, cellulose membrane cut-off 10–12 kDa) to wash out uncoupled dye molecules and freeze dried (Martin Christ ALPHA 2–4 LSC). Lastly, dye molecules were desorbed from lyophilized samples by solubilizing them in $ddH_2O$ previously adjusted at pH 12 (1% w/v) for 2 h at RT, in the dark. Finally, after centrifugation (15°C, 6000 rpm, 10 min), the samples were analyzed using an UV–Vis spectrophotometer (PerkinElmer, Lambda 25) within the spectral range from 700 to 400 nm, being Orange characteristic peak at 485 nm. Exposed amines were then quantified referring to a calibration curve based on Orange-containing standards (1.75–29.2 μg/ml concentration) prepared in $ddH_2O$ at pH 12.

## Hydrogel Design and Characterization

### Hydrogel Preparation Protocol

In order to obtain thermo-sensitive sol-gel systems, NHP407 and SHP407 were dissolved at a previously optimized concentration of 15% w/v (Boffito et al., 2016). Polymer solubilization was carried out at 5°C overnight using a mix of physiological solution (0.9% NaCl), phosphate buffer at pH 8 and phosphate buffered saline (PBS, pH 7.4) at 80/10/10 volume ratio. This mixture of buffered and not-buffered aqueous solutions was selected to make the developed sol-gel systems able to more easily transport acid pH from the surrounding environment (pH 5) to their core, while forcing initial hydrogel pH toward a neutral value. In order to

allow comparison among the samples and avoid results variance due to sample geometry and volume, all hydrogels (1 ml) were prepared in Bijou sample containers (Savatec, Italy, polystyrene vials with 17 mm inner diameter).

### Tube Inverting Test

Hydrogel gelation potential was first qualitatively assessed by tube inverting test, which was performed in temperature ramp mode and in isothermal conditions at 37°C to estimate Lower Critical Gelation Temperature (LCGT) values and gelation time in physiological conditions, respectively. Briefly, LCGT values were estimated by progressively increasing hydrogel temperature from 4 to 70°C at 1°C/step, each step consisting in sample equilibration at the predefined temperature for 5 min followed by vial inversion for 30 s. At each step, "sol," "semi-gel," and "gel" states were defined by observing the presence of flow during the 30 s of vial inversion. Gelation time in physiological conditions was estimated by keeping the temperature constant at 37°C and inverting the vials after predefined time intervals of incubation at that temperature (i.e., from 1 to 10 min, 1 min/step). Conditions of "sol," "semi-gel," and "gel" were defined through vial inversion for 30 s.

### Rheological Characterization

To better characterize hydrogel transition from the sol to the gel state, rheological characterization was performed through strain sweep, frequency sweep and temperature ramp tests. Strain sweep tests were conducted at 37°C and constant frequency (10 Hz) within the deformation range from 0.01 to 500% to characterize the designed gels in terms of their resistance to applied strain through the definition of their linear viscoelastic region (LVE, i.e., the strain range is which storage modulus -G′- is constant), the linearity limit ($\gamma_L$, i.e., the limiting value of the LVE region) and the yield stress (YS, i.e., the value of shear stress at the maximum of the loss modulus -G″-). Then, frequency sweep tests were performed within the LVE region, at three different temperatures (i.e., 25, 30, and 37°C) and angular frequency ranging between 0.1 and 100 rad/s to characterize the progressive transition from the sol to the gel state. At each tested temperature, the angular frequency at G′/G″ crossover ($\omega_{G'/G''crossover}$) was determined using Matlab (MathWorks, R2016b version). Finally, the temperature-driven sol-to-gel transition was investigated through temperature ramp tests at constant frequency (0.1 Hz) and rate (2°C/min) within the temperature range from 0 to 40°C. Gelation onset temperature ($T_{onset}$) was then identified at the minimum of viscosity. All tests were performed using a stress-controlled MCR302 Anton Paar rheometer equipped with a Peltier system for temperature control and a 50 mm parallel plate geometry. Before each analysis, the sample was poured on instrument lower plate at 0°C, heated at the test temperature, left to equilibrate for 10 min and finally analyzed. In the case of temperature ramp tests, equilibration was performed at 0°C.

### Evaluation of Hydrogel pH Transfer Potential

Hydrogels based on NHP407 and SHP407 were qualitatively and quantitatively characterized in terms of their ability to transfer pH variation from the surrounding environment through their thickness. To quantitatively characterize hydrogel pH variation upon contact with environments at different pH values, samples were prepared as previously described and their initial pH was measured (Martini Instruments, Mi150, United States) in the sol state while keeping them in a water bath at 5°C. After complete gelation at 37°C (Memmert IF75, Schwabach, Germany) for 10 min, 1 ml of a buffer solution (phosphate buffered saline -PBS- pH 7.4 or acetate buffer at pH 5 (0.1 M), previously equilibrated at 37°C) was added to each sample. At predefined time intervals (15, 30, 45 min, 1 and 24 h), the residual buffer was withdrawn, the samples were incubated at 5°C to allow their sol-to-gel transition and finally hydrogel pH was measured. At each time point, hydrogel pH change was calculated according to Eq. 1.

$$Hydrogel\ pH\ change(\%) = \frac{pH_{to} - pH_{ti}}{pH_{to} - pH_{buffer}} \cdot 100 \qquad (1)$$

where $pH_{to}$ and $pH_{ti}$ are the measured pH values of hydrogels before (at $t_o$) and after incubation in the presence of a buffer for $t_i$ minutes, and $pH_{buffer}$ is the pH of the buffer (7.4 or 5) put in contact with the hydrogels.

Qualitative evaluation of the pH gradient moving through gel thickness was performed adding pH indicators to the hydrogels (phenol red, 0.1 mg/ml, for neutral/basic pH, and bromocresol purple, 0.1 mg/ml, for acid pH, Sigma Aldrich, Italy), which change their color in response to pH changes. Upon gelation at 37°C for 10 min, the prepared hydrogels containing pH indicators were incubated in the presence of acetate buffer at pH 5 or PBS according to the previously described protocol and then photographed at predefined time intervals.

### Hydrogel Swelling and Stability in Aqueous Environment

The capability of the developed hydrogels to absorb fluids from the surrounding environment and undergo swelling/erosion phenomena was evaluated according to a recently published protocol (Boffito et al., 2019b). In detail, hydrogels were prepared as previously described and weighed ($w_i$). Upon gelation at 37°C for 10 min, 1 ml of buffer (PBS or acetate buffer at pH 5, equilibrated at 37°C) was added upon each gel and samples were again incubated at 37°C to simulate physiological conditions. Complete buffer refresh was performed every other day. At predefined time points (6 h, 1, 3, 7, and 14 days), residual buffer was removed and samples were weighed in their wet and dried states upon lyophilization ($w_f$ and $w_{f\_dried}$, respectively). Control samples, i.e., samples not-subjected to swelling and stability tests, were also prepared and freeze dried to evaluate hydrogel initial dried weight ($w_{i\_dried}$). Finally, the percentage of hydrogel swelling (i.e., gel mass change in wet conditions) and dissolution/degradation (i.e., gel mass change in dry conditions) was evaluated according to equations reported by Boffito et al. (2016). In addition, at each time point swelling and dissolution/degradation data were correlated through the evaluation of the swelling ratio according to the formula reported by Park et al. (2009).

### *Ex vivo* Characterization of the Developed Hydrogels

To test injectability and gelation potential of SHP407 hydrogel within an organism, a proof of concept cadaver study was carried out. In line with the 3R principles, the mice employed in this study had to be finalized for reasons beyond the outlined experiments. No additional animals had to be sacrificed, thereby exploiting the "reduce" of the 3R principles. The study was performed in accordance with the German Animal Welfare Act and was approved by the local animal protection authorities (LaGeSo; permit number: G 0293/17). Mice ($n = 2$) were finalized in deep anesthesia achieved by intraperitoneal (i.p.) injection of medetomidine and ketamine [medetomidine 1 mg/kg BW (Cepetor®, CP-Pharma, Germany) and ketamin 75 mg/kg BW (Inresa Arzneimittel, Germany)] followed by cervical dislocation directly prior to the injection of the SHP407 hydrogel (15% w/v). The rodents' physiological body temperature was maintained by a heating plate set to 37°C and exposure to red light. The external temperature of the immediate environment of the cadaver was controlled using a thermometer. SHP407 hydrogel was stained with food coloring for better visualization, kept on ice until usage, and 200 μl were injected subcutaneously (s.c.) into the neck region using a 18G needle. 5 min post injection, the skin pocket containing the injected hydrogel was opened and gel distribution and gelation were inspected visually and haptically. Additionally, an external fixator (RISytems, Switzerland) was mounted on the right femur, and a 0.7 mm osteotomy gap was created using a giggly saw. Via the 18G needle, the blue-colored gel was applied into the fracture gap in order to test the gel distribution in a wound cavity.

## Particle Synthesis and Characterization

### Materials

The following compounds were purchased from Sigma Aldrich Inc.: Tetraethyl orthosilicate (TEOS); Ammonium nitrate; Cetyltrimethylammonium bromide (CTAB); 4-Aminobenzyl alcohol (ABA); Phenyl chloroformate; N,N-Diisopropyl-ethylamine (DIPEA); Dibutyltin dilaurate (DBTDL); *tert*-butanol (*t*BuOH); Tris(2,2′-bipyridyl)dichlororuthenium(II) hexahydrate (Ru); (3-chloropropyl)triethoxysilane; Di-*tert*-butyl dicarbonate ($BOC_2O$); Dimethyl sulfoxide (DMSO); N,N-Dimethylformamide (DMF); Tetrahydrofuran (THF); Dichloromethane (DCM). The rest of the chemicals (ethanol, heptane, etc.) were of the best quality and employed as received.

### Synthesis of Mesoporous Silica Nanoparticles

Mesoporous silica nanoparticles (MSNs) were synthesized following the Stöber method with some modifications (Baeza et al., 2014). Briefly, CTAB (1 g, 2.74 mmol), $H_2O$ (480 ml) and NaOH (3.5 ml) were added to a 1l flask. Then, the solution was heated to 80°C and TEOS (5 ml, 22.39 mmol) was added dropwise over 20 min. Once the addition was completed, the solution was heated for further 2 h at 80°C under magnetic stirring. After that, the precipitate was centrifuged and washed twice with water and once with ethanol. Afterward, the surfactant was removed to obtain empty pores. For that purpose, the particles were refluxed in 350 ml of a $NH_4NO_3$ solution (10 mg/ml) in EtOH (95%) at 75°C for 2 h and subsequently centrifuged (Sorvall LEGEND XTR Centrifuge, Thermo Scientific; 9000 rpm, 15 min, 10°C). The process was repeated two more times. Finally, the nanoparticles were centrifuged, washed twice with water and once with ethanol and stored in absolute ethanol.

### Synthesis of Self-Immolative Polymer (SIP)

(a) Phenyl(4-(hydroxymethyl)phenyl) carbamate (**1**)
Compound **1** was synthesized following a previously reported method (Gisbert-Garzarán et al., 2017). First, 4-aminobenzyl alcohol (1 g, 8.12 mmol) was dissolved in dry DMF (15 ml). Then, dry DIPEA (1.7 ml, 9.76 mmol) was added and the solution was placed in an ice bath. After that, phenyl chloroformate (1.12 ml, 8.83 mmol) was added dropwise, the ice bath was removed after 15 min and the reaction was stirred for 4 h. Afterward, the organic phase was extracted in ethyl acetate, washed with saturated ammonium chloride solution and finally dried over sodium sulfate. The solvent was partially evaporated and the resultant solution was precipitated in cold heptane and centrifuged (Sorvall LEGEND XTR Centrifuge, Thermo Scientific; 9000 rpm, 15 min, 10°C) twice in heptane.

(b) Tert-butyl(4-(hydroxymethyl)phenyl) carbamate (**2**) First, 4-aminobenzyl alcohol (1 g, 8.12 mmol) and di-*tert*-butyl dicarbonate (1.8 g, 8.12 mmol) were dissolved in dry THF (80 ml). Then, dry DIPEA (1.4 ml, 8.12 mmol) was added and the mixture was refluxed overnight. Afterward, the solvent was removed to obtain an oil that was dissolved in a small amount of ethyl acetate and precipitated in cold heptane. The solid was filtered off and dried under vacuum.

(c) Poly(phenyl(4-(hydroxymethyl)phenyl) carbamate (**3**) Compound **3** was synthesized following a modification of a previously reported method (Sagi et al., 2008). First, compound **1** (1 g, 4.12 mmol) was dissolved in dry DMSO (1.62 ml) and the solution was heated to 85°C. Then, DBTDL (5% mol) was added and the reaction was stirred for 2 h 30 min at 85°C. After that, compound **2** (223 mg, 1 mmol) in dry DMSO (0.5 ml) was injected and the solution was heated for further 2 h. Finally, the crude reaction mixture was precipitated in cold methanol, centrifuged (Sorvall LEGEND XTR Centrifuge, Thermo Scientific; 9000 rpm, 15 min, 10°C) and washed three times with methanol.

### Synthesis of SIP-Coated Mesoporous Silica Nanoparticles

#### *Mesoporous silica nanoparticles modified with (3-chloropropyl)triethoxysilane (MSN-CS)*

Vacuum-dried MSNs (175 mg) were first dispersed in dry toluene (30 ml). Then, (3-chloropropyl)triethoxysilane (100 μl, 0.04 mmol) was added and the mixture was refluxed overnight. After that, the particles were isolated by centrifugation (Sorvall LEGEND XTR Centrifuge, Thermo Scientific; 9000 rpm, 15 min, 10°C), washed with toluene and ethanol and dried under vacuum.

*SIP-coated mesoporous silica nanoparticles (MSN-CS-SIP)*

First, vacuum-dried MSN-CS (175 mg) were dispersed in dry DMSO (25 ml). Separately, compound **3** (0.33 g, 0.1 mmol) was dissolved in dry DMSO (2.5 ml). Then, dry DIPEA (25.6 μl, 0.15 mmol) was added and the solution was stirred for 2 h for alcohol activation. After that, the polymer-containing solution was added dropwise to the nanoparticle dispersion and the mixture was heated to 80°C. Afterward, a second vial containing compound **3** in dry DMSO was activated for 2 h with dry DIPEA and subsequently added to the nanoparticle solution. Finally, a third vial containing compound **3** in DMSO was activated with dry DIPEA and added to the nanoparticle solution. After that, the whole reaction mixture was stirred overnight at 80°C. Finally, SIP-coated particles (MSN-CS-SIP) were centrifuged (Sorvall LEGEND XTR Centrifuge, Thermo Scientific; 9000 rpm, 15 min, 10°C), washed with DMSO, water and ethanol and dried under vacuum. For pH-triggered release experiments, the fluorescent red dye tris(2,2′-bipyridine)dichloro ruthenium (II) (Ru) was loaded into the MSN framework before SIP grafting according to Gisbert-Garzarán et al. (2017). Briefly, MSN-CS (175 mg) were incubated in a Ru solution (10.4 mg/ml in DMSO) at room temperature and under stirring for 24 h. Then, the dispersion was heated to 80°C and subjected to the previously described protocol. Ru containing MSNs will be referred to with the acronym MSN-CS-SIP-Ru.

### Characterization of MSNs, SIP, MSN-CS, and MSN-CS-SIP

A step-by-step approach was adopted for the characterization of the synthesized mesoporous matrices and their coating, encompassing the analysis of compounds **1–3**, MSNs, MSN-CS (see **Supplementary File**) and culminating with the characterization of MSN-CS-SIP samples.

MSN-CS-SIP samples were characterized by Power X-Ray Diffraction (XRD) analyses performed using a Philips X'Pert diffractometer equipped with a Cu Kα radiation (wavelength 1.5406 Å). XRD patterns were registered within the 2θ range from 0.6° to 6°, with a step size of 0.02° and 5 s counting time/step. ATR-FTIR analyses were performed using a Nicolet Nexus instrument (Thermo Fisher Scientific) equipped with a Goldengate ATR accessory. Spectra resulted from the average of 64 scans within the spectral range 4000–400 $cm^{-1}$ at 1 $cm^{-1}$ resolution. Nitrogen adsorption and desorption isotherms were recorded on degassed samples (approximately 50 mg kept under vacuum at 40°C for 24 h) at 77 K using a Micromeritics ASAP 2020 equipment. Surface area and pore size distribution were estimated through the Brunauer-Emmett-Teller (BET) and the Barrett-Joyner-Halenda (BJH) methods, respectively. Pore volume was defined from the amount of $N_2$ adsorbed at a relative pressure of approximately 0.99. Thermogravimetric (TG) analyses were conducted using a Perkin Elmer Pyris Diamond TG/DTA instrument within the temperature range from RT to 600°C (5°C/min) to quantify the amount of organic phase present in the sample (10 mg).

## Hybrid Hydrogel Design and Characterization

### Preparation of Hybrid PEU/MSN-CS-SIP Sol-Gel Systems

Hybrid NHP407 and SHP407 hydrogels containing MSN-CS-SIP were prepared according to Boffito et al. (2019b). Briefly, PEU-based hydrogels were initially prepared according to the protocol described in section "Hydrogel preparation protocol" at higher concentration by solubilizing the polymer in the solution portion composed of physiological solution and phosphate buffer at pH 8 (0.1 M), which represents the 90% of the total aqueous solution volume required to solubilize the material at a final concentration of 15% w/v. Then, the residual 10% of aqueous solution (i.e., PBS) was used to prepare a MSN-CS-SIP-containing dispersion. In detail, MSN-CS-SIP were first dispersed at 50 mg/ml concentration in PBS through sonication (26 W, 20 kHz, Vibracell VCX130, Sonics, United States) for 3 min in a water-ice bath to avoid evaporation and then an aliquot was added to the previously solubilized PEU samples to reach final particle and polymer concentrations of 5 mg/ml and 15% w/v, respectively. Particle addition was performed with hydrogels in the sol state (at 5°C) and samples were vortexed for 30 s to homogeneously distribute the particle within the hybrid sol-gel systems.

Hereafter, MSN-CS-SIP-containing hydrogels will be referred to with the acronyms NHP407_MSN-CS-SIP and SHP407_MSN-CS-SIP.

### Rheological Characterization of Hybrid Sol-Gel Systems

In order to investigate the effects of particle addition to hydrogels on their gelation potential, rheological characterization of the developed hybrid sol-gel systems was performed according to the previously described protocol (see section "Rheological characterization").

### Payload Release Test

pH-triggered release studies were performed on hybrid hydrogels encapsulating MSN-CS-SIP particles previously loaded with the red dye Ru (MSN-CS-SIP-Ru) (hydrogel acronyms: NHP407_MSN-CS-SIP-Ru and SHP407_MSN-CS-SIP-Ru). Tests were performed according to the protocol published by Gisbert-Garzarán et al. (2017) with slight changes to adapt it to sol-gel systems. In detail, hybrid hydrogels were loaded in the sol state into 24 well cell culture inserts (transwell, Greiner, poly(ethylene terephthalate) membrane, 0.4 μm pore size) (400 μl gel/insert) and allowed to gel at 37°C for 10 min. Then, 1 ml of buffer (PBS pH 7.4 or acetate buffer at pH 5, equilibrated at 37°C) was added to each well containing an insert and release tests were conducted in physiological like conditions (i.e., in incubator at 37°C). Release medium was collected at predefined time intervals (1, 2, 4, 5, 24, 28, 72, 96, 168, and 336 h) and completely refreshed with the same volume of fresh buffer at 37°C. Collected release media were then analyzed through a plate reader (Perkin Elmer Victor X3) at a wavelength of 450 nm. For the quantification of released dye, a calibration curve was constructed starting from Ru standards prepared in PBS or

acetate buffer at pH 5 at different concentrations within the range 0–200 μg/ml.

### *Ex vivo* Characterization of Hybrid Sol-Gel Systems

The gelation and dispersion of SHP407_MSN-CS-SIP-Ru hydrogel were studied similarly to SHP407 sol-gel system as such (section "*Ex vivo* Characterization of the Developed Hydrogels"). 200 μl of composite hydrogel (SHP407_MSN-CS-SIP-Ru), SHP407 hydrogel or MSN-CS-SIP-Ru dispersion (all kept on ice until usage) were injected s.c. into the neck region of just finalized murine cadavers ($n$ = 4 mice) maintained at physiological body temperature. After 5 min, the cadavers were imaged using an *in vivo* imaging system (IVIS® Lumina, Caliper LifeSciences, MA; ex/em filter: 465 nm/Cy5.5). After imaging, the injection site was opened through a skin incision and the dispersion and appearance (i.e., sol or gel state) of the different injected materials were inspected visually and haptically.

## Statistical Analysis

Statistical analysis of the collected data was performed using GraphPad Prism 5 for Windows (GraphPad Software, Inc., Version 5.03, 2009)[1]. In detail, Two-way ANOVA analyses followed by Bofferoni's multiple comparison tests were performed on data collected from swelling, dissolution/degradation, pH variation and release tests. Statistical differences were defined according to Boffito et al. (2016). Analyses were performed in triplicate and results are reported as mean ± standard deviation.

# RESULTS

## Chemical Characterization of NHP407 and SHP407

The as-synthesized NHP407 PEU containing P407 as building block was chemically characterized by Attenuated Total Reflectance Fourier Transform Infrared (ATR-FTIR) spectroscopy and Size Exclusion Chromatography (SEC). The effects of Boc-deprotection reaction on the integrity of PEU backbone were investigated by ATR-FTIR and SEC analyses, meanwhile the effective Boc group removal was assessed by Proton Nuclear Magnetic Resonance spectroscopy. Finally, exposed -$NH_2$ groups were colorimetrically quantified according to Laurano et al. (2020).

### Characterization of NHP407 Poly(ether urethane)

Attenuated Total Reflectance Fourier Transform Infrared spectroscopic analyses were performed on both as-synthesized NHP407 and the starting P407 macrodiol for comparison (**Supplementary Figure S1**). As expected, NHP407 spectrum exhibited all the characteristic absorption bands of P407 at 2877 $cm^{-1}$ ($CH_2$ stretching vibration), 1242 $cm^{-1}$ ($CH_2$ rocking vibration) and 1099 $cm^{-1}$ (asymmetric stretching of -$CH_2$-O-$CH_2$- groups typical of PEO blocks in P407). The formation of urethane bonds in NHP407 induced the appearance in its ATR-FTIR spectrum of new absorption peaks at 3347 $cm^{-1}$ (N-H stretching vibration), 1720 and 1630 $cm^{-1}$ (stretching vibration of carbonyl groups, amide I), and 1539 $cm^{-1}$ (concurrent bending and stretching of N-H and C-N bonds, respectively). The absence of absorption peaks within 2200 and 2300 $cm^{-1}$ proved the complete conversion of isocyanate groups.

NHP407 exhibited $\overline{M}_n$ and D values of 44600 Da and 1.42, respectively, as assessed by SEC analyses.

### Characterization of SHP407 Poly(ether urethane)

With the aim to assess the integrity of PEU backbone upon treatment in $CHCl_3$/TFA mixture (90/10 v/v), ATR-FTIR, SEC and $^1$H NMR analyses were performed on SHP407 samples and NHP407 as control. ATR-FTIR spectrum of SHP407 was completely overlapped with that of native NHP407 (**Supplementary Figure S1**) and no absorption peaks ascribable to residual $CHCl_3$ or TFA (e.g., C-Cl and C-F stretching vibration at 600–800 $cm^{-1}$ and 1000–1400 $cm^{-1}$, respectively) were detected.

Estimated $\overline{M}_n$ value slightly decreased after the Boc-deprotection reaction ($\overline{M}_n$ and D of SHP407 were measured to be 40700 Da and 1.56, respectively), but this change was not significant considering the typical SEC analysis error (approximately 10%) (Trathnigg, 2000).

**Supplementary Figure S2** reports the $^1$H NMR spectra of NHP407 (control) and SHP407 samples. Magnified inserts in the spectral regions between 5.65–5.73 and 7.00–7.20 highlight the characteristic bands of urea and urethane N-H groups, respectively (Qin et al., 2019). The magnified insert of NHP407 spectrum within 1.31 and 1.41 ppm shows the co-presence of resonances typical of the methylene protons of HDI-deriving block (at 1.22 and 1.37 ppm) and the methyl protons of Boc caging groups (sharp singlet at 1.37 ppm, overlapped to HDI-derived signals) (Caddeo et al., 2019). Differently, the methylene protons adjacent to the urethane bonds appeared at 2.93 ppm. Upon treatment in acid conditions, the singlet at 1.37 due to Boc protons significantly decreased, indicating that the reaction conditions allowed an almost complete Boc removal (deprotection yield > 90%).

The number of exposed primary amines in SHP407 was colorimetrically quantified through the Orange II sodium salt assay. The effective exposure of amino groups along polymer chains was indirectly proved by the darker orange color of SHP407 solutions in $ddH_2O$ at pH 12 compared to NHP407 control samples, which exhibited a weak orange color ascribable to physical adsorbance phenomena of dye molecules to polymer chains. Assuming that orange molecules and -$NH_2$ groups electrostatically interact at a 1:1 molecular ratio and subtracting the contribution of dye adsorbance to polymer chains, the number of exposed free primary amines along SHP407 was estimated to be 3.07E18 ± 1.63E17 -$NH_2$/$g_{SHP407}$.

[1]http://www.graphpad.com

## Characterization of NHP407- and SHP407-Based Sol-Gel Systems

NHP407- and SHP407-based hydrogels (15% w/v), prepared by solubilizing the PEUs in aqueous medium (i.e., physiological solution/PBS/buffer at pH 8 at 80/10/10 v/v), were characterized in terms of their temperature-driven gelation, capability to change their pH in response to the external aqueous medium as well as swelling and stability in aqueous environments at different pH values. Finally, injectability, gelation and gel distribution upon subcutaneous injection were evaluated *ex vivo* in a rodent model.

### Thermo-Sensitive Behavior of NHP407 and SHP407 Hydrogels

The gelation potential of NHP407- and SHP407-based sol-gel systems was first qualitatively evaluated by tube inverting test. LCGT values were measured to be 26 and 28°C (error ± 0.5°C) for NHP407 and SHP407 hydrogels, respectively. Tube inverting test in isothermal conditions at 37°C, instead, allowed the estimation of hydrogel gelation time in physiological conditions, which turned out to be 4 and 5 min (error ± 30 s) for NHP407 and SHP407 sol-gel systems, respectively. To obtain further insight on the sol-to-gel transition of NHP407 and SHP407 hydrogels, a thorough rheological characterization was performed by strain sweep, frequency sweep and temperature ramp tests (**Figure 1**). **Figure 1A** reports the trends of storage and loss moduli (G′ and G″) at 37°C as a function of strain in the range 0.01–500% for NHP407 and SHP407 gels. As expected for structured materials, when the strain ($\gamma$) exceeded a critical value ($\gamma_L$, limiting strain value of the LVE), G′ started to decrease, while G″ initially increased and then decreased, representing an overshoot behavior that can be correlated to a strain hardening effect. NHP407 and SHP407 hydrogels showed a similar behavior, but the NHP407-based sol-gel system was characterized by slightly higher critical deformation ($\gamma_L$ of 18.6 and 11.6% for NHP407 and SHP407 gels, respectively) and mechanical strength (higher G′ values within the LVE) with respect to SHP407-based one (mean G′ value within LVE for NHP407 and SHP407 gels was 8880 and 6780 Pa, respectively). Gel Yield Stress (YS) was measured to be 1790 and 875 Pa for NHP407 and SHP407 formulations, respectively. Frequency sweep tests were conducted to study the progress of gel formation and development with increasing temperature (three different temperatures were tested, i.e., 25, 30, and 37°C) (**Figure 1C**). **Table 1** reports the G′/G″ crossover frequencies ($\omega_{G'/G''crossover}$) and the G′/G″ delta at 100 rad/s ($\Delta_{G'/G''\_100\ rad/s}$) for NHP407 and SHP407 gels at each tested temperature. No significant differences were observed between NHP407 and SHP407 hydrogels that were both characterized by G′ values becoming progressively constant with temperature increase, proving the progressive gel formation. At 37°C, indeed, both NHP407 and SHP407 gels turned out to be in the gel state with $\omega_{G'/G''crossover}$ lower than 0.1 rad/s. However, the kinetics of gel formation and development slightly slowed down in SHP407-based sol-gel system with respect to NHP407-based one, as shown by the slight increase in $\omega_{G'/G''crossover}$ at 25 and 30°C observed in SHP407 formulation compared to NHP407 one. The temperature-driven gelation of NHP407 and SHP407 sol-gel systems was also investigated by rheological temperature ramp tests (**Figure 1B**), which highlighted that SHP407-based formulation exhibited a similar gelation process compared to NHP407-based one. **Table 2** summarizes the characteristic parameters extracted from the measured temperature ramp curves: the gelation onset temperature ($T_{onset}$), viscosity at 0°C ($\eta_{0°C}$) and viscosity value at 25°C ($\eta_{25°C}$). As typical of solutions, viscosity initially decreased with increasing temperature until a minimum value was reached that was followed by a sharp viscosity increase. The temperature at the minimum of viscosity ($T_{onset}$) represents the onset of the gelation process, i.e., the temperature at which polymer chains started to aggregate into micelles. The formed micelles then tended to organize into a gel network as evidenced by the viscosity increase at higher temperatures. At a certain temperature of about 29–30°C, the viscosity of both the analyzed systems decreased with increasing temperature as a consequence of melt fracture phenomena due to gel mechanical failure induced by the application of a continuous strain rate (Boffito et al., 2016).

**TABLE 1** | Frequency values at G′/G″ crossover ($\omega_{G'/G''crossover}$) and G′/G″ delta at 100 rad/s ($\Delta_{G'/G''\_100\ rad/s}$) for NHP407 and SHP407 hydrogels, evaluated at 25, 30, and 37°C.

| | $\omega_{G'/G''crossover}$ (rad/s) | | $\Delta_{G'/G''\_100\ rad/s}$ (Pa) | |
|---|---|---|---|---|
| | NHP407 | SHP407 | NHP407 | SHP407 |
| 25°C | 27.46 | 32.25 | 2130 | 1410 |
| 30°C | 2.05 | 2.51 | 7670 | 5660 |
| 37°C | <0.1 | <0.1 | 9650 | 7340 |

**TABLE 2** | $T_{onset}$, $\eta_{0°C}$ and $\eta_{25°C}$ of NHP407 and SHP407 hydrogels, estimated from rheological temperature ramp tests.

| | NHP407 | SHP407 |
|---|---|---|
| $\eta_{0°C}$ (Pa · s) | 0.57 | 0.50 |
| $T_{onset}$ (°C) | 16.03 | 16.36 |
| $\eta_{25°C}$ (Pa · s) | 201.7 | 230.2 |

### Investigation of Hydrogel pH Transfer Potential

NHP407 and SHP407 gel ability to transfer pH changes through their thickness was tested in acid and neutral environments (i.e., pH 5 and 7.4). First, a quantitative evaluation was obtained through the measurement of hydrogel pH after incubation with buffers at different pHs (PBS, acetate buffer at pH 5) for predefined time intervals (0, 15, 30, 45 min, 1, 24 h) at 37°C (**Figures 2A,B**). NHP407- and SHP407-based hydrogels showed initial pH of 7.45 ± 0.10 and 7.67 ± 0.02, respectively. After 15 min contact with acetate buffer at pH 5, the pH of both hydrogels significantly decreased ($0.0001 < p < 0.001$) reaching values of 6.54 ± 0.06 and 6.50 ± 0.08 (no significant difference), respectively. However, although both the sol-gel systems reached a pH value of about 6.5, the initial pH of SHP407 hydrogels was significantly higher than that of NHP407 systems ($0.01 < p < 0.05$). Starting from 30 min incubation,

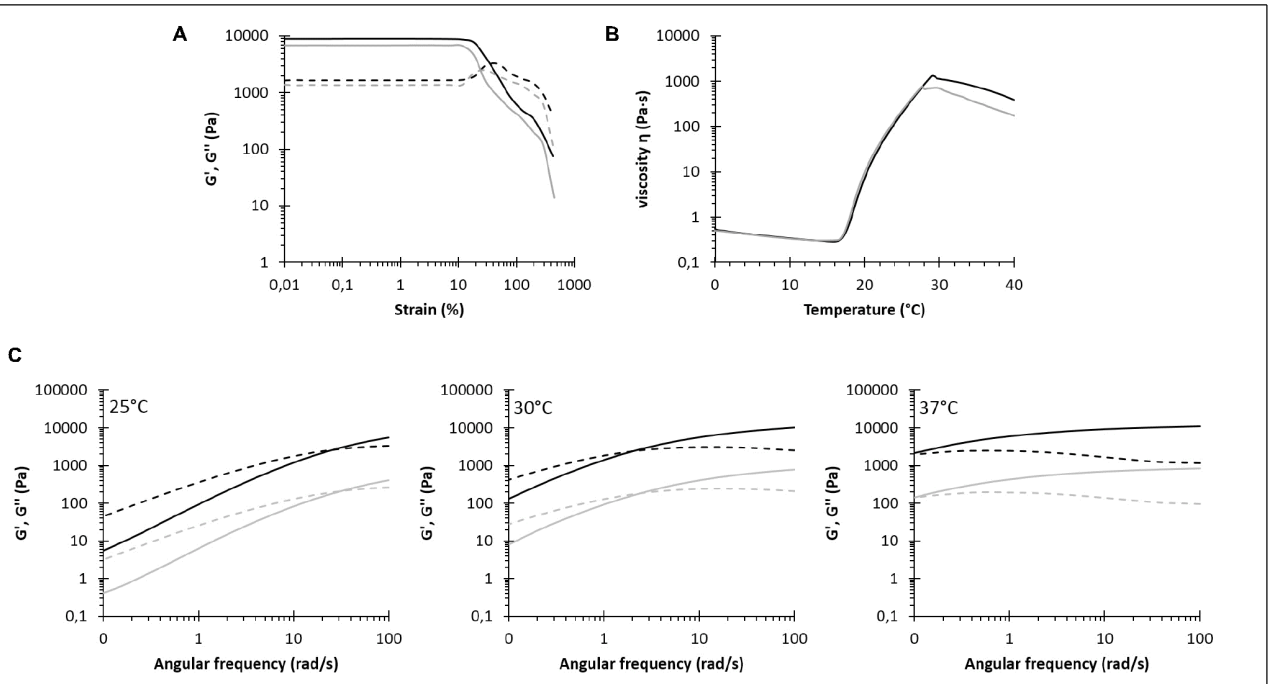


**FIGURE 1 |** Rheological characterization of NHP407 (black) and SHP407 (gray) hydrogels. **(A)** Storage (G′, continuous line) and loss (G″, dashed line) moduli trends as a function of applied strain at 37°C. **(B)** Trend of viscosity (η) as a function of temperature within 0–40°C temperature range. **(C)** G′ and G″ trends (continuous and dashed lines, respectively) as a function of angular frequency at 25, 30, and 37°C. G′ and G″ values of SHP407 hydrogels were divided by a factor of 10.

hydrogel pH progressively decreased toward the value of the surrounding aqueous medium, with no significant differences between NHP407 and SHP407 hydrogels at all investigated time points (after 24 h incubation in a buffer at pH 5, NHP407 and SHP407 gels reached a pH value of 5.32 ± 0.03 and 5.32 ± 0.00, respectively) (**Figure 2A**). The progressive change of hydrogel pH over time was then evaluated according to Eq. 1 (**Figure 2C**), highlighting that pH variations in SHP407-based hydrogels showed a faster kinetics compared to NHP407-based systems up to 45 min incubation time. For instance, NHP407 and SHP407 gels covered 42.01 ± 3.42 and 52.00 ± 0.65% ($0.01 < p < 0.05$) of the pH delta between their initial pH value and the pH of the buffer (i.e., pH 5) within the first 30 min of incubation, respectively. As control condition, pH transfer tests were also conducted by soaking the gels in neutral pH environment (i.e., PBS) (**Figure 2B**). As expected, both NHP407 and SHP407 hydrogels did not show significant pH variations at each analyzed time point, with the exception of 24 h incubation for SHP407-based formulation (from 60 min to 24 h incubation time, SHP407 hydrogel pH significantly decreased from 7.76 ± 0.01 to 7.61 ± 0.04, $0.01 < p < 0.05$). On the other hand, at each investigated time point the pH of SHP407 hydrogels was significantly higher than that of NHP407 sol-gel systems ($0.0001 < p < 0.001$), in accordance with its higher initial pH. After 24 h incubation in contact with PBS, NHP407 and SHP407 hydrogels exhibited pH values of 7.26 ± 0.02 and 7.61 ± 0.04, respectively. The progressive pH gradient moving through gel thickness was qualitatively evaluated observing the change in color of gels containing pH indicators and put in contact with acetate buffer at pH 5 or PBS (**Figure 2D**). In accordance with quantitative measurements, no changes in the color of the hydrogels were observed upon incubation in the presence of PBS, meaning that no gradient of pH change was moving through hydrogel thickness. Conversely, a progressive variation of gel color from blue to yellow was observed in gels incubated in acetate buffer at pH 5.

## Investigation of Hydrogel Swelling and Stability in Aqueous Media

The capability of NHP407- and SHP407-based gels to absorb fluids from the surrounding environment undergoing swelling/erosion phenomena was evaluated at 37°C by incubating the samples in contact with PBS or acetate buffer at pH 5. Gel swelling [gel mass change in wet state (%)] and dissolution/degradation [gel mass change in dry state (%)] over time are reported in **Figures 3A,B**, meanwhile **Figure 3C** reports swelling ratio data evaluated at each time point according to Park et al. (2009).

Irrespective of the surrounding environment pH, swelling prevailed over erosion/dissolution (**Figures 3A,B**) up to 7 days incubation for both NHP407 and SHP407 gels. However, with increasing incubation time in aqueous media, hydrogel dissolution/degradation became progressively predominant over swelling, with a consequent deswelling (i.e., a decrease in swelling percentage) which assumed negative values when erosion/dissolution completely prevailed over absorption phenomena. In the presence of a buffer at pH 5, NHP407- and SHP407-based gels showed similar swelling behavior, with

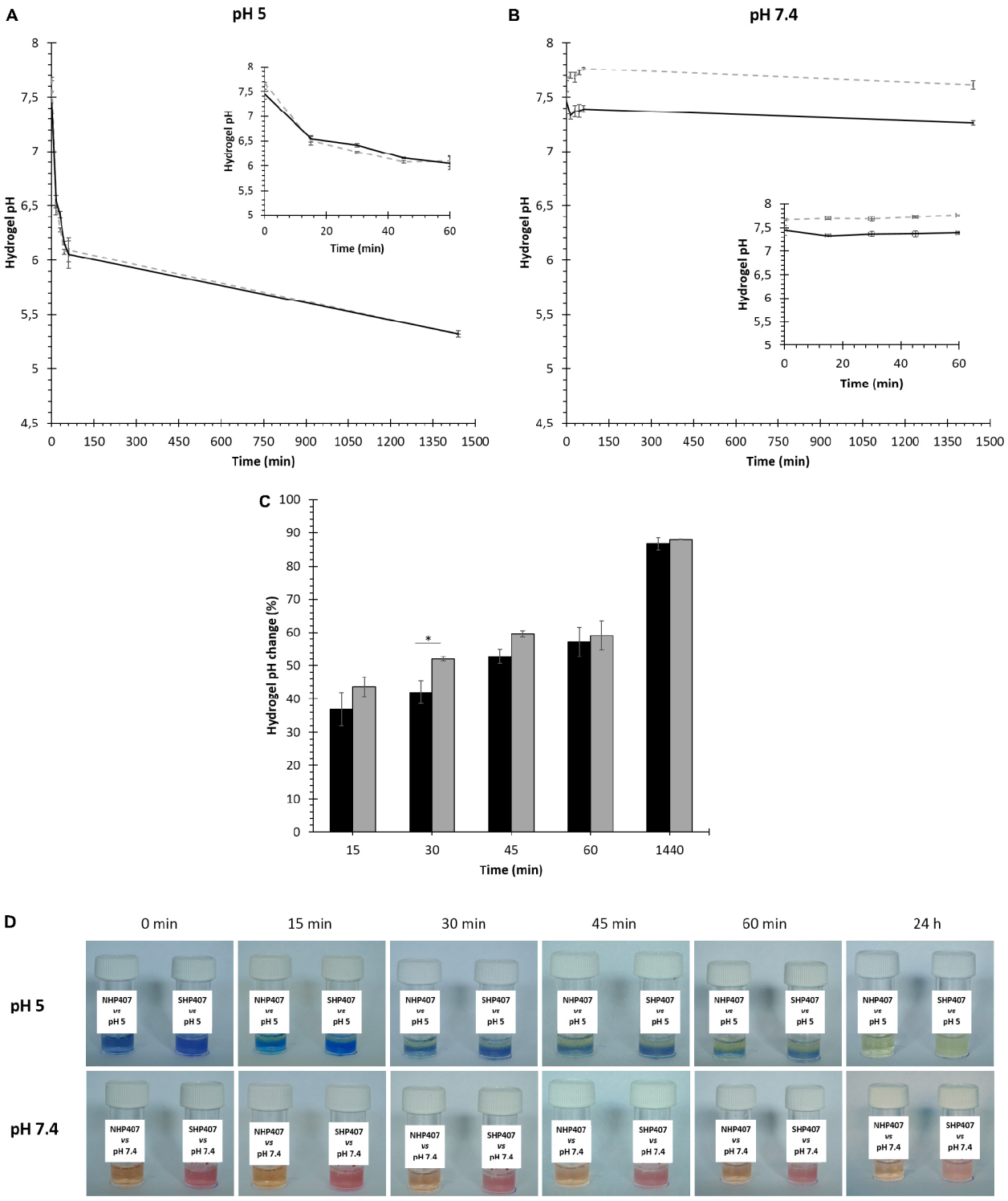


**FIGURE 2 |** Sensitivity of NHP407- and SHP407-based gels to environmental pH (pH 5 and 7.4). **(A,B)** NHP407 (black, continuous line) and SHP407 (gray, dashed line) hydrogel pH values after incubation in buffered solutions at pH 5 or 7.4 for different time intervals. Magnified inserts evidence the trend of hydrogel pH within the first 60 min incubation in aqueous medium. **(C)** Percentage of pH change (evaluated according to Eq. 1) in NHP407- (black) and SHP407- (gray) based hydrogels upon incubation in the presence of acetate buffer at pH 5 for different time intervals. **(D)** Representative images of NHP407 and SHP407 gels containing pH indicators (phenol red for neutral/basic pH and bromocresol purple for acid pH) which change their color in response to pH changes. Gels were soaked in acetate buffer solution at pH 5 or phosphate buffered solution at pH 7.4 for different time intervals.

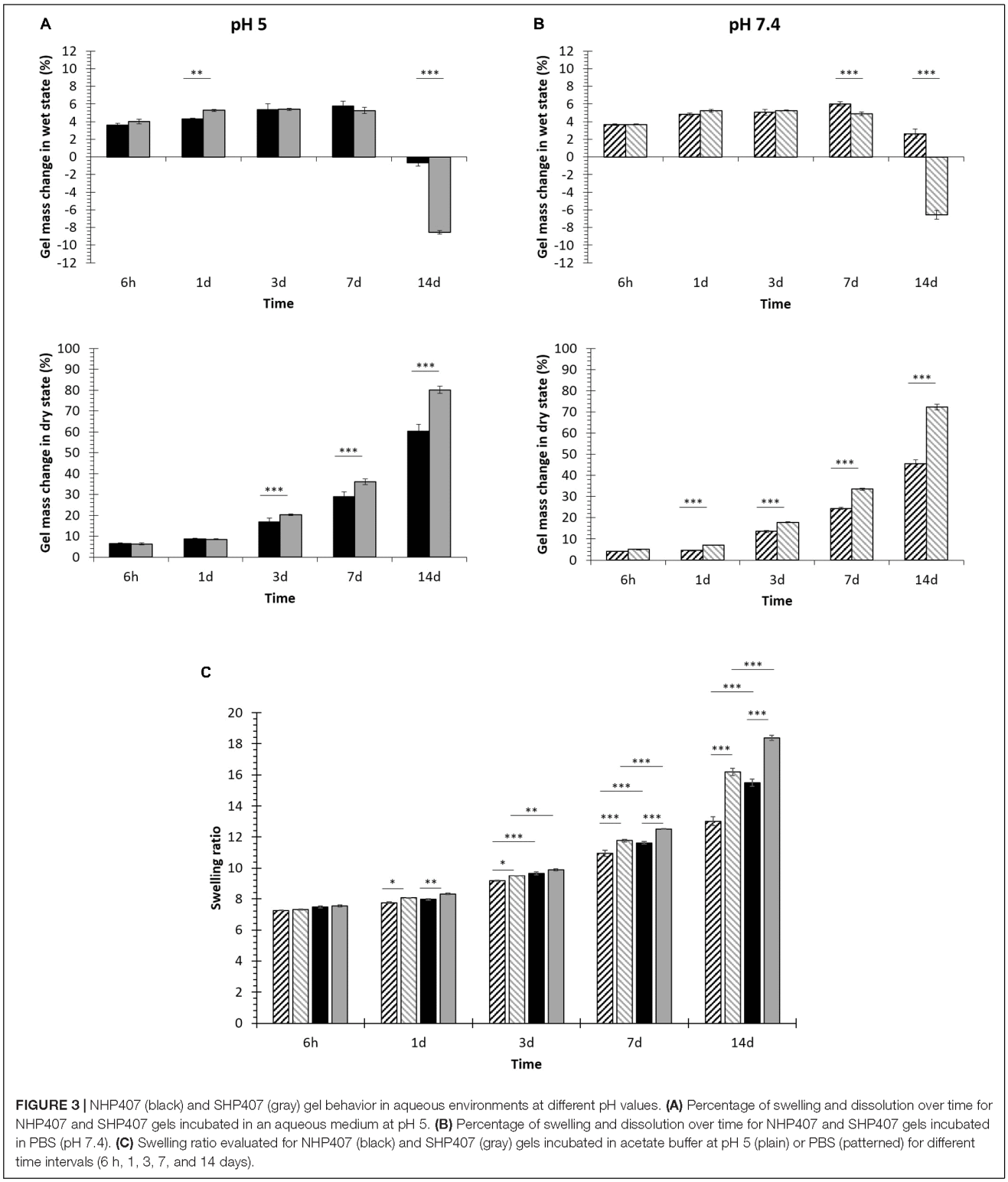


**FIGURE 3 |** NHP407 (black) and SHP407 (gray) gel behavior in aqueous environments at different pH values. **(A)** Percentage of swelling and dissolution over time for NHP407 and SHP407 gels incubated in an aqueous medium at pH 5. **(B)** Percentage of swelling and dissolution over time for NHP407 and SHP407 gels incubated in PBS (pH 7.4). **(C)** Swelling ratio evaluated for NHP407 (black) and SHP407 (gray) gels incubated in acetate buffer at pH 5 (plain) or PBS (patterned) for different time intervals (6 h, 1, 3, 7, and 14 days).

significantly different swelling percentages at 1 and 14 days incubation time. In the same environment, SHP407-based gels showed significantly higher dissolution compared to NHP407-based ones starting from 3 days incubation time ($0.0001 < p < 0.001$), reaching a dissolution of $78.98 \pm 0.15$ and $60.61 \pm 0.98$%, respectively after 14 days incubation. Gels

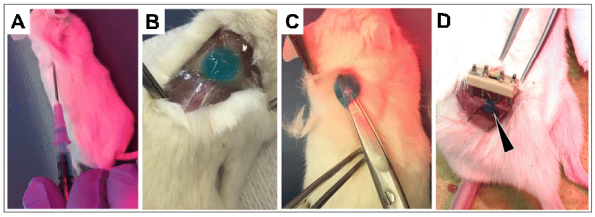


**FIGURE 4 |** Injection and gelation of SHP407 hydrogel *in situ* into murine cadavers. **(A)** Using an 18G needle, blue-colored SHP407 hydrogel was injected s.c. into the neck region. Physiological temperature of the organism was maintained using a heating pad and red light. **(B)** Solidified SHP407 gel 5 min post s.c. injection into the neck region. **(C)** Test of solidity by lifting the SHP407 gel up. **(D)** Solid SHP407 gel (black arrow) exclusively present within the osteotomy area 5 min post injection into the fracture gap.

immersed in PBS showed a similar swelling trend, with SHP407 gels undergoing significant deswelling compared to NHP407 ones. Similarly to data collected from hydrogels incubated in acid pH aqueous medium, SHP407 gels exhibited higher weight loss in the dry state compared to NHP407, with significant differences ($0.0001 < p < 0.001$) from 1 day incubation on. Hence, SHP407-based sol-gel systems showed higher destabilization compared to NHP407-based ones irrespective of the environmental pH surrounding them. This consideration was also proved by the analysis of swelling ratio data (**Figure 3C**), that evidenced a higher swelling ratio for SHP407 gels compared to NHP407 ones at each analyzed time point, at both pH 5 and pH 7.4. On the other hand, the swelling ratio for both NHP407 and SHP407 gels was higher at pH 5 compared to pH 7.4 at each time point, with significant differences on 3, 7 and 14 days incubation.

### *Ex vivo* Evaluation of Hydrogel Injectability and Gelation

In order to study hydrogel injectability, dispersion and gelation *in situ* within an organism, *ex vivo* proof of concept studies were carried out working with murine cadavers. In detail, the dispersion and gelation of SHP407 hydrogel were investigated by injecting 200 μl subcutaneously (s.c.) in the neck region (**Figure 4A**). In **Figures 4B–D**, representative images of solid SHP407 gel at 5 min post injection are depicted. The blue color derives from food coloring that was previously confirmed to not affect gelation properties (data not shown). **Figure 4B** clearly shows a minimum dispersion of SHP407 sol-gel system as it presented as a coherent and spherical gel. **Figure 4C** demonstrates the solidity of SHP407 system, which allowed lifting the hydrogel using scissors. To study the dispersion and gelation of SHP407 in a more advanced application, a 0.7 mm femoral midshaft osteotomy was created in the cadaver and the hydrogel (∼15 μl) was introduced into the osteotomy gap using a 18G needle (**Figure 4D**). The spherical shape and the finding that the SHP407 gel remained in the gap region, without dripping onto the muscle tissue below the femur, further stresses the quick gelation and minimum dispersion *in situ*.

## Particle Characterization

Mesoporous silica nanoparticles and SIP were initially synthesized and characterized separately (see **Supplementary Material**). In detail, MSNs were physico-chemically and morphologically characterized by XRD, ATR-FTIR spectroscopy, nitrogen adsorption and desorption analyses, TG analyses, DLS, SEM and TEM, meanwhile the SIP and its constituent blocks (i.e., compounds **1** and **2**) were characterized by $^{1}$H NMR spectroscopy. The functionalization of MSNs with the pH-responsive polymeric coating was accomplished following a two-step synthetic protocol: (i) MSNs functionalization with an organosilane acting as linker between the surface and the SIP (MSN-CSs) and (ii) DIPEA-mediated alcohol activation and mixing with the particles (**Scheme 2**). SIP-coated MSNs (MSN-CS-SIP) resulting from the grafting of SIP on MSN surface were then characterized as MSNs as such to assess the effect of the coating procedure on particle physico-chemical and morphological properties.

### Characterization of SIP-Coated Mesoporous Silica Nanoparticles

As observed in **Supplementary Figure S3A**, the diffraction maxima typical of mesoporous silica nanoparticles were still observable after the grafting of the SIP on top of mesoporous silica nanoparticles. The amount of organic matter incorporated was analyzed though TG analysis (**Supplementary Figure S3B**). The addition of the self-immolative coating increased the weight loss up to *ca.* 15%, compared to MSNs as such. The samples were further analyzed using ATR-FTIR spectroscopy (**Supplementary Figure S3C**), unrevealing the presence of new functional groups. For instance, vibration bands typical of the carbamate of the self-immolative polymer (C=O stretching vibration at 1630 cm$^{-1}$) were present in MSN-CS-SIP ATR-FTIR

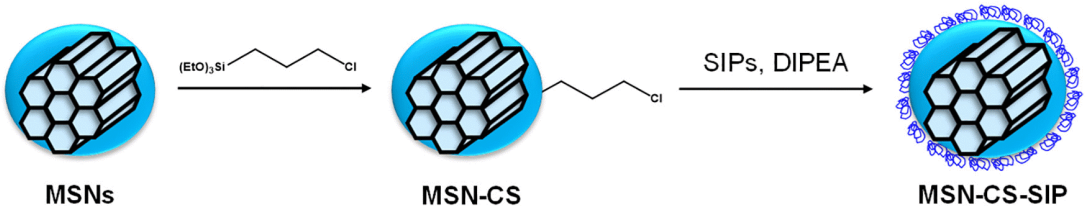


**SCHEME 2 |** Schematic representation of the coating of MSNs with the SIP. First, the nanoparticles were surface modified with a chloro alkoxysilane (MSN-CS) and then subjected to SIP grafting, leading to SIP-coated MSNs (MSN-CS-SIP).

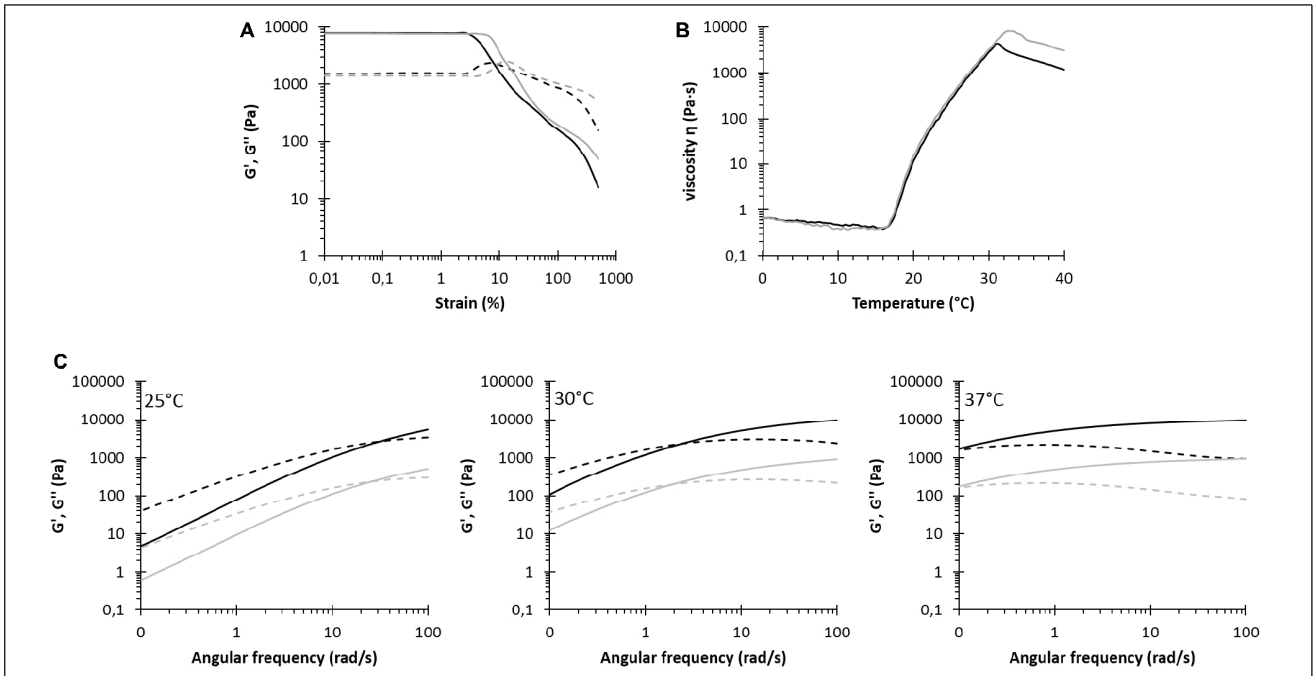


**FIGURE 5 |** Rheological characterization of NHP407_MSN-CS-SIP (black) and SHP407_MSN-CS-SIP (gray) hydrogels. **(A)** Storage (G′, continuous line) and loss (G″, dashed line) moduli trends as a function of applied strain at 37°C. **(B)** Trend of viscosity (η) as a function of temperature within 0–40°C range. **(C)** G′ and G″ trends (continuous and dashed lines, respectively) as a function of angular frequency at 25, 30, and 37°C. G′ and G″ values of SHP407_MSN-CS-SIP hydrogels were divided by a factor of 10.

spectrum. $N_2$ adsorption analysis (**Supplementary Figure S3D**) showed a reduction of the textural parameters after the SIP coating. In detail, the specific surface area decreased *ca.* 40% after SIP grafting (from *ca.* 1000 $m^2/g$ for MSNs to *ca.* 650 $m^2/g$ for MSN-CS-SIP).

## Hybrid Hydrogel Characterization

NHP407- and SHP407-based hydrogels (15% w/v) encapsulating MSN-CS-SIP (5 mg/mL) were first characterized through rheological tests. Release tests against different pHs were conducted on hydrogels encapsulating MSN-CS-SIP previously loaded with a fluorescent dye as model drug (Ru). Finally, hybrid hydrogel injectability, gelation, distribution and detectability upon subcutaneous injection were evaluated *ex vivo* in a rodent model.

### Thermo-Sensitive Behavior of NHP407 and SHP407 Hydrogels Encapsulating MSN-CS-SIP

In order to assess the effects of particle addition on hybrid hydrogel gelation, rheological characterization of NHP407_MSN-CS-SIP and SHP407_MSN-CS-SIP hydrogels was conducted by strain sweep, frequency sweep and temperature ramp tests (**Figure 5**). **Figure 5A** reports the trends of storage and loss moduli at 37°C as a function of applied strain within the range 0.01–500%. Both storage and loss moduli initially showed a constant value (within the LVE region) up to the linearity limit ($\gamma_L$) which turned out to be 2.83 and 7.25% for NHP407_MSN-CS-SIP and SHP407_MSN-CS-SIP gels, respectively. Moreover, within the linear viscoelastic region, G′ showed higher values than G″ for both NHP407_MSN-CS-SIP and SHP407_MSN-CS-SIP gels, proving that at 37°C the developed systems were in the gel state. NHP407_MSN-CS-SIP and SHP407_MSN-CS-SIP gels exhibited mean G′ values within the LVE region of 7800 and 7600 Pa, respectively, meanwhile their Yield Stress was measured to be 262 and 442 Pa. For strain value higher than $\gamma_L$, storage modulus started to decrease, while G″ increased reaching a maximum value (2350 and 2550 Pa for NHP407_MSN-CS-SIP and SHP407_MSN-CS-SIP gels, respectively), as typical for structured networks. After this maximum value was achieved, also G″ started to decrease as a consequence of macro-cracks development throughout the sample which finally led to its complete failure, with the hydrogel behaving as a sol (i.e., G″ > G′). Hydrogel progressive transition from the sol to the gel state with increasing temperature was investigated by frequency sweep tests conducted within the angular frequency range from 0 to 100 rad/s at 25, 30, and 37°C (**Figure 5C**). **Table 3** reports the frequency values at G′/G″ crossover ($\omega_{G'/G''\,crossover}$) and the G′/G″ delta at 100 rad/s ($\Delta_{G'/G''\_100\ rad/s}$) for NHP407_MSN-CS-SIP and SHP407_MSN-CS-SIP evaluated at 25, 30, and 37°C. For both NHP407_MSN-CS-SIP and SHP407_MSN-CS-SIP, $\omega_{G'/G''\,crossover}$ value decreased with increasing temperature, as a sign of hydrogel temperature-drive gelation. On the other hand, particle encapsulation within SHP407-based systems led to lower $\omega_{G'/G''\,crossover}$ values compared to SHP407 hydrogels as such (at 25°C $\omega_{G'/G''\,crossover}$ of 32.25 and 25.96 Pa for SHP407 and SHP407_MSN-CS-SIP hydrogels, respectively) (see

section "Thermo-Sensitive Behavior of NHP407 and SHP407 Hydrogels"). Conversely, MSN-CS-SIP loading within NHP407 hydrogels resulted in slightly increased $\omega_{G'/G''crossover}$ values compared to NHP407 as such (at 25°C $\omega_{G'/G''crossover}$ increased from 27.46 rad/s for NHP407 to 30.98 rad/s for NHP407_MSN-CS-SIP). Despite these differences, at 37°C both the systems appeared to be in the gel state, but complete gel development (i.e., G′ independent over frequency) was not achieved, similarly, to NHP407 and SHP407 as such.

The trend of viscosity as a function of temperature for NHP407_MSN-CS-SIP and SHP407_MSN-CS-SIP is reported in **Figure 5B**, meanwhile the characteristic parameters of temperature ramp tests are summarized in **Table 4**. Initial viscosity slightly increased in MSN-CS-SIP-containing hybrid hydrogels compared to pure NHP407 and SHP407 sol-gel systems ($\eta_{0°C}$ values for SHP407_MSN-CS-SIP and SHP407 systems were 0.66 and 0.50, respectively). Similarly, viscosity values of MSN-CS-SIP-containing hydrogels slightly increased compared to hydrogels as such at each tested temperature within the analyzed range; for instance, at 25°C NHP407_MSN-CS-SIP and virgin NHP407 exhibited a viscosity of 265.0 and 201.7 Pa · s, respectively. On the other hand, the trend of the onset temperature of gelation for SHP407-based hybrid system was opposite, with SHP407_MSN-CS-SIP hydrogel showing a slightly lower $T_{onset}$ value compared to virgin sol-gel system. No differences in $T_{onset}$ were observed between NHP407 and NHP407_MSN-CS-SIP.

## Payload Release Tests in Aqueous Environment at pH 5 or 7.4

The progressive release of the red dye tris(2,2′-bipyridine)dichloro ruthenium (II) (Ru) from SIP-coated MSNs embedded within NHP407 and SHP407 hydrogels (NHP407_MSN-CS-SIP-Ru and SHP407_MSN-CS-SIP-Ru) was investigated in aqueous environment at different pH values. **Figure 6A** reports payload release profiles over time from SHP407_MSN-CS-SIP-Ru gels incubated in pH 5 and pH 7.4 aqueous media. Similar trends were obtained also from NHP407_MSN-CS-SIP-Ru gels (data not reported). Additionally, at each analyzed time point, both NHP407_MSN-CS-SIP-Ru and SHP407_MSN-CS-SIP-Ru showed significantly higher Ru dye release in pH 5 buffer compared to PBS ($0.0001 < p < 0.001$). Furthermore, the exposure of free amines along SHP407 polymer chains induced an increased release of Ru molecules in acid pH environment from SHP407_MSN-CS-SIP-Ru compared to NHP407_MSN-CS-SIP-Ru at each analyzed time point (statistically significant differences at 72 and 96 h observation time, $0.01 < p < 0.05$) (**Figure 6B**). On the other hand, at pH 7.4, Ru release from SHP407_MSN-CS-SIP-Ru was not significantly higher (approximately 5–6%) than its release from NHP407_MSN-CS-SIP-Ru (**Figure 6C**). Conversely, in acid pH environment higher differences were detected at each investigated time interval, with released Ru amounts approximately 10% higher for SHP407_MSN-CS-SIP-Ru compared to NHP407_MSN-CS-SIP-Ru.

**TABLE 3** | Frequency values at G′/G″ crossover ($\omega_{G'/G''crossover}$) and G′/G″ delta at 100 rad/s ($\Delta_{G'/G''\_100\ rad/s}$) for NHP407_MSN-CS-SIP and SHP407_MSN-CS-SIP evaluated at 25, 30 and 37°C.

| | $\omega_{G'/G''crossover}$ (rad/s) | | $\Delta_{G'/G''\_100\ rad/s}$ (Pa) | |
|---|---|---|---|---|
| | NHP407_MSN-CS-SIP | SHP407_MSN-CS-SIP | NHP407_MSN-CS-SIP | SHP407_MSN-CS-SIP |
| 25°C | 30.98 | 25.96 | 2060 | 2160 |
| 30°C | 2.37 | 2.01 | 7220 | 6980 |
| 37°C | <0.1 | <0.1 | 8840 | 8745 |

**TABLE 4** | $T_{onset}$, $\eta_{0°C}$ and $\eta_{25°C}$ of NHP407_MSN-CS-SIP and SHP407_MSN-CS-SIP hydrogels estimated from rheological temperature ramp tests.

| | NHP407_MSN-CS-SIP | SHP407_MSN-CS-SIP |
|---|---|---|
| $\eta_{0°C}$ (Pa · s) | 0.64 | 0.66 |
| $T_{onset}$ (°C) | 16.0 | 15.7 |
| $\eta_{25°C}$ (Pa · s) | 265.0 | 321.0 |

## *Ex vivo* Evaluation of Hybrid Hydrogel Injectability and Gelation

*Ex vivo* evaluation of hybrid hydrogel injectability, gelation and distribution was conducted according to the protocol previously adopted for SHP407 hydrogel as such. In detail, hybrid SHP407 hydrogel embedding MSN-CS-SIP-Ru was compared with SHP407 hydrogels as such and MSN-CS-SIP-Ru aqueous dispersion. Moreover, the fluorescent nature of particles' cargo was utilized to study the detectability of the materials under the skin via an *in vivo* imaging system (IVIS). Prior to s.c. injection into murine cadavers, the fluorescence-based detectability of Ru-loaded MSN-CS-SIP within aqueous dispersion or upon incorporation within SHP407 hydrogel was confirmed using IVIS imaging (**Figure 7A**, ex/em filter: 465 nm/ Cy5.5). Then, the just finalized mice were injected with 200 μl of material at similar concentrations, maintained at physiological body temperature and imaged after 5 min of incubation using the IVIS. **Figure 7B** shows the fluorescence signal obtained from Ru-loaded MSNs (ex/em filter: 465 nm/ Cy5.5), which was detectable for animals 1, 3, and 4 in accordance to the nature of the injected material. In fact, animal 1 received an injection of MSN-CS-SIP-Ru dispersion, animal 2 an injection of SHP407 hydrogel as such and animals 3 and 4 were injected with the composite hydrogel SHP407_MSN-CS-SIP-Ru. By comparing animals 1 to 3 and 4, the animal that received MSN-CS-SIP-Ru suspended in physiological fluid already showed a less round shape of the fluorescence-positive injection area 5 min after injection. After the imaging, the injection site was uncovered (**Figure 7C**). The photographic pictures confirmed the previously seen low dispersion and good solidification of SHP407 hydrogel (animal 2), which was found to be similar to the distribution and gelation properties of the composite hydrogel (animals 3 and 4). On the contrary, MSN-CS-SIP-Ru injected as suspension in physiological fluid dispersed broadly as shown in the magnified image of the injection area. **Figure 7D** underlines the successful

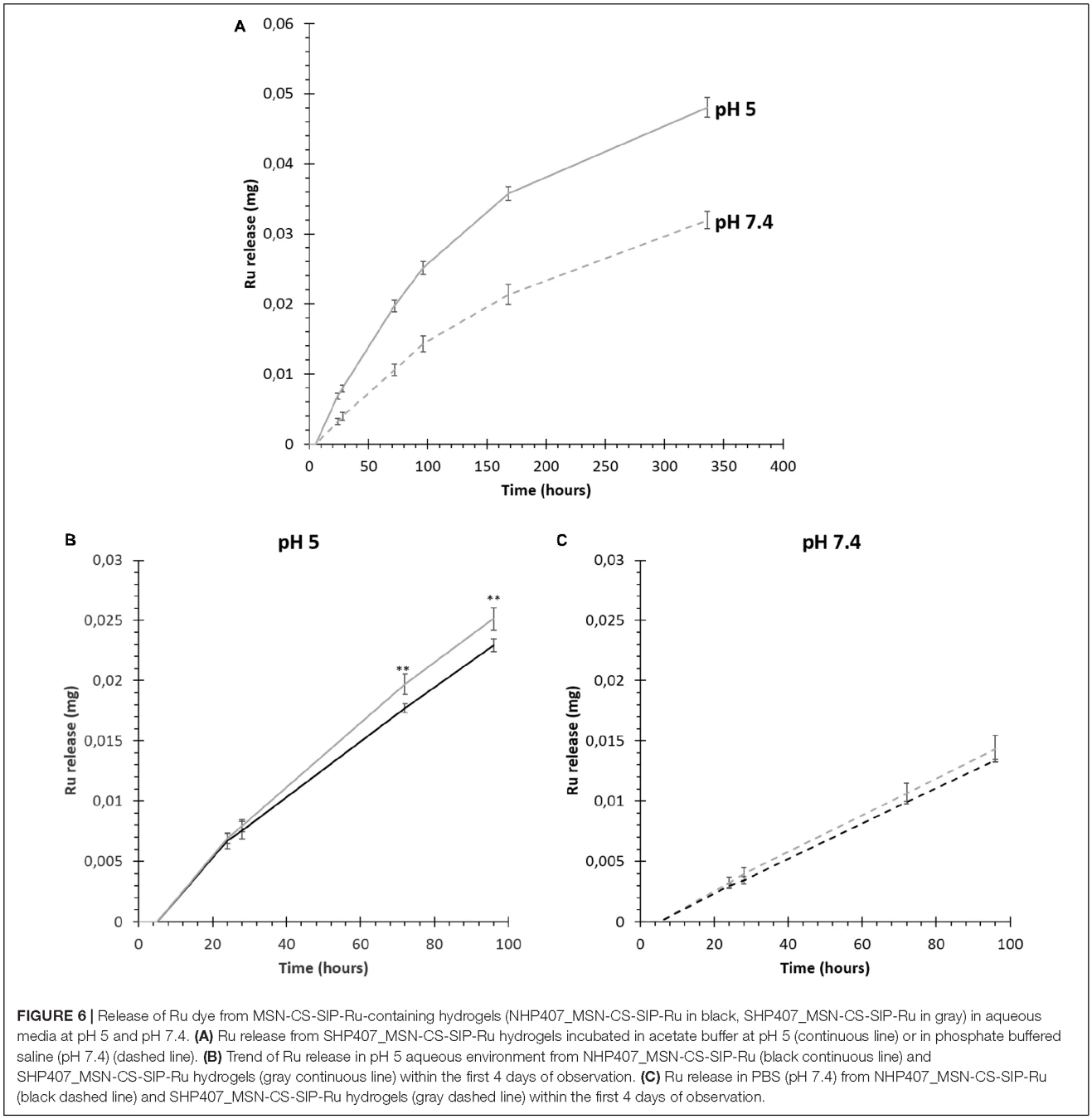


**FIGURE 6 |** Release of Ru dye from MSN-CS-SIP-Ru-containing hydrogels (NHP407_MSN-CS-SIP-Ru in black, SHP407_MSN-CS-SIP-Ru in gray) in aqueous media at pH 5 and pH 7.4. **(A)** Ru release from SHP407_MSN-CS-SIP-Ru hydrogels incubated in acetate buffer at pH 5 (continuous line) or in phosphate buffered saline (pH 7.4) (dashed line). **(B)** Trend of Ru release in pH 5 aqueous environment from NHP407_MSN-CS-SIP-Ru (black continuous line) and SHP407_MSN-CS-SIP-Ru hydrogels (gray continuous line) within the first 4 days of observation. **(C)** Ru release in PBS (pH 7.4) from NHP407_MSN-CS-SIP-Ru (black dashed line) and SHP407_MSN-CS-SIP-Ru hydrogels (gray dashed line) within the first 4 days of observation.

gelation of SHP407 as such and in composite with MSN-CS-SIP-Ru, as both could be lifted up as a whole using forceps (black arrows) and remained in their solid form after harvest from the injection site (**Figure 7D**, dashed pictures, top left).

## DISCUSSION

In a scenario characterized by the progressive development and optimization of patient-specific smart therapeutic approaches, there is an urgent need of *ad hoc* designed injectable formulations with the potential to be finely tuned according to the pathological environment. Additionally, these injectable therapeutics could be designed to exhibit sensitivity to different physico-chemical stimuli, thus making them able to properly adapt their properties in response to external environment characteristics, with a consequent capability to smartly exert their function in the target tissue/organ. Within this complex and challenging scenario, in this work we attempted to design and thoroughly characterize a new injectable formulation responding

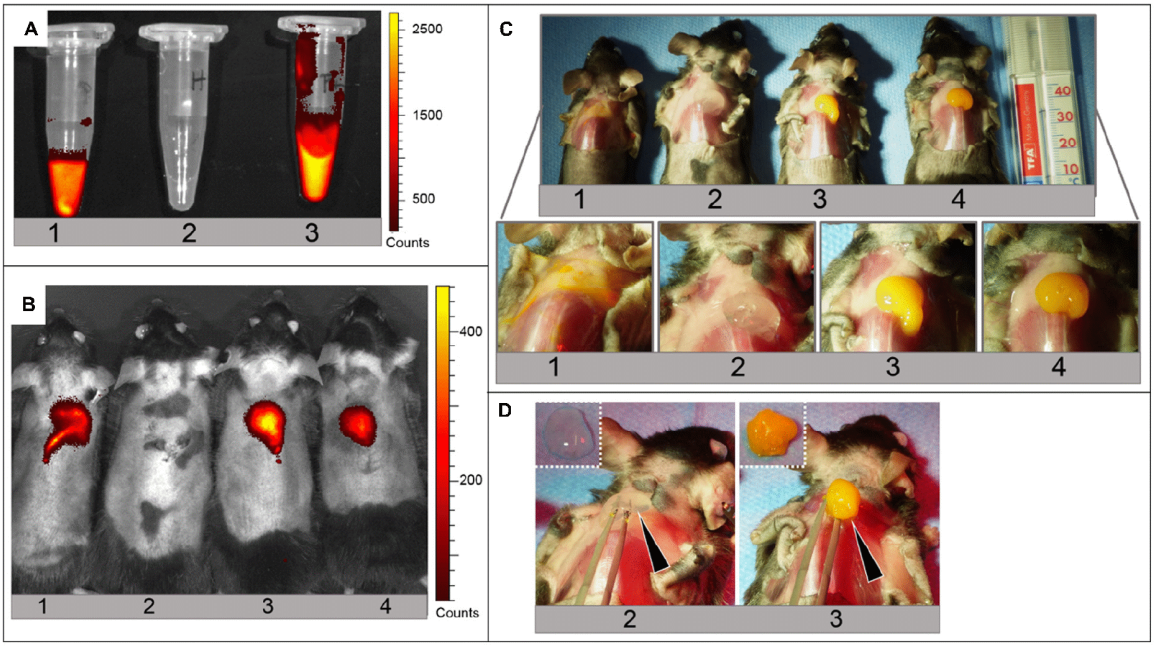


**FIGURE 7 |** Injection and gelation of MSN-CS-SIP-Ru aqueous dispersion, SHP407 hydrogel and SHP407_MSN-CS-SIP-Ru hybrid hydrogel *in situ* into murine cadavers. **(A)** IVIS read at ex/em filter: 465 nm/ Cy5.5 of MSN-CS-SIP-Ru aqueous dispersion (1), SHP407 hydrogel (2) and SHP407_MSN-CS-SIP-Ru hybrid hydrogel (3) before injection in the animal model. **(B)** IVIS read at ex/em filter: 465 nm/ Cy5.5 of murine cadavers with maintained physiological body temperature subjected to injection of MSN-CS-SIP-Ru aqueous dispersion **(1)**, SHP407 hydrogel **(2)** and SHP407_MSN-CS-SIP-Ru hybrid hydrogel **(3,4)**. Only those animals injected with samples containing Ru-loaded MSN-CS-SIP exhibited a fluorescence signal. **(C)** Photographic images of the animals previously measured in the IVIS (same numbering) including a magnification of the injection site. Solid materials can be seen in animal **(2–4)**, whereas MSN-CS-SIP-Ru were broadly dispersed in the animal injected with particle suspension (animal 1). **(D)** Test of gelation of SHP407 (animal 2) and SHP407_MSN-CS-SIP-Ru (animal 3) by lifting the material up (black arrows). The solid form was maintained after the harvest (dashed pictures, top left of each image).

to the aforementioned demands by exploiting the custom-made nature of its components. In fact, we combined amphiphilic PEU-based thermo-sensitive sol-gel systems with MSNs coated with a SIP providing them sensitivity to acid pH environments. Custom-made PEUs were used as alternative to commercially available Poloxamers® to develop thermo-sensitive hydrogels with improved gelation properties (i.e., lower critical gelation concentration, faster gelation in physiological conditions), mechanical strength and residence time in aqueous environments (Boffito et al., 2016). Additionally, PEU versatile chemistry was exploited to introduce free amines along the polymer backbone to provide the resulting material with an enhanced sensitivity to external pH environment. On the other hand, MSNs have been selected for their easy synthesis route, tunable pore morphology and dimension, suitability to surface functionalization to expose specific functional moieties and high surface area and pore volume, which are responsible for their high loading capacities of different payloads (e.g., drugs, growth factors) (Narayan et al., 2018; Zhou et al., 2018; Xu et al., 2019; Manzano and Vallet-Regí, 2020). However, mesoporous particles exhibit an open porous network that usually makes payload diffusion out from them very fast. In this regard, the introduction of gatekeepers closing the pore entrance and opening on-demand in the presence of specific conditions has been reported as a valuable strategy to control payload release (Wen et al., 2017). In this work, MSNs were surface functionalized with a self-immolative polymer caging their pore mouth and undergoing head to tail degradation in the presence of acid pH, thus inducing pore opening and acid-pH triggered cargo release, as already demonstrated by Gisbert-Garzarán et al. (2017). According to a bottom up approach, the key components of the therapeutic formulation, i.e. the hydrogel and the particles, were first designed and characterized as single entities and then they were assembled to develop hybrid sol-gel systems answering to the previously described needs.

An amphiphilic water soluble PEU with acronym NHP407 was synthesized using Poloxamer® 407, HDI and N-Boc serinol as building blocks. Successful NHP407 synthesis was proved by ATR-FTIR spectroscopy, SEC analyses and $^{1}$H NMR spectroscopy. The comparison between native P407 and NHP407 ATR-FTIR spectra proved the synthesis of a PEU containing P407 blocks. Indeed, in addition to P407 typical absorption peaks, new bands characteristic of urethane bonds appeared in NHP407 spectrum (**Supplementary Figure S1**). Additionally, complete consumption of isocyanate groups was proved by the absence of –N=C=O characteristic peak around 2200–2300 cm$^{-1}$. Similarly, $^{1}$H NMR spectrum of NHP407 (**Supplementary Figure S2**) showed the characteristic peaks of all the building blocks used for its synthesis, i.e., resonances ascribable to the PEO and PPO segments of P407 and to the methylene protons of HDI blocks and serinol moieties (Caddeo et al., 2019). In addition, methyl

protons of Boc caging groups showed their typical resonance at 1.37 ppm, in the form of a sharp singlet overlapped to HDI signals (Caddeo et al., 2019). Finally, the successful binding of NHP407 building blocks through urethane bonds was demonstrated by the signal within the spectral range between 5.65 and 5.73, which is typical of N-H groups of urethane groups (Qin et al., 2019). However, also side-reactions leading to urea bond formation occurred during NHP407 synthesis, as proved by the presence of a signal in its $^1$H NMR spectrum within the spectral region from 7.00 to 7.20 ppm (attributed to urea N-H groups) and the peak at 1630 $cm^{-1}$ in its ATR-FTIR spectrum (ascribed to urea carbonyl groups) (**Supplementary Figures S1, S2**; Laurano et al., 2020). Nevertheless, despite urea by-product formation, a high molecular weight polymer with a narrow molecular weight distribution was obtained (NHP407 $\overline{M}_n$ and D were measured to be 44600 Da and 1.42, respectively). NHP407 was designed to expose Boc-protected amines along its polymer chains, which could be made available through a deprotection reaction in acid conditions, similarly to protocols habitually adopted during peptide synthesis. In this work, the protocol for Boc caging group removal from NHP407 chains was optimized to maximize free amine exposure, while avoiding detrimental polymer degradation (see **Supplementary Material**). In the optimized conditions, NHP407 was treated in a $CHCl_3$/TFA mixture at 90/10 v/v, obtaining SHP407. ATR-FTIR spectrum of SHP407 was completely overlapped to that of native NHP407, confirming the retention of PEU chemical structure and the complete removal of both $CHCl_3$ and TFA (**Supplementary Figure S1**). Similarly, also $^1$H NMR spectrum of SHP407 sample was completely overlapped to that of native NHP407, with the exception of the peak attributed to the methyl protons of Boc caging groups at 1.37 ppm (**Supplementary Figure S2**). This peak, indeed, significantly decreased its intensity in SHP407 compared to NHP407, thus proving an almost complete removal of the Boc groups (deprotection yield > 90%). SEC analyses evidenced a slight decrease in number average molecular weight upon the deprotection reaction, which, however, fell within the typical SEC analysis error (approximately 10%) (Trathnigg, 2000). The number of exposed free amines along SHP407 chains turned out to be 3.07E18 ± 1.63E17 -$NH_2$/$g_{SHP407}$ corresponding to the 93–94% of the total theoretical number of amines present along PEU chains (i.e., approximately 2–3 primary amines exposed per each SHP407 chain), in agreement with $^1$H NMR analyses. SHP407 and NHP407 were then used to prepare thermo-sensitive sol-gel systems at 15% w/v polymer concentration in a physiological solution/PBS/buffer at pH 8 mixture at 80/10/10 volume ratio. This polymer concentration was selected based on the previous characterization performed on NHP407-based hydrogels by Boffito et al. (2016), which evidenced the high potential of this formulation as injectable fast-gelling hydrogel. On the other hand, the composition of the aqueous medium used to solubilize the polymers was optimized to force hydrogel initial pH toward a neutral value (thus protecting the SIP from degradation), while maximizing the possibility to change its pH in response to environmental pH value being a not-buffered solution. Qualitative characterization through tube inverting test highlighted that SHP407-based formulation showed a slightly increased Lower Critical Gelation Temperature and gelation time at 37°C compared to NHP407-based system. These results were further confirmed by frequency sweep tests conducted at 25, 30, and 37°C (**Figure 1C** and **Table 1**) which evidenced a slightly slowed down kinetics of SHP407-based gel formation compared to NHP407-based one (e.g., at 25°C $\omega_{G'/G''crossover}$ of SHP407 and NHP407 sol-gel systems was measured to be 32.25 and 27.46, respectively). Furthermore, also the temperature of gelation onset ($T_{onset}$) was slightly higher in SHP407 sol-gel system compared to NHP407 one ($T_{onset}$ of 16.03 and 16.36), respectively (**Figure 1B** and **Table 2**). This different behavior can be probably correlated to the different hydrophobicity of NHP407 and SHP407: being NHP407 more hydrophobic than SHP407 due to the presence of Boc caging groups, the conditions required to induce polymer chains rearrangement into micelles were more easily reached in NHP407 aqueous solution compared to SHP407 one. Conversely, SHP407-based micelles required slightly more time and higher temperature to form, but then they turned out to be able to easily and quickly arrange into a gel network similarly to NHP407 micelles. In fact, at 37°C both NHP407 and SHP407 systems exhibited $\omega_{G'/G''crossover}$ values lower than 0.1 rad/s and turned out to be in the gel state, although a not complete gel development was achieved. This result can be correlated to the presence in SHP407-based system of a higher number of hydrogen bonds due to the exposure of free -$NH_2$ groups, which contribute together with hydrophobic interactions to the progressive chain arrangement into micelles and their consequent aggregation to finally form a gel (Aoki et al., 1994; Laurano et al., 2019). This high degree of physical crosslinking within SHP407 gel was probably also responsible for its lower resistance to applied deformation ($\gamma_L$ of 18.6 and 11.6% for NHP407 and SHP407 gels, respectively) and Yield Stress (YS of 1790 and 875 Pa for NHP407 and SHP407 gels, respectively) compared to NHP407-based one (**Figure 1A**). Despite these slight differences, the G′, G″ and viscosity trends reported in **Figure 1** and the data summarized in **Tables 1**, **2** clearly evidenced that the exposure of free amines along PEU chains did not detrimentally affect the thermo-responsiveness of SHP407 hydrogel that retained the capability to quickly undergo gelation in physiological conditions. As the final hybrid formulation has been designed to release the payload encapsulated into MSNs in response to a pH trigger, the capability of both NHP407 and SHP407 gels to transfer pH changes from the surrounding aqueous environment toward their core was quantitatively evaluated through hydrogel pH measurements upon incubation with buffered solutions at pH 5 or 7.4 for predefined time intervals (**Figures 2A–C**). The progressive pH gradient through gel thickness was also visually analyzed using pH indicators (**Figure 2D**). The exposure of free amino groups along SHP407 chains effectively accelerated the transfer of acid pH through gel thickness compared to NHP407-based system. Indeed, faster pH variation kinetics (hydrogel pH change defined according to Eq. 1 within the first 30 min incubation in pH 5 environment was measured to be 42 and 52% for NHP407 and SHP407 gels, respectively) and gradient movement toward the gel core were observed in SHP407-based hydrogel compared to NHP407-based one,

probably as a consequence of the progressive protonation of exposed -$NH_2$ along SHP407 chains in acid environment. However, after this initial accelerated pH change in SHP407-based gel up to approximately 45 min incubation, the trend of pH of both kinds of gels became almost the same, with the pH value progressively tending to 5. On the other hand, Boc-deprotection did not affect the behavior of the gels in contact with a neutral pH environment, with no statistically significant differences. Gel swelling and stability in aqueous media were evaluated in the same conditions used to evaluate pH transfer potential. Due to the physical interactions responsible for micelle packing and gel network formation, two distinct and concurrent phenomena can be distinguished upon gel incubation in an aqueous environment, i.e., swelling and erosion/dissolution. In fact, in a watery environment, the gel network tends to absorb fluids from the surrounding environment, undergoing swelling. However, absorbed water molecules also induce a progressive dissolution of the polymer chains, which constitute the micelles, resulting in erosion/dissolution of the gels and therefore a decrease in hydrogel dry weight. The trends of swelling and dissolution/degradation (**Figures 3A,B**) of NHP407 and SHP407 gels were similar with dissolution/erosion phenomena becoming predominant over swelling with increasing incubation time. No clear dependence of gel swelling/stability over the pH of the surrounding aqueous medium was observed. Indeed, irrespective of the pH of the surrounding aqueous medium, SHP407-based gels exhibited an increased destabilization compared to NHP407-based ones. This different behavior can be associated to SHP407 increased hydrophilicity and water-solubility, resulting from the removal of Boc caging groups rather than to a clear pH-responsiveness induced by the exposure of amino groups along polymer backbone. Hence, although the exposed primary amines along SHP407 chains made pH transfer through gel thickness faster, they did not provide the resulting gels with a marked pH-sensitivity, which would have conferred higher swelling to SHP407 gels compared to NHP407 systems in acid environment, as a consequence of the electrostatic repulsion forces arising among micelles upon amine protonation in acid media. Increasing the number of exposed functionalities along polymer chains would lead to the design of hydrogels with further accelerated pH change capability in acid media and significantly increased swelling potential in low pH environment. To achieve this goal different approaches could be adopted. For instance, the protocol for polymer synthesis could be optimized to introduce a higher number of amine-containing building blocks in each polymer chain. In this regard, Laurano et al. have recently reported a modified synthesis protocol resulting in the introduction along the backbone of a P407-based PEU of approximately 10E20 secondary amino groups/$g_{PEU}$ (Laurano et al., 2020). Another possible route to be investigated consists in adapting the plasma treatment protocol developed by Laurano et al. (2019) to expose primary amines along polymer backbone using allylamine as monomer (Jeong et al., 2019) or ammonia gas (Mahmoudifard et al., 2017). In view of the final application of the developed formulation, SHP407 hydrogel injectability, dispersion and gelation *in situ* within an organism were demonstrated *ex vivo* using murine cadavers (**Figure 4**). Results of *ex vivo* studies concerning dispersion and gelation of SHP407 sol-gel systems were in line with *in vitro* studies, since proper solidification after 5 min of incubation in a 37°C environment was observed. The dispersion of SHP407 gel was quite low, as demonstrated by the spherical shape of the material upon visual inspection (**Figure 4B**). For future usage of the SHP407 as a place-keeper of e.g., pharmacologically active carrier-drug systems, the restricted dispersion is of outmost importance, since the location of the intervention would need to be precise and controllable. Moreover, penetration of deeper underlying tissues would not be favorable. Creating a femoral osteotomy and applying the SHP407 hydrogel into the fracture gap allowed for a more advanced application and confirmed the beneficial gelation and dispersion properties, as the hydrogel remained in the gap area and did not penetrate the tissues underneath the femur (**Figure 4D**).

As second component of the final hybrid formulation, pH-responsive nanoparticles were prepared as potential drug delivery systems by grafting a self-immolative polymer on the surface of mesoporous silica nanoparticles. The production of MSN-CS-SIP was carried out by first synthesizing and characterizing its building blocks, i.e., MSNs and SIP (see **Supplementary Material**). MSNs were then surface functionalized with the SIP in a two-step procedure according to **Scheme 2**. XRD patterns highlighted that the typical hexagonally ordered mesostructure of the particles was unaffected by the coating procedure (**Supplementary Figure S3A**). ATR-FTIR spectrum of MSN-CS-SIP sample exhibited the characteristic absorption bands of the SIP (i.e., CH and C=O stretching vibrations at approximately 3050 and 1630 $cm^{-1}$, respectively), thus proving the successful grafting of the SIP on MSN surface (**Supplementary Figure S3C**). Further confirmation of the presence of the polymeric coating covering the surface of the nanoparticles was provided by $N_2$ adsorption analysis (**Supplementary Figure S3A**) that evidenced a reduction of the characteristic textural parameters after the SIP coating (specific surface area of MSNs and MSN-CS-SIP were measured to be *ca.* 1000 vs. *ca.* 650 $m^2/g$, respectively), and TG analyses which showed the presence of a higher amount of organic material (corresponding to an increased weight loss within the 100–600°C temperature range) in MSN-CS-SIP compared to MSNs (**Supplementary Figure S3B**).

NHP407- and SHP407-based hydrogels encapsulating MSN-CS-SIP were finally prepared at 15% w/v and 5 mg/ml polymer and particle concentration, respectively. First, both NHP407_MSN-CS-SIP and SHP407_MSN-CS-SIP hydrogels were rheologically characterized to evaluate the effect of particle addition on the gelation potential and kinetics of the hybrid formulations (**Figure 5**). Particle embedding within PEU sol-gel systems turned out to affect both resistance to applied deformation and gelation kinetics of the resulting formulations. However, no detrimental effects hindering the transition from the sol to the gel state were observed. In fact, similarly to NHP407 and SHP407 hydrogels as such, both NHP407_MSN-CS-SIP and SHP407_MSN-CS-SIP systems appeared to be in the gel state at 37°C ($\omega_{G'/G''\,crossover}$ lower than 0.1 rad/s). Additionally, both the formulations did not exhibit a G′ trend independent over frequency, proving that the gel network

was not completely developed at physiological temperature (**Figure 5C** and **Table 3**). However, in terms of gelation kinetics, MSN-CS-SIP loading within the hydrogels turned out to have different effects on SHP407 and NHP407 sol-gel systems. SHP407 hybrid formulation showed a faster sol-to-gel transition compared to virgin SHP407 hydrogel, as suggested by the lower $\omega_{G'/G''crossover}$ values it exhibited at both 25 and 30°C (**Figure 5C** and **Table 3**). This behavior could be probably correlated to the presence of the polymeric coating covering the particles, which made them able to take part to the gelation process, acting as additional crosslinking points within the gel network thanks to the hydrogen bonds arising between them and SHP407 micelles. This hypothesis was further supported by the observed decrease in $T_{onset}$ (from 16.36 to 15.7°C upon particle encapsulation) (**Figure 5B** and **Table 4**). Differently, particle embedding within NHP407-based sol-gel system had an opposite effect, as demonstrated by the slightly higher $\omega_{G'/G''crossover}$ values of NHP407_MSN-CS-SIP system with respect to NHP407 control hydrogel at both 25 and 30°C. The different behavior of NHP407-based hybrid hydrogel could be ascribed to the presence of Boc groups that acted as obstacles to H-bond formation due to steric hindrance and their caging activity of amino groups that, conversely, in SHP407 were available for hydrogen bonding. Irrespective of the nature of the constituent polymer, at 37°C the particles acted as defects within the gel network, lowering its resistance to applied deformation and Yield Stress (**Figure 5A**). These results further corroborated the previous hypothesis on the formation of hydrogen bonds between the SIP and SHP407 chains. In fact, a lower decrease of both $\gamma_L$ and YS was observed for SHP407-based system compared to NHP407-based one (i.e., upon particle addition, $\gamma_L$ decreased of 84.8 and 37.5% in NHP407- and SHP407-based systems, respectively. Decrease in YS was 85.4 and 49.5% in NHP407- and SHP407-based systems, respectively). Finally, the capability of hybrid formulations to release the payload previously encapsulated in MSN-CS-SIP was characterized in pH 5 and pH 7.4 aqueous media (**Figure 6**). Despite encapsulation within the gel phase, SIP-coated MSNs retained the capability to release their cargo. In fact, at both pH 5 and pH 7.4 environments, the Ru dye was progressively released from the hybrid hydrogels with no burst release. In accordance with the pH-responsiveness of the SIP, triggered Ru dye release in acid environment was successfully achieved from both NHP407_MSN-CS-SIP-Ru and SHP407_ MSN-CS-SIP-Ru (**Figure 6A**), thus proving that the progressive SIP degradation at acid pH and the opening of the pore entrances were not hindered by the embedding of the particles within a hydrogel phase. Furthermore, the exposure of free amino groups along SHP407 polymer chains turned out to effectively enhance Ru release from SHP407_MSN-CS-SIP-Ru compared to NHP407_MSN-CS-SIP-Ru (**Figure 6B**). This result is in agreement with the accelerated decrease in pH observed in SHP407 sol-gel systems compared to NHP407 ones, during incubation in acid pH environment (**Figure 2A**). On the other hand, no significant differences in Ru release were observed in neutral pH medium, in accordance with the similar pH trend SHP407 and NHP407 hydrogels exhibited upon incubation in this environment (**Figure 2B**). *Ex vivo* injectability and gelation were then assessed also for SHP407_MSN-CS-SIP-Ru hybrid formulation (**Figures 7C,D**). The capability of the hydrogel vehicle phase to localize the therapeutic formulation in the target area was demonstrated by s.c. injecting the hybrid formulation and comparing this to a MSN-CS-SIP-Ru aqueous dispersion that, in fact, tended to broadly disperse immediately upon application (**Figure 7C**). Additionally, the loading of the fluorescent cargo Ru into the MSNs allowed for a fluorescence-based detection of the particle dispersion as such, but also upon loading into the hydrogel, both *in vitro* (**Figure 7A**) as well as *in vivo* (**Figure 7B**). Hence, SHP407 gel showed ability to transmit fluorescent signals, which can be a crucial feature for potential proof-of-concept *in vivo* payload release studies.

## CONCLUSION

The optimal therapeutic drug-release formulation should recapitulate in a sole device several features and fulfill a specific plethora of strict requirements. First, it must be easy to handle, injectable and able to completely fill body cavities or defects. Second, the capability to change its state and adapt itself to different scenarios is mandatory to allow injection, good distribution in the target tissue/organ and adequate residence time to properly exert its function. Third, it must progressively release its payload in a controlled way, avoiding undesired burst release and ensuring the delivery of active therapeutic agents within the target tissue/organ at a suitable concentration within the therapeutic window for the proper time frame. Last, it should possess high versatility allowing a wide possibility of tuning its composition. As an additional feature, smartness could make therapeutic formulations able to actively respond to external stimuli, such as physical and biochemical cues, thus allowing them to change their properties, with the consequent possibility to trigger and modulate cargo release. Within this challenging and highly demanding scenario, in this work we succeeded in developing formulations meeting the aforementioned demands and showing concurrent sensitivity to temperature and environmental pH. Thermo-responsiveness was successfully provided through the use of an amphiphilic polymer as hydrogel forming material to make the resulting formulations able to quickly gel in physiological conditions. On the other hand, mesoporous silica particles coated with a properly designed self-immolative polymer provided the resulting formulation with responsiveness to acid pH environment, resulting in accelerated delivery of their payload in specific conditions. *Ex vivo* demonstrated injectability, gelation and confined distribution of the newly designed formulations represent additional key features for their application in the biomedical field. Moreover, in view of a potential *in vivo* application, the here-developed formulations and their degradation products can be hypothesized to be suitable for complete excretion from the body. Indeed, mesoporous silica nanoparticles have been demonstrated in literature to undergo degradation/dissolution in simulated biological media, with a progressive increase in pore size and decrease in both porosity and surface area

(Cauda et al., 2010; Chen et al., 2015). On the other hand, the poly(ether urethane)s used as hydrogel-forming materials are susceptible to progressive hydrolytic or oxidative degradation, which could be also triggered by local environment properties [e.g., local pH (Mesa et al., 2005; Yang et al., 2006) and presence of specific ionic species (Boffito et al., 2019b)]. On the other hand, being dissolution the main phenomenon responsible for physical hydrogel disassembling in aqueous media in the short-term, also full-length polymer chain will probably circulate in the body and expected to be excreted via renal clearance [albumin -66 kDa- is usually referred to as a good estimate for glomerular molecular weight cut-off (Lin, 2009)].

The high potential of the here-proposed approach lies in its many compositional degrees-of-freedom and the custom-made nature of its constituents. The high versatility of poly(urethane) chemistry opens the way to the possibility to further increase the sensitivity of the gel phase to the surrounding environment through a proper selection of the building blocks or additional functionalization procedures. For instance, enzyme-sensitive blocks [e.g., matrix metalloproteinase-sensitive peptide sequences (Lutolf et al., 2003)] could be introduced into the polymer backbone allowing a further control over the stability of the system upon *in vivo* injection. On the other hand, according to recently reported data by some authors of the present work (Pontremoli et al., 2018; Boffito et al., 2019b), thermo-sensitive hydrogels based on custom-made poly(ether urethane)s have been demonstrated to allow mesoporous particle encapsulation at high concentration, thus making it possible to modulate cargo loading within a wide concentration range. In addition, the mesoporous nature of embedded particles allows the encapsulation of huge amounts of payload, thus further increasing the potential of the here-developed injectable formulations. Finally, also the custom-made nature of the self-immolative polymers opens the way to a further tuning of payload release profile. The multi-component nature of these hybrid hydrogels and the custom-made nature of its constituents will thus allow in the future to assemble *ad hoc* formulated therapeutics answering to the specific needs of each patient.

## DATA AVAILABILITY STATEMENT

The raw data supporting the conclusions of this article will be made available by the authors, without undue reservation, to any qualified researcher.

## ETHICS STATEMENT

The animal study was approved by the local animal protection authorities (Landesamt für Gesundheit und Soziales (LaGeSo); permit number: G 0293/17) and was performed in accordance with the German Animal Welfare Act.

## AUTHOR CONTRIBUTIONS

This is a multi-disciplinary work that has been conducted by three main institutions (Politecnico di Torino, POLITO, Universidad Complutence de Madrid, UCM, and Charité - Universitätsmedizin Berlin, CHARITÉ). GC was responsible for POLITO's unit and coordinated the research activities, MB, AT, CT-T, and RL designed the thermo-sensitive hydrogels and executed all the experimental activities related to hydrogel fabrication and characterization. They were also responsible for the design and characterization of hybrid sol-gel systems. CC performed and interpreted $^{1}$H NMR analyses. MV-R and MM were responsible for UCM's activities. MG-G synthesized and characterized pH-sensitive mesoporous silica nanoparticles and loaded them with the fluorescent cargo. GD, KS-B, and JB were responsible for the research activities carried out by CHARITÉ units. JB and KS-B planned and executed *ex vivo* injectability and gelation tests in rodents. Data interpretation responsibility was collectively shared by all the authors. MB wrote the whole manuscript with contribution on particle synthesis and characterization and *ex vivo* tests from MG-G and JB, respectively. All authors provided critical feedback and helped shape the research, analysis and manuscript.

## FUNDING

This project has received funding from the European Union's Horizon 2020 Research and Innovation Programme under grant agreement no. 685872-MOZART (www.mozart project.eu). MV-R acknowledged the financial support from European Research Council through ERC-2015-AdG-694160 (VERDI) project.

## ACKNOWLEDGMENTS

The authors would like to express their gratitude to Dr. Carsten Grötzinger, Charité - Universitätsmedizin Berlin, Germany, for his instrumental support by enabling the usage of the *in vivo* imaging system (IVIS).

## SUPPLEMENTARY MATERIAL

The Supplementary Material for this article can be found online at: https://www.frontiersin.org/articles/10.3389/fbioe.2020.00384/full#supplementary-material

## REFERENCES

Ahmed, E. M. (2015). Hydrogel: preparation, characterization, and applications: a review. *J. Adv. Res.* 6, 105–121. doi: 10.1016/j.jare.2013.07.006

Anggelia, M. R., Cheng, H. Y., Wen, C. J., Wang, A. Y. L., and Lin, C. H. (2019). A mixed thermosensitive hydrogel system for sustained delivery of Tacrolimus for immunosuppressive therapy. *Pharmaceutics* 11, 413. doi: 10.3390/pharmaceutics11080413

Aoki, T., Kawashima, M., Katono, H., Sanui, K., Ogata, N., Okano, T., et al. (1994). Temperature-responsive interpenetrating polymer networks constructed with poly(acrylic acid) and poly(N,N-dimethylacrylamide). *Macromolecules* 27, 947–952. doi: 10.1021/ma00082a010

Baeza, A., Guisasola, E., Torres-Pardo, A., González-Calbet, J. M., Melen, G. J., Ramirez, M., et al. (2014). Hybrid enzyme-polymeric capsules/mesoporous silica nanodevice for in situ cytotoxic agent generation. *Adv. Funct. Mater.* 24, 4625–4633. doi: 10.1002/adfm.201400729

Blondelle, S. E., and Houghten, R. A. (1993). Comparison of 55% TFA/CH2Cl2 and 100% TFA for Boc group removal during solid–phase peptide synthesis. *Int. J. Pept. Protein Res.* 41, 522–527. doi: 10.1111/j.1399-3011.1993.tb00473.x

Boffito, M., Gioffredi, E., Chiono, V., Calzone, S., Ranzato, E., Martinotti, S., et al. (2016). Novel polyurethane-based thermosensitive hydrogels as drug release and tissue engineering platforms: design and in vitro characterization. *Polym. Int.* 65, 756–769. doi: 10.1002/pi.5080

Boffito, M., Grivet Brancot, A., Lima, O., Bronco, S., Sartori, S., and Ciardelli, G. (2019a). Injectable thermosensitive gels for the localized and controlled delivery of biomolecules in tissue engineering/regenerative medicine. *Biomed. Sci. Eng.* 3:67. doi: 10.4081/bse.2019.67

Boffito, M., Pontremoli, C., Fiorilli, S., Laurano, R., Ciardelli, G., and Vitale-Brovarone, C. (2019b). Injectable thermosensitive formulation based on polyurethane hydrogel/mesoporous glasses for sustained co-delivery of functional ions and drugs. *Pharmaceutics* 11:501. doi: 10.3390/pharmaceutics11100501

Boffito, M., Sirianni, P., Di Rienzo, A. M., and Chiono, V. (2014). Thermosensitive block copolymer hydrogels based on poly(ε-caprolactone) and polyethylene glycol for biomedical applications: state of the art and future perspectives. *J. Biomed. Mater. Res. A* 103, 1276–1290. doi: 10.1002/jbm.a.35253

Bullock, A. J., Garcia, M., Shepherd, J., Rehman, I., and Sheila, M. (2019). Bacteria induced pH changes in tissue-engineered human skin detected non-invasively using Raman confocal spectroscopy. *Appl. Spectrosc. Rev.* 55, 158–171. doi: 10.1080/05704928.2018.1558232

Caddeo, S., Mattioli-Belmonte, M., Cassino, C., Barbani, N., Dicarlo, M., Gentile, P., et al. (2019). Newly-designed collagen/polyurethane bioartificial blend as coating on bioactive glass-ceramics for bone tissue engineering applications. *Mater. Sci. Eng. C* 96, 218–233. doi: 10.1016/j.msec.2018.11.012

Cauda, V., Schlossbauer, A., and Bein, T. (2010). Bio-degradation study of colloidal mesoporous silica nanoparticles: effect of surface functionalization with organo-silanes and poly(ethylene glycol). *Micropor. Mesopor. Mater.* 132, 60–71. doi: 10.1016/j.micromeso.2009.11.015

Chang, C. H., Lin, Y. H., Yeh, C. L., Chen, Y. C., Chiou, S. F., Hsu, Y. M., et al. (2010). Nanoparticles incorporated in pH-sensitive hydrogels as amoxicillin delivery for eradication of *Helicobacter pylori*. *Biomacromolecules* 11, 133–142. doi: 10.1021/bm900985h

Chatterjee, S., Hui, P. C.-L., Kan, C.-W., and Wang, W. (2019). Dual-responsive (pH/temperature) Pluronic F-127 hydrogel drug delivery system for textile-based transdermal therapy. *Sci. Rep.* 9:11658. doi: 10.1038/s41598-019-48254-6

Chen, D., Zhang, C., Huo, H., Ji, C., Sun, M., and Nie, L. (2018). Injectable temperature-sensitive hydrogel with VEGF loaded microspheres for vascularization and bone regeneration of femoral head necrosis. *Mater. Lett.* 229, 138–141. doi: 10.1016/j.matlet.2018.06.123

Chen, G., Teng, Z., Su, X., Liu, Y., and Lu, G. (2015). Unique biological degradation behavior of stöber mesoporous silica nanoparticles from their interiors to their exteriors. *J. Biomed. Nanotechnol.* 11, 722–729. doi: 10.1166/jbn.2015.2072

Dong, X., Wei, C., Liang, J., Liu, T., Kong, D., and Lv, F. (2017). Thermosensitive hydrogel loaded with chitosan-carbon nanotubes for near infrared light triggered drug delivery. *Colloids Surf. B Biointerfaces* 154, 253–262. doi: 10.1016/j.colsurfb.2017.03.036

Geng, H., Song, H., Qi, J., and Cui, D. (2011). Sustained release of VEGF from PLGA-nanoparticles mbedded thermo-sensitive hydrogel in full-thickness porcine bladder acellular matrix. *Nanoscale Res. Lett.* 6:312. doi: 10.1186/1556-276X-6-312

Gisbert-Garzarán, M., Lozano, D., Vallet-Regí, M., and Manzano, M. (2017). Self-immolative polymers as novel pH-responsive gate keepers for drug delivery. *RSC Adv.* 7, 132–136. doi: 10.1039/C6RA26771H

Gupta, M. K., Martin, J. R., Werfel, T. A., Shen, T., Page, J. M., and Duvall, C. L. (2014). Cell protective, ABC triblock polymer-based thermoresponsive hydrogels with ROS-triggered degradation and drug release. *J. Am. Chem. Soc.* 136, 14896–14902. doi: 10.1021/ja507626y

Huang, H., Qi, X., Chen, Y., and Wu, Z. (2019). Thermo-sensitive hydrogels for delivering biotherapeutic molecules: a review. *Saudi Pharm. J.* 27, 990–999. doi: 10.1016/j.jsps.2019.08.001

Jeong, Y. W., Jung, S., Han, J. J., Park, H. J., Kim, R. Y., Kim, B. H., et al. (2019). Effectiveness of surface treatment with amine plasma for improving the biocompatibility of maxillofacial plates. *Materials (Basel)* 12:2581. doi: 10.3390/ma12162581

Jiang, S., Wang, K., Dai, Y., Zhang, X., and Xia, F. (2019). Near-infrared light-triggered dual drug release using gold nanorod-embedded thermosensitive nanogel-crosslinked hydrogels. *Macromol. Mater. Eng.* 304:1900087. doi: 10.1002/mame.201900087

Kanamala, M., Wilson, W. R., Yang, M., Palmer, B. D., and Wu, Z. (2016). Mechanisms and biomaterials in pH-responsive tumour targeted drug delivery: a review. *Biomaterials* 85, 152–167. doi: 10.1016/j.biomaterials.2016.01.061

Lang, Y. Y., Li, S. M., Pan, W. S., and Zheng, L. Y. (2006). Thermo- and pH-sensitive drug delivery from hydrogels constructed using block copolymers of poly(N-isopropylacrylamide) and Guar gum. *J. Drug Deliv. Sci. Technol.* 16, 65–69. doi: 10.1016/s1773-2247(06)50010-3

Laurano, R., Boffito, M., Torchio, A., Cassino, C., Chiono, V., and Ciardelli, G. (2019). Plasma treatment of polymer powder as an effective tool to functionalize polymers: case study application on an amphiphilic polyurethane. *Polymers (Basel)* 11:E2109. doi: 10.3390/polym11122109

Laurano, R., Cassino, C., Ciardelli, G., Chiono, V., and Boffito, M. (2020). Polyurethane-based thiomers: a new multifunctional copolymer platform for biomedical applications. *React. Funct. Polym.* 146:104413. doi: 10.1016/j.reactfunctpolym.2019.104413

Liang, Y., Zhao, X., Ma, P. X., Guo, B., Du, Y., and Han, X. (2019). pH-responsive injectable hydrogels with mucosal adhesiveness based on chitosan-grafted-dihydrocaffeic acid and oxidized pullulan for localized drug delivery. *J. Colloid Interface Sci.* 536, 224–234. doi: 10.1016/j.jcis.2018.10.056

Lin, J. H. (2009). Pharmacokinetics of biotech drugs: peptides, proteins and monoclonal antibodies. *Curr. Drug Metab.* 10, 661–691. doi: 10.2174/138920009789895499

Lutolf, M. P., Lauer-Fields, J. L., Schmoekel, H. G., Metters, A. T., Weber, F. E., Fields, G. B., et al. (2003). Synthetic matrix metalloproteinase-sensitive hydrogels for the conduction of tissue regeneration: engineering cell-invasion characteristics. *Proc. Natl. Acad. Sci. U.S.A.* 100, 5413–5418. doi: 10.1073/pnas.0737381100

Mahmoudifard, M., Soleimani, M., and Vossoughi, M. (2017). Ammonia plasma-treated electrospun polyacrylonitryle nanofibrous membrane: the robust substrate for protein immobilization through glutaraldhyde coupling chemistry for biosensor application. *Sci. Rep.* 7:9441. doi: 10.1038/s41598-017-10040-7

Manzano, M., and Vallet-Regí, M. (2020). Mesoporous silica nanoparticles for drug delivery. *Adv. Funct. Mater.* 30, 3–5. doi: 10.1002/adfm.201902634

Mesa, M., Sierra, L., Patarin, J., and Guth, J. L. (2005). Morphology and porosity characteristics control of SBA-16 mesoporous silica. Effect of the triblock surfactant Pluronic F127 degradation during the synthesis. *Solid State Sci.* 7, 990–997. doi: 10.1016/j.solidstatesciences.2005.04.006

Narayan, R., Nayak, U. Y., Raichur, A. M., and Garg, S. (2018). Mesoporous silica nanoparticles: a comprehensive review on synthesis and recent advances. *Pharmaceutics* 10:E118. doi: 10.3390/pharmaceutics10030118

Noel, S., Liberelle, B., Robitaille, L., and De Crescenzo, G. (2011). Quantification of primary amine groups available for subsequent biofunctionalization of polymer surfaces. *Bioconjug. Chem.* 22, 1690–1699. doi: 10.1021/bc200259c

Ozcelik, B. (2016). "Degradable hydrogel systems for biomedical applications," in *Biosynthetic Polymers for Medical Applications,* Chapter 7, eds L. Poole-Warren, P. Martens, and R. Green (Amsterdam: Elsevier), 173–188. doi: 10.1016/B978-1-78242-105-4.00007-9

Park, H., Guo, X., Temenoff, J. S., Tabata, Y., Caplan, A. I., Kasper, F. K., et al. (2009). Effect of swelling ratio of injectable hydrogel composites on chondrogenic differentiation of encapsulated rabbit marrow mesenchymal stem cells in vitro. *Biomacromolecules* 10, 541–546. doi: 10.1021/bm801197m

Pontremoli, C., Boffito, M., Fiorilli, S., Laurano, R., Torchio, A., Bari, A., et al. (2018). Hybrid injectable platforms for the in situ delivery of therapeutic ions from mesoporous glasses. *Chem. Eng. J.* 340, 103–113. doi: 10.1016/j.cej.2018.01.073

Qin, J., Jiang, J., Ye, S., Wang, S., Xiao, M., Tao, Y., et al. (2019). High performance poly(urethane-: co-amide) from $CO_2$-based dicarbamate: an alternative to long chain polyamide. *RSC Adv.* 9, 26080–26090. doi: 10.1039/c9ra04646a

Qindeel, M., Ahmed, N., Sabir, F., Khan, S., and Ur-Rehman, A. (2019). Development of novel pH-sensitive nanoparticles loaded hydrogel for transdermal drug delivery. *Drug Dev. Ind. Pharm.* 45, 629–641. doi: 10.1080/03639045.2019.1569031

Roy, A., Maity, P. P., Bose, A., Dhara, S., and Pal, S. (2019). β-Cyclodextrin based pH and thermo-responsive biopolymeric hydrogel as a dual drug carrier. *Mater. Chem. Front.* 3, 385–393. doi: 10.1039/c8qm00452h

Rwei, S. P., Anh, T. H. N., Chiang, W. Y., Way, T. F., and Hsu, Y. J. (2016). Synthesis and drug delivery application of thermo- and pH-sensitive hydrogels: poly(β-CD-co-N-isopropylacrylamide-co-IAM). *Materials (Basel)* 9:E1003. doi: 10.3390/ma9121003

Sagi, A., Weinstain, R., Karton, N., and Shabat, D. (2008). Self-immolative polymers. *J. Am. Chem. Soc.* 8, 5434–5435. doi: 10.1021/ja801065d

Trathnigg, B. (2000). "Size-exclusion chromatography of polymers," in *Encyclopedia of Analytical Chemistry*, ed. R. A. Meyers (Chichester: Jonh Wiley & Sons Ltd), 8008–8034.

Wang, C., Javadi, A., Ghaffari, M., and Gong, S. (2010). A pH-sensitive molecularly imprinted nanospheres/hydrogel composite as a coating for implantable biosensors. *Biomaterials* 31, 4944–4951. doi: 10.1016/j.biomaterials.2010.02.073

Wen, J., Yang, K., Liu, F., Li, H., Xu, Y., and Sun, S. (2017). Diverse gatekeepers for mesoporous silica nanoparticle based drug delivery systems. *Chem. Soc. Rev.* 46, 6024–6045. doi: 10.1039/c7cs00219j

Xi, L., Wang, T., Zhao, F., Zheng, Q., Li, X., Luo, J., et al. (2014). Evaluation of an injectable thermosensitive hydrogel as drug delivery implant for ocular glaucoma surgery. *PLoS One* 9:e100632. doi: 10.1371/journal.pone.0100632

Xu, C., Lei, C., and Yu, C. (2019). Mesoporous silica nanoparticles for protein protection and delivery. *Front. Chem.* 7:290. doi: 10.3389/fchem.2019.00290

Yang, B., Guo, C., Chen, S., Junhe, M., Wang, J., Liang, X., et al. (2006). Effect of acid on the aggregation of poly(ethylene oxide)-poly(propylene oxide)-poly(ethylene oxide) block copolymers. *J. Phys. Chem. B* 110, 23068–23074. doi: 10.1021/jp0634149

Ye, Y., and Hu, X. (2016). A pH-sensitive injectable nanoparticle composite hydrogel for anticancer drug delivery. *J. Nanomater.* 2016:9816461. doi: 10.1155/2016/9816461

Zhang, W., Jin, X., Li, H., Zhang, R. R., and Wu, C. W. (2018). Injectable and body temperature sensitive hydrogels based on chitosan and hyaluronic acid for pH sensitive drug release. *Carbohydr. Polym.* 186, 82–90. doi: 10.1016/j.carbpol.2018.01.008

Zhou, Y., Quan, G., Wu, Q., Zhang, X., Niu, B., Wu, B., et al. (2018). Mesoporous silica nanoparticles for drug and gene delivery. *Acta Pharm. Sin. B* 8, 165–177. doi: 10.1016/j.apsb.2018.01.007

**Conflict of Interest:** The authors declare that the research was conducted in the absence of any commercial or financial relationships that could be construed as a potential conflict of interest.

# 8. Curriculum vitae

Mein Lebenslauf wird aus datenschutzrechtlichen Gründen in der elektronischen Version meiner Arbeit nicht veröffentlicht.

# 9. Publication list

1. Diederichs S, Bartsch L*, **Berkmann JC***, Fröse K*, Heitmann J*, Hoppe C*, Iggena D*, Jazmati D*, Karschnia P*, Linsenmeier M*, Maulhardt T*, Möhrmann L*, Morstein J*, Paffenholz SV*, Röpenack P*, Rückert T*, Sandig L*, Schell M*, Steinmann A*, Voss G*, Wasmuth J*, Weinberger ME*, Wullenkord R*.
   The dark matter of the cancer genome: aberrations in regulatory elements, untranslated regions, splice sites, non-coding RNA and synonymous mutations.
   *EMBO Mol Med*. 2016;8(5):442-457. doi: 10.15252/emmm.201506055
   * Co-authors contributed equally
2. Müller A*, **Berkmann JC***, Scheerer P, Biebermann H, Kleinau G.
   Insights into Basal Signaling Regulation, Oligomerization, and Structural Organization of the Human G-Protein Coupled Receptor 83.
   *PLoS One*. 2016;11(12):e0168260. doi:10.1371/journal.pone.0168260
   * Co-first authors
3. Bhinder G, Allaire JM, Garcia C, Lau JT, Chan JM, Ryz NR, Bosman ES, Graef FA, Crowley SM, Celiberto LS, **Berkmann JC**, Dyer RA, Jacobson K, Surette MG, Innis SM, Vallance BA.
   Milk Fat Globule Membrane Supplementation in Formula Modulates the Neonatal Gut Microbiome and Normalizes Intestinal Development.
   *Sci Rep*. 2017;7:45274. doi:10.1038/srep45274
4. Qazi TH, Berkmann JC, Schoon J, Geißler S, Duda GN, Boccaccini AR, Lippens E.
   Dosage and composition of bioactive glasses differentially regulate angiogenic and osteogenic response of human MSCs.
   *J Biomed Mater Res A*. 2018;106(11):2827-2837. doi:10.1002/jbm.a.36470
5. Gisbert-Garzarán M*, **Berkmann JC***, Giasafaki D, Lozano D, Spyrou K, Manzano M, Steriotis T, Duda GN, Schmidt-Bleek K, Charalambopoulou G, Vallet-Regí M.
   Engineered pH-Responsive Mesoporous Carbon Nanoparticles for Drug Delivery.
   *ACS Appl Mater Interfaces*. 2020;12(13):14946-14957. doi:10.1021/acsami.0c01786
   * Co-first authors
6. **Berkmann JC**, Herrera Martin AX, Ellinghaus A, Schlundt C, Schell H, Lippens E, Duda GN, Tsitsilonis S, Schmidt-Bleek K.
   Early pH Changes in Musculoskeletal Tissues upon Injury-Aerobic Catabolic Pathway Activity Linked to Inter-Individual Differences in Local pH.
   *Int J Mol Sci*. 2020;21(7):2513. doi:10.3390/ijms21072513
7. Boffito M, Torchio A, Tonda-Turo C, Laurano R, Gisbert-Garzarán M, **Berkmann JC**, Cassino C, Manzano M, Duda GN, Vallet-Regí M, Schmidt-Bleek K, Ciardelli G.
   Hybrid Injectable Sol-Gel Systems Based on Thermo-Sensitive Polyurethane Hydrogels Carrying pH-Sensitive Mesoporous Silica Nanoparticles for the Controlled and Triggered Release of Therapeutic Agents.
   *Front Bioeng Biotechnol*. 2020;8:384. doi:10.3389/fbioe.2020.00384

# Acknowledgement

Ein herzlicher Dank geht an Herrn Prof. Dr. Georg N. Duda, der es mir als Direktor des Julius Wolff Instituts und als mein Erstbetreuer ermöglichte, meine Doktorarbeit am JWI anzufertigen. Ebenso möchte ich Herrn Prof. Dr. Roland Lauster von der Technischen Universität Berlin für die Übernahme der Funktion als Zweitbetreuer meines Promotionsvorhabens danken. Ich erinnere mich gern an die konstruktiven Mentoring Meetings mit beiden Betreuern und meiner Mentorin Frau PD Dr. Katharina Schmidt-Bleek zurück. Kate, dir gilt ein besonders großer Dank dafür, dass du mich in deiner Arbeitsgruppe willkommen geheißen hast, für stets bestärkende Gespräche, für deine kreativen Ideen und dein Vertrauen in mich. Du hast mich gefördert und mir viele Entwicklungsmöglichkeiten eröffnet, die ich gern ergriffen habe.

Der gesamten AG Schmidt-Bleek möchte ich für die Zusammenarbeit und die tollen freundschaftlichen Beziehungen, die sich entwickelt haben, danken. Christian, dir danke ich besonders für unseren steten wissenschaftlichen Diskurs und dafür, dass du deinen theoretischen und methodischen Wissensschatz gern mit mir geteilt hast. Vielen Dank für die tollen Gespräche innerhalb und außerhalb des OPs und deine Unterstützung, Agnes! Aaron, danke für deine Hilfe, für gute wissenschaftliche und private Diskussionen und deine positive Einstellung. Die gemeinsamen MOZART-Reisen bleiben unvergessen. Sabine, du hast mich am längsten auf diesem Weg begleitet, ich schätze deine ruhige, aufbauende und verständnisvolle Art mindestens ebenso wie deine hervorragende Arbeit. Lisa, Gabi, Claudia, Norma, Oskar, Radost, Raphael: danke für die gute Atmosphäre in der Arbeitsgruppe!

Auch über die AG Schmidt-Bleek hinaus möchte ich mich bei einigen Kollegen besonders bedanken. Dazu gehören Taimoor, Dorit, Sven, Janosch und Julia aus der AG Geißler sowie Gabriela, von denen ich einige Methoden erlernen durfte und die mit Rat und Tat an meiner Seite standen. Ein weiteres Dankeschön geht an Evi und Hanna, mit denen ich zu Beginn dieses Promotionsvorhabens zusammengearbeitet habe. Tobias und Tazio, besten Dank für die Möglichkeit, diese Arbeit durch Proben und Perspektiven aus der Klinik zu erweitern. Insgesamt möchte ich mich bei dem gesamten JWI für ein wirklich angenehmes Arbeitsklima bedanken. Der BSRT danke ich für die zahlreichen Kurse, die ich im Rahmen der Graduiertenschule besuchen durfte, und für die sozialen Aktivitäten, die einen Austausch mit anderen Doktoranden ermöglichten.

Durch das MOZART-Konsortium konnte ich meinen wissenschaftlichen Horizont in Richtung Biomaterialforschung erweitern und habe tolle und inspirierende Menschen kennenlernen dürfen, mit denen Kooperationen und persönliche Beziehungen über diese Arbeit hinaus gehen. Besonderer Dank gilt hier UCM, Demokritos, FAU, POLITO und USFD.

Ich bin aus ganzen Herzen dankbar für den Rückhalt in meiner Familie, für euren Glauben in meine Fähigkeiten und eure stete Unterstützung! Ein herzliches Dankeschön geht auch an Familie Kallenberg – es ist immer schön mit euch. Ebenfalls danken möchte ich meinen Freunden, die mir die Freizeit in den letzten Jahren mit gemeinsamen Erlebnissen versüßt haben.

Mein tiefster Dank gilt Felix, meinem Verlobten, Wegbegleiter, Zuhörer, Motivator und Sparringspartner. Mit dir an meiner Seite konnte ich diesen Weg gehen und ich bin gespannt auf all die anderen Ziele, die wir gemeinsam erreichen werden.